Eur. Phys. J. E (2021) 44:136
https://doi.org/10.1140/epje/s10189-021-00136-4

THE EUROPEAN PHYSICAL JOURNAL E

Topical Review – Flowing Matter

Structure and dynamics of nanoconfined water and aqueous solutions

Horacio R. Corti[1,a], Gustavo A. Appignanesi[2,b], Marcia C. Barbosa[3], J. Rafael Bordin[4,c], Carles Calero[5], Gaia Camisasca[6], M. Dolores Elola[1], Giancarlo Franzese[5], Paola Gallo[6], Ali Hassanali[7], Kai Huang[8], Daniel Laria[1,9], Cintia A. Menéndez[2], Joan M. Montes de Oca[2], M. Paula Longinotti[9], Javier Rodriguez[1,10], Mauro Rovere[6], Damián Scherlis[9], and Igal Szleifer[11]

[1] Departmento de Física de la Materia Condensada & Instituto de Nanociencia y Nanotecnología (CNEA-CONICET), Comisión Nacional de Energía Atómica, B1650LWP Buenos Aires, Argentina
[2] INQUISUR, Departamento de Química, Universidad Nacional del Sur (UNS)-CONICET, 8000 Bahía Blanca, Argentina
[3] Institute of Physics, Federal University of Rio Grande do Sul, 91501-970 Porto Alegre, Brazil
[4] Department of Physics, Institute of Physics and Mathematics, 96050-500 Pelotas, RS, Brazil
[5] Secció de Física Estadística i Interdisciplinària – Departament de Física de la Matèria Condensada, Universitat de Barcelona & Institut de Nanociència i Nanotecnologia (IN2UB), Universitat de Barcelona, 08028 Barcelona, Spain
[6] Dipartimento di Matematica e Fisica, Università degli Studi Roma Tre, 00146 Roma, Italy
[7] Condensed Matter and Statistical Physics Section (CMSP), The International Center for Theoretical Physics (ICTP), Trieste, Italy
[8] Institute of Systems and Physical Biology, Shenzhen Bay Laboratory, Shenzhen, Guangdong, China
[9] Instituto de Química Física de los Materiales, Medio Ambiente y Energía (INQUIMAE-CONICET), Universidad de Buenos Aires, Buenos Aires, Argentina
[10] Escuela de Ciencia y Tecnología, Universidad Nacional de General San Martín, San Martín, Buenos Aires, Argentina
[11] Biomedical Engineering Department, Northwestern University, Evanston, USA

Received 27 August 2021 / Accepted 6 October 2021 / Published online 15 November 2021

Abstract This review is devoted to discussing recent progress on the structure, thermodynamic, reactivity, and dynamics of water and aqueous systems confined within different types of nanopores, synthetic and biological. Currently, this is a branch of water science that has attracted enormous attention of researchers from different fields interested to extend the understanding of the anomalous properties of bulk water to the nanoscopic domain. From a fundamental perspective, the interactions of water and solutes with a confining surface dramatically modify the liquid's structure and, consequently, both its thermodynamical and dynamical behaviors, breaking the validity of the classical thermodynamic and phenomenological description of the transport properties of aqueous systems. Additionally, man-made nanopores and porous materials have emerged as promising solutions to challenging problems such as water purification, biosensing, nanofluidic logic and gating, and energy storage and conversion, while aquaporin, ion channels, and nuclear pore complex nanopores regulate many biological functions such as the conduction of water, the generation of action potentials, and the storage of genetic material. In this work, the more recent experimental and molecular simulations advances in this exciting and rapidly evolving field will be reported and critically discussed.

1 Introduction

Water is not only the most important fluid for life, but it also constitutes a system that deeply intrigues us with its anomalous behavior. In fact, despite the simplicity of its molecular formula, water presents more than seventy properties that deviate from that expected for most materials [1–4]. While some of water's unique properties are literally essential for life [5], others have profound effects on the size and shape of living organisms, on their functions and on the physical limits or constraints within which they must operate. The possibility to form up to four hydrogen bonds (H-bonds) leads water to have two characteristic length scales at the molecular interaction level: the larger length scale arises, when the H-bond between two water molecules is formed, while the closer length scale is due to short-range repulsion. Thus, bulk liquid water tends to arrange in a structure built up by an open network of hydrogen-bonded

[a] e-mail: hrcorti@tandar.cnea.gov.ar (corresponding author)
[b] e-mail: appignan@criba.edu.ar
[c] e-mail: jrbordin@ufpel.edu.br

molecules with a different amount of defects depending on the thermodynamic conditions. Such capability to form two distinctive local molecular arrangements, stemming from the directional HB interactions, seems to be at the heart of many of the unusual properties of water [6,7].

For long time, but particularly in the present century, the study of nanoconfined water and aqueous solutions has attracted enormous attention of researchers from different fields devoted to extending the understanding of the anomalous properties of bulk water to the nanoscopic domain.

From a fundamental standpoint, it becomes pivotal to understand how the properties of water are modified by the interaction with a confining surface and to establish the length scale where the assumption of bulk behavior and the phenomenological description of the transport properties of aqueous systems break down.

Understanding the effect of the solid boundaries on liquid properties is challenging for its fundamental implications and its possible applications. Water can be naturally observed under nanoconfinement, as inside biological [8,9] or geological nanochannels [10]. On the other hand, aqueous systems confined within synthetic nanopores are nowadays ubiquitous in several technological areas, such as desalination [11,12], decontamination [13], energy storage [14], heterogeneous catalysis, and graphene exfoliation and transferring [15].

Molecular modeling at distinct length scales from ab initio and semiempirical quantum calculations to atomistic and coarse-grained molecular dynamics simulations has played a key role to understand water properties from the bulk to extreme confinement. Such approaches can be used to interpret experiments and even simulate properties not directly accessible by experiment—as the case of water behavior inside narrow nanopores. In this sense, many of water's basic physical properties can now be explained, at least semiquantitatively, in molecular and structural terms.

In this topical review, we will address several experimental and theoretical/computational aspects of the behavior of water and aqueous solutions under confinement in synthetic and biological nanopore structures. Our work does not intend to cover exhaustively the vast realm of nanoconfined water. (For previous reviews, we refer the reader to ref. [9] and [16].) Instead, we aim at focusing on areas of great current concern within the subject which the authors of this review have been mostly involved with.

In Sect. 2, we analyze the effect of confinement, mainly in silica nanopores, on the solid–liquid and glass–liquid transitions in pure water and aqueous solutions. It is worth to mention that the confinement of water in nanopores is one of the ways to access to the study of the properties of supercooled water in the "no-man's land" (NML) region, although it is a matter of discussion if the properties of supercooled bulk water can be actually approached through those of the nanoconfined one.

The reactive properties of water at the nanoscale will be treated in Sect. 3, in particular the effect of confinement on the value of its dissociation constant. This section adopts a molecular perspective to present the most prominent experimental results concerning the reactivity in confined aqueous phases, on the one hand, and a summary on the simulations devoted to exploring water dissociation in nanopores, on the other.

A central concept that emerges from all these investigations is that effects from size and interface interactions cannot be separately characterized, but are the two sides of the same coin. Then, Sects. 4–7 deal with the dynamic properties of water and aqueous solutions.

Section 4 is devoted to the analysis of the slow dynamics of water confined in hydrophilic nanopores, mainly silica pores, by computer simulations. It is focused on the interplay between thermodynamics and dynamics of confined water, as a possible route to the definitive clarification of the origins of the bulk water anomalies.

In Sect. 5, the structure and dynamics of water under extreme confinement are discussed with emphasis in some recent computational findings and some open questions about the behavior of water when confined between grapheme walls, nanotubes, and nanopores in 2D materials. In turn, in Sect. 6 the transport properties of ionic aqueous solutions are reviewed to shed some light on the main features of the transport properties of water and ionic solutes in nanometric sized pores that have grown rapidly in the last years mainly triggered by their relevance for electrochemical systems of energy storage and conversion and also for water remediation.

In Sect. 7, the structure and diffusion of aqueous solutions of ionic liquids, with different degrees of hydrophobicity in the corresponding anionic species, confined in hydrophobic silica nanopores are analyzed by means of molecular dynamics simulations. Then, Sect. 8 deals with the relationship between local hydrophobicity and non-covalent interactions in a couple of simple illustrative situations: the self-assembly of graphene and graphene-based materials (usually regarded as hydrophobic but exhibiting a rather hydrophilic behavior) and the effect of the local hydrophobicity on the electrostatic interactions operating under nanoconfined water environments, a situation of relevance, for instance, for certain protein–protein association processes.

Finally, Sect. 9 reviews recent modeling efforts on polymer-coated nanopores in aqueous solution, with special focus on the structural behaviors of the coating polymers and their molecular design. Covering both artificial and biological nanopores, this section discusses how bioinspiration guides the development of advanced nanopores, and how the latter in return can be used to advance our understanding of complex biological and pathological processes.

2 Solid–liquid and glass–liquid transitions of confined aqueous solutions

Two different approaches have been commonly used to analyze the state of supercooled water in the "no-man's

land" (NML) region, that is, between the homogeneous ice nucleation at $T_H \approx 231\,K$ and crystallization of a highly viscous liquid to cubic ice at $T_X \approx 150\,K$ [17]. One of these is to confine water in different types of porous materials, while the second one is to mix it with a salt or another glass-forming liquid. For sufficiently small pores (smaller than $\approx 2\,nm$ in diameter) in the first case, and at high solute concentrations in the second one, crystallization can be completely avoided at all temperatures. The fact that in these cases ice formation is avoided is a strong indication that the structural and dynamical properties could be altered as compared to those of bulk water.

It should be noted that the NML is defined for pure bulk water, but not for water in solutions or water under confinement [18], where the structure and dynamics of water within a nanopore cannot be always assimilated to that of bulk water.

In the following subsections, we will analyze how the phase behavior of bulk pure water is modified by confinement of aqueous solutions.

2.1 Solid–liquid transition

Among the various liquid properties affected by confinement, one of the most widely studied is the reduction in the melting point. In pure confined liquid systems, it has been demonstrated that the degree of the melting point depression is inversely correlated to the nanopore radius [19–21], as predicted by the Gibbs–Thompson equation, which connects the change in the melting point, ΔT_m, of a confined liquid in relation to the bulk with the pore radius, r:

$$\Delta T_m = T_m^0 - T_m^c = \frac{2\gamma_{sl} T_m^0 V_s^* \cos\theta}{\Delta H_m}\left(\frac{1}{r}\right) \qquad (1)$$

where T_m^c and T_m^0 are the melting points of the pure component in the confined and the bulk systems, respectively, γ_{sl} is the interfacial tension between the confined solid and liquid phases, θ is the contact angle (usually assumed as 180° if the solution wets the pore surface), V^* is the molar volume of the pure solid, and ΔH_m is the molar enthalpy of melting at T_m^c.

Water is the most studied pure liquid in relation to its freezing/melting behavior under confinement, especially in mesoporous silica [19,22–29]. Equation (1) is valid to predict the melting point depression of ice confined in mesopores with diameters down to about 4 nm. However, for smaller pores, the pore radius should be corrected by a factor t representing the thickness of non-freezable liquid that exists at the pore wall–liquid interface. Thus, an empirical Gibbs–Thompson equation has been used to describe the experimental data, namely

$$\Delta T_m = \frac{C}{(r-t)} \qquad (2)$$

where C takes different values because the surface tension, contact angle, and the enthalpy of melting change with the nature of the solid surface in contact with water. The thickness of the non-freezable layer reported by different authors is also surface-dependent, but most of the data fits lead to values between 0.30 nm [23] and 0.60 nm [19] that, roughly, corresponds to one or two water monolayers.

Though the studies on freezing/melting in confined aqueous systems are no so abundant like in pure water, it has been demonstrated that the Gibbs–Thompson equation can be extended to solid–liquid equilibrium in multicomponent aqueous systems. This is of great interest since it enables to estimate ice formation in more complex aqueous media, such as cells and tissues [30–32].

As an example of a binary non-ionic aqueous system, Liu et al. [33] analyzed how the curvature affects the temperature freezing point of water–glycerol mixtures in equilibrium with the pure solids above the eutectic temperature. The general conditions for solid–liquid equilibrium were derived and then examined, quantifying the effect of the interface curvature on the two solid–liquid equilibrium curves and the eutectic temperature/concentration point. By applying the equilibrium conditions that maximize the entropy of the system and reservoir, subject to the constraints imposed by the system, the following expression for the melting point depression of the mixture with respect to component 1 (glycerol) was derived:

$$\Delta T_m = \frac{2\gamma_{sl} T_{m1}^0 V_{s1}^* \cos\theta}{\Delta H_{m1}}\left(\frac{1}{r}\right) - \frac{T_{m1}^0 \Pi V_{L1}^*}{\Delta H_{m1}} \qquad (3)$$

where the symbols are as in Eq. (1) for the component 1, V_{L1}^* is the volume of the pure liquid component 1, and Π is the osmotic pressure of the solution.

The results show that for radius of curvature between 100 and 1000 nm, both solid–liquid equilibrium curves are not appreciably different from those corresponding to a flat surface. However, the equilibrium temperatures decrease significantly as the capillary radius is 10 nm or smaller, as shown in Fig. 1 [33]. Therefore, this approach provides a promising theoretical method to predict thermodynamic properties of solid–liquid equilibrium across a curved interface in non-ideal multicomponent systems.

In the case of aqueous electrolytes, Burba and Janzen [34] studied the ice melting temperature of dilute aqueous NaCl solutions confined within mesoporous silica, MCM-41 and SBA-15, with pore sizes 3.5 nm and 6.4 nm, respectively. They extended the Gibbs–Thompson equation by adding a term that takes into account the colligative salt effect in the dilute regime,

$$\Delta T_m = \frac{2T_m^0 \gamma_{sl} V_s^* \cos\theta}{\Delta H_m}\left(\frac{1}{r}\right) - \frac{iM_w R T_m^0 T_m^c}{\Delta H_m} m \qquad (4)$$

where i is the van't Hoff factor, M_w is the water molecular weight, and m is the salt molality. However, the

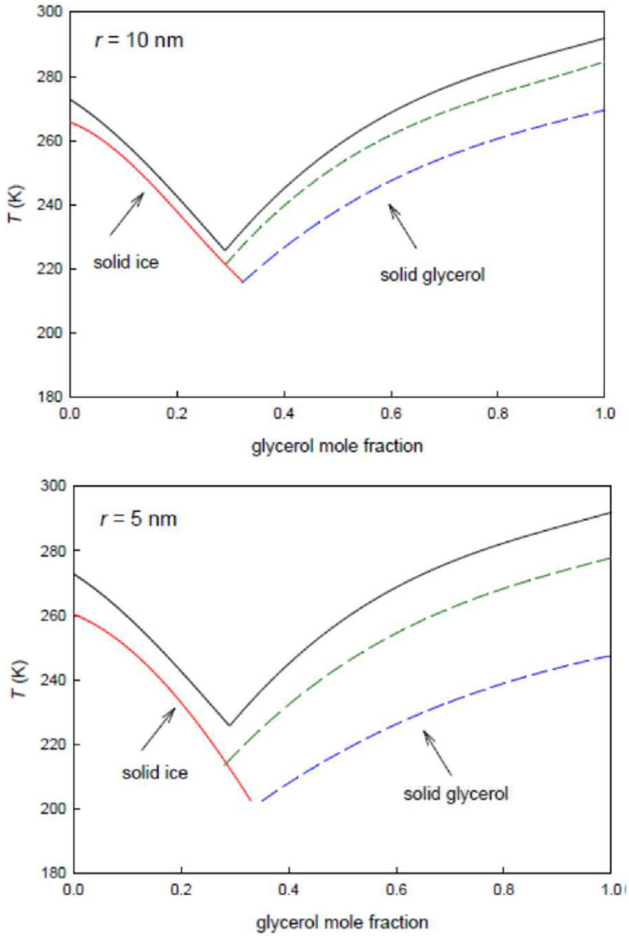

Fig. 1 Predicted solid–liquid equilibrium curves for water–glycerol at 1 bar in capillaries with diameters 10 nm (top) and 5 nm (bottom). Black curves correspond to a flat surface. For the water branch, γ_{sl} was set at 32 mN m^{-1} (red curves). For the glycerol branch, two γ_{sl} values were used: 100 mN m^{-1} (blue curves) and 32 mN m^{-1} (green curves). Adapted with permission from Ref. [33]. Copyright 2017 American Chemical Society

slope of the plots ΔT_m vs m, increases as the size of the pore is reduced, a fact that is not counted for by Eq. (4). A linear dependence of $\gamma_{ice-soln}$ with the salt concentration was proposed in order to match the experimental values of $\partial \Delta T_m / \partial m$ with that predicted by Eq. (4) with $\gamma_{sl} = \gamma_{sl}^0 + m(\partial \gamma_{sl}/\partial m)$. However, the agreement was not good, even when a non-freezable water layer 0.38 nm thickness was considered, probably due to the failure of the solution ideality and full wetting assumptions.

Recently, Koop et al. [35] reported differential scanning calorimetry (DSC) results for the melting temperature of LiCl and $CaCl_2$ aqueous solutions confined in mesoporous silica (MCM-41 and SBA-15) with pore radii between 1.9 and 11.1 nm over a wide range of concentrations (up to 12 mol kg^{-1}). They found that confinement reduces the melting temperature of both electrolytes, except in the smallest pores (r = 1.9 nm for LiCl, and r = 3.2 nm for $CaCl_2$), where the melting temperature is not affected by the presence of solutes. They proposed that this effect could be due to the exclusion of the salts from the smallest pores. However, the surface charge density of the silica is too low to account for a Donnan exclusion mechanism for the concentrated solutions used in this work, and it has also been probed that LiCl is not excluded from mesoporous silica with even smaller pore sizes [36]. Moreover, the selective exclusion of ions from nanopores due to the breakdown of electroneutrality has only been reported in slit-shaped pores where the distance between pore walls is smaller than 1 nm [37].

The model proposed by Koop et al. [35] as an alternative to the Gibbs–Thompson and its extended version (Eqs. 1 and 4) assumes that the solution inside the pore is under a Kelvin pressure (P), which increases with decreasing the pore radius, and that the effect of ions on the structure of water is similar to that of applying pressure [38], in accordance with neutron diffraction studies of near-neighbor network [39,40].

Other approach to the estimation of the change of melting temperature of aqueous electrolyte solutions in nanopores is the secondary confinement hypothesis, that is, the assumption that precipitated salt constitutes an additional confinement for ice/water in the pores. Findenegg et al. [41] applied this approach to explain the change in the eutectic melting point of aqueous alkali chlorides solutions in MCM-41 and SBA-15 silica samples with pore diameters between 4.4 and 8.5 nm.

As it was observed in other salt aqueous solutions, higher melting point depressions were found for samples with small pores, and the largest shifts of the eutectic temperature were found for salts that crystallize as oligohydrates. Thus, in the series KBr, RbCl, CsCl, and NaCl, the highest change in melting temperature was found for NaCl, since it crystallizes as dihydrate at the eutectic point, while the others crystallize in anhydrous form. This behavior is due to the fact that the oligohydrates occupy a larger fraction of the pore, adding a stronger extra confinement as compared to the salts that form anhydrous crystals. It was observed that the decrement in the melting eutectic point, ΔT_E, inside the pore increases with the fraction of volume occupied by the salt in the solid eutectic mixture. A simple expression for the salt-induced melting point depression was obtained considering that the precipitated salt forms a layer of crystallites near the pore wall. In this case, the effective core radius, r', for water crystallization in Eq. (1) is given by $r' = r(1-\phi_E)^{1/2}$, leading to a corresponding increase in the eutectic temperature depression.

For salts with low ΔT_E, the modified Gibbs–Thompson equation underestimates the depression of the eutectic temperature. Thus, an empirical constant correction should be included in Eq. (1), 1.5 K for SBA and 6.1 K for MCM, which accounts for specific ion effects on the non-freezing layer at the pore wall [41].

2.2 Glass transition

The effect of confinement on the glass transition temperature, T_g, of aqueous solutions has been scarcely studied [42–49]. A pioneering work was performed by Johari et al. [42] by resorting to DSC measurements of ethylene glycol (EG)–water mixtures confined in poly(2-hydroxyethyl) methacrylate, having pores 3 nm in diameter. It was observed that for the bulk system, T_g vs. EG molar fraction shows a maximum, which disappears in the confined system. This result was interpreted in terms of a change in the hydrogen bond network due to the confinement. A similar non-monotonic behavior of T_g as a function of the composition was observed in bulk for propylene glycol methyl ether (PGME)–water mixtures [44]. For pure PGME $T_g = 143$ K and increases with increasing water content reaching a maximum at 169 K for water concentration 55 wt%. This behavior was explained considering that in PGME–water mixtures, water increases the size of the relaxing entities in comparison with the corresponding ones observed in pure PGME. For PGME–water mixtures confined in two dimensional Na-vermiculite slits, a maximum value in T_g was also observed as in the bulk system [44]. Therefore, the authors concluded that in this case confinement does not modify the hydrogen bond structure of the PGME–water mixtures.

Swenson et al. [46] performed quasielastic neutron scattering (QENS) and DSC measurements for dipropylene glycol methyl ether–water mixtures confined in MCM-41 in the composition range between 0 and 90 wt% water. In bulk, this system also shows a non-monotonic T_g dependence on composition, which is affected by confinement. Specifically, T_g shows a maximum at 30 wt% water in bulk, while this maximum shifts up to 75 wt% water under confinement. The authors hypothesized that this behavior can be explained considering microphase separation inside the pores, where water molecules hydrate preferably the hydrophilic silanol surface groups of the silica matrix. Also, microphase separation was pointed out to explain the phase behavior of acetonitrile–water mixtures [28] and the T_g composition dependence results of glycerol–water mixtures [43,47] both confined in MCM-41. Broadband dielectric spectroscopy (BDS) and DSC experiments were performed in these MCM-41 samples [43]. For the glycerol–water mixtures, the results show that for the bulk system T_g of pure glycerol decreases with increasing water content (plasticization effect). However, under confinement, T_g is nearly constant for water concentrations between 0 and 85 wt%. The authors hypothesized that this behavior is consistent with the scenario that water molecules have a stronger tendency to coordinate to the silanol surface groups, thereby leaving most of the glycerol molecules clustered in the center of the pores. Thus, the observed T_g should be attributed to the glycerol clusters, while the water molecules coordinated to the silanol surface groups have no influence on the glass transition. For water-rich mixtures, an increment of T_g from 176 K at 85 wt%, up to 187 K at 90 wt% water content was observed, implying that the water molecules bound to the glycerol molecules have an anti-plasticization effect, or glycerol has a plasticization effect on water, breaking up the tetrahedral network structure of water. Based on these findings, Swenson et al. suggested that both geometrical confinement and the introduction of guest molecules (i.e. glycerol) destroy the tetrahedral network structure of deeply supercooled bulk water, which speed up the structural α-relaxation at temperatures close to T_g of bulk water. Consequently, the observed T_g of water-rich glycerol–water mixtures should be considerably lower than that expected for bulk water, that, as hypothesized by the authors, should be much higher than 187 K. These results lead to the remarkable conclusion that the T_g of pure water could be much higher than the value commonly accepted for pure water (136 K) [50]. Moreover, the different structure and dynamics of water in mixtures with high and low water concentrations imply that T_g of bulk water cannot be estimated from extrapolations, of the concentration dependencies of T_g of aqueous solutions containing less than about 80 wt% water.

Recently, Angarita et al. [49] obtained very different conclusions from DSC experiments in glycerol–water mixtures (0–50 water wt%) confined in disordered silica mesoporous samples in a wide range of pore sizes (2–58 nm diameter). Their results show that T_g for pure glycerol and aqueous solutions above the eutectic composition decreases with decreasing pore size. In these samples, only one T_g was observed. However, below the eutectic composition two glass transitions appear, ascribed to the existence of two liquid phases, as observed by Murata and Tanaka [51] in annealed bulk glycerol–water mixtures below the eutectic point. These two liquid phases were related to the two liquid phases of water, HDL and LDL, in the NML region [52].

Angarita et al. [49] also analyzed the dependence of T_g with composition in bulk and confined glycerol–water mixtures by resorting to the Gordon and Taylor equation. The data extrapolate to $T_g \approx 140$ K for pure water in bulk and confined in pores 58 nm in diameter, but decreases in narrower pores, attaining $T_g \approx 112$ K for water confined in pores 2 nm in diameter. These results coincide with those obtained by Soprunyuk and Schranz [53] using the DMA technique and show that T_g of bulk water agrees with the value commonly accepted in the literature, but it differs from the extrapolations reported by Elamin et al. [43]. Moreover, the experiments performed by Angarita et al. [49] do not show evidence of the existence of microphase separation within the pores.

Regarding the glass transition temperature of ionic aqueous solutions confined in nanopores, two recent studies deserve attention. Using DSC, Zhao et al. [45] studied the glass transition of aqueous NaCl solutions with concentrations between 2.8 and 22.6 wt% (just below the eutectic composition) in bulk and confined in nanoporous silica glasses with pores from 56 nm down to 2.6 nm in diameter. They observed that, for small pores, vitrification is observed for all the concentrations, while for larger pore sizes it occurs only for the

smaller NaCl contents. The authors outlined a mechanism of glass formation for dilute aqueous solutions where ice precipitates in the core of the pore, while the remaining eutectic phase, available for vitrification, is constrained between the ice core and the pore walls. Consequently, T_g is constant over the whole composition range since always vitrifies the eutectic phase. Moreover, it was observed that, under the same experimental conditions, KCl aqueous solutions do not vitrify, implying that ion–water interactions should probably play an important role in the process.

Longinotti et al. [48] found that LiCl aqueous solutions with eutectic ($R = 7$) and subeutectic compositions ($R = 9$, 11, 13, and 15), being $R =$ moles of water/moles of LiCl, vitrify over the whole composition range when confined in mesoporous silica (with pore diameters between 2 and 58 nm). It was observed that for LiCl solutions in bulk and confined in pores with diameters above 8 nm, T_g remains almost constant, but samples confined in pores 2 nm in diameter exhibit T_g between 2 and 5 K higher. This increment of the glass transition of the solution by confinement is similar to applying a pressure of up to 100 MPa to the bulk sample. Moreover, it was concluded that the difference in the formation of aqueous LiCl and NaCl glasses is given by the strong interaction of Li^+ ions with the pore silica walls in comparison with Na^+ ions.

Summarizing both subsections, it can be concluded that the effect of confinement in the solid–liquid and glass–liquid transitions of aqueous solutions has not been yet extensively explored in the literature. In the first case, the Gibbs–Thompson equation and its extensions give a reasonable description of the melting temperature depression as a function of pore size and concentration for aqueous solutions. For the glass transition, a general description is hindered due to the fact that different interactions between the components of the mixture with the pore walls, and possible nanosegregation, play a relevant role. Therefore, more works are needed to throw some light on the effect of confinement on the glass transition temperature of aqueous solutions.

3 Dissociation and reactivity of nanoconfined water

The thermodynamics and dynamics of water under nanoscopic confinement have been the subject of a large amount of experimental and computational work. This is, however, not the case for the reactive properties of water at this length scale. In particular, the confinement effect on the value of K_w, the dissociation constant of H_2O, continues to be an unsolved question, despite its importance to design nanostructured catalysts or membranes, or to elucidate the chemistry in aerosols or protein pockets. Beyond speculations based on indirect evidence, this equilibrium has not been quantified from experiments, and simulations provide sometimes contradictory results. This section adopts a molecular perspective to present the most prominent experimental results concerning the reactivity in confined aqueous phases, on the one hand, and a summary on the simulations devoted to exploring water dissociation in nanopores, on the other. A central concept that emerges from all these investigations is that effects from size and interface interactions cannot be separately characterized but are the two sides of the same coin.

Experiments and computational modeling have both shown that nanoscale confinement exerts drastic changes on the physical–chemical properties of water. As discussed throughout this review, almost every single water property examined in confinement has proved to be altered with respect to the one corresponding to the bulk phase.

Despite all these insights reported for the physical properties of nanoconfined water, much less is known about its chemical behavior. Water dissociation and reactivity in these conditions are still a matter of debate, and the body of experimental and theoretical information is scarce and even conflicting at times.

The difficulty to quantify chemical equilibrium and kinetics in nanospaces, be from experiments or from realistic computational approaches, is responsible for this lack of information. A number of surveys focused on three catalytic or reactive processes in aqueous microdroplets and thin films have been reported for some specific cases [54,55] but as yet there is no general understanding of how acidity constants, isoelectric points, or even the water dissociation equilibrium are affected with the reduction of system dimensions. This knowledge is, however, precious to experimentalists, as it is indeed essential to design materials for nanocatalysis, selective membranes, nanofluidics, or single entity electrochemistry of aqueous solutions [56], let aside its fundamental relevance in other areas as atmospheric [57,58] and biological sciences [59] to elucidate processes in aerosols or in protein cavities and membranes. In the present review, we give an overview of the research on this subject, including the effect of confinement on the dissociation constant of water (K_w or the pK_w), which is one of the central questions in this context.

3.1 A microscopic view of water dissociation and lessons from simulations.

The dynamic equilibrium between water and its constituent ions, the proton, and hydroxide ion forms one of the most fundamental processes in acid base chemistry. How this equilibrium changes as a function of temperature and pressure determines the pH of a solution. Similar types of acid–base chemistry reactions also underpin chemical reactions involving proton exchange between the amide backbone of proteins and the surrounding water [60]. Although this forms the basic pedagogy in textbook acid–base chemistry, the molecular mechanisms of this process still remain poorly understood. Atomistic simulations played a key role in decipher-

ing the underlying mechanisms associated with water dissociation. Before delving into their contribution, it is worth spending some time reviewing some of the historical background that motivated a large part of these studies. Many of the ideas behind water dissociation date back to work by Eigen and de Maeyer who proposed a conceptual model for how the proton and hydroxide ion would recombine in solution [61].

Specifically, they argued that beyond the Bjerrum length, the ions would undergo Grotthuss-like diffusion. In a water like solvent, the Bjerrum length, where the electrostatic energy is screened by the solvent and is on the same order as thermal energy, is less than 1 nm. Below this length, Eigen and de Maeyer could only speculate about the underlying mechanisms involved in the reaction of the two ions.

The birth of first principles ab initio molecular dynamics simulations finally opened up the possibility of exploring the molecular mechanisms behind the phenomenological models proposed previously. Specifically, in 1985 Car and Parrinello revolutionized the field of simulation by the introduction of Car–Parrinello Molecular Dynamics (CPMD) which allowed for the first time to observe chemical reactions where the electronic degrees of freedom were explicitly included [62]. One of the first applications of the CPMD method was to study the electronic properties of water and its dissociated ions. The first CPMD simulations of the excess proton and hydroxide ion by Parrinello et al. demonstrated the molecular mechanisms associated with the Grotthuss mechanism which involved the breaking of covalent and hydrogen bonds simultaneously [63]. These simulations showed that the mobility of water ionic defects did not involve hydrodynamic diffusion and provided rational for their enhanced diffusion coefficient compared to ions of similar hydrodynamic radius.

In the late 90s, Parrinello and Sprik attempted to use CPMD simulations to estimate the pK_w. Since water dissociation in the bulk is a rare event happening on average once every 10 hours (characterized by a large activation barrier much larger than thermal energy), one cannot use standard molecular dynamics tools. Thus, to observe dissociation during a simulation one has to use enhanced sampling methods and bias the system along certain degrees of freedom [64,65]. Trout and Parrinello used the O–H bond length of a water molecule and determined the free energy of water ionization along this coordinate [64] using the blue-moon ensemble method.

Although these calculations correctly describe the initial activated process of dissociation, they suffer from the fact that since the ionic defects undergo Grotthuss diffusion, they eventually recombine. Thus, these simulations do not correctly describe the product state of the ionization involving two solvent separated ions. Sprik [65] revisited these free-energy calculations using more sophisticated reaction coordinates involving coordination numbers of putative hydronium and hydroxide ions forming in solution. By controlling the coordination number of a given oxygen instead of the O–H distance, it is possible to induce the transformation of a water into hydronium or hydroxide, depending on whether the coordination number is shifted from 2 to 3 or from 2 to 1. This strategy prevented the issues of recombination of the ions and revealed several stages in the dissociation process. In the first step, the O–H bond increases from about 1 to 1.4 Å leading to the creation of a contact ion pair involving the hydronium donating a strong hydrogen bond to the hydroxide ion. Since this species is highly susceptible to recombination, in order to stabilize the ions, Grotthuss diffusion must separate them with solvent molecules screening the interactions. The absolute value of the free energy for the dissociation reaction is about one pKa unit off with respect to experiments, which is within the expected deviation for the DFT functional employed [65].

In 2001, Chandler and Parrinello combined transition path sampling and CPMD to study the ionization of liquid water [66]. Transition path sampling allows for exploring regions of coordinate space that are high in free energy. These simulations provided more insights into the reaction pathway involving water ionization. Specifically, the authors suggested that water ionization can be considered within the framework of a Marcus theory-like framework where electric field fluctuations from the surrounding solvent act as slow degrees of freedom modulating the potential energy profile for proton dissociation.

Although these early studies provided rich insights into molecular fluctuations involving proton dissociation, they were limited by rather short simulation times and small box sizes. Almost a decade ago, Hassanali and Parrinello re-visited the mechanism associated with water ionization by focusing on the time-reverse process, namely the recombination of hydronium and hydroxide ions [67].

These simulations were conducted with Born–Oppenheimer molecular dynamics and for longer simulation time and also using larger boxes, showing that the recombination appears to be driven by a collective compression of proton wires bridging the ions. Furthermore, there are also specific solvent fluctuations involving water molecules donating hydrogen bonds to the hydronium ion and the hydroxide ion as well, which are important in the recombination process. The hydronium ion is a weak acceptor of a hydrogen bond and is therefore considered to be quite hydrophobic, being stabilized near cavities in water as well as near hydrophobic interfaces such as the air–water interface [68,69]. The role of proton wire fluctuations and more generally the importance of changes in the hydrogen bond topology have subsequently been elucidated in several other studies involving not only acid–base chemical reactions [70], but also proton transfer in the bulk [71] and at interfaces [69] using a wide variety of different atomistic simulations [72].

Besides first principles simulations, there have also been empirical valence bond (EVB) simulations studying the ionization of water and its ionic products. QM/MM EVB-based simulations by Warshel et al. showed a large sensitivity of the dissociation barrier to the explicit inclusion of quantum treated waters [73].

There have also been numerous advancements in using multistate empirical valence bond (MSEVB) to study reactions associated with waters constituent ions the proton and hydroxide in the bulk, at interfaces and confined systems [74,75]. A key contribution of these studies is the ability to move to much larger system sizes and also considerably longer simulations.

Broadly speaking, we envision three main challenges in the theoretical study of acid–base reaction chemistry: (i) the simulation of a broader class of acid–base chemical reactions in water that is not limited to the short simulations and small system sizes, (ii) the development of methods that allow for the determination of the relevant reaction coordinates or order parameters in water, and finally, (iii) devising more efficient methods to explore high activation energy processes not sampled by thermal fluctuations.

In the last decade, there have been several attempts to address some of these challenges and we only highlight a couple of important works in this regard. Several groups have used neural networks (NN) to train potentials that allow for the simulation of water and its constituent ions both in the bulk and at interfaces [76–79]. It will be interesting to see how these NN potentials perform with respect to the thermodynamics of water dissociation predicted in earlier studies. Recently, there have also been some attempts to develop more agnostic approaches to sampling reaction coordinates based on topology, thereby circumventing the need to define coordinates built by chemical intuition which may prevent the system from exploring all possible pathways in complex chemical reactions [80]. The application of these methods to problems involving proton transfer remains an interesting challenge and direction to pursue.

3.2 Dissociation and reactivity in confinement: what do we know from experiments?

For the last 15 years, chemists have been exploring the use of microdroplets as vehicles to catalyze or accelerate the kinetics of chemical transformations [54,81]. This possibility mostly relies on electrospray ionization (ESI) to generate micrometer-size particles dispersed in an aerosol and loaded with the reagents, in combination with mass spectrometry to detect the reaction products [82].

Alternatively, levitation techniques, based either on acoustic waves [83] or in the Leidenfrost effect [84], have also been implemented to produce microdroplets.

Possibly the work by Cook et al. was among the first to conclusively demonstrate an enhancement of reaction rates with respect to the bulk phase [85]. This was shown for the bimolecular reaction of a hydrazine salt with carbonyl compounds in a mixture of water and methanol. Several other studies followed this investigation, showing enhancements of several orders of magnitude, of up to 6 in some cases, for a series of addition, elimination, and other class of transformations involving from simple organic molecules to polymers and metal nanoparticles [83,84,86–89]. The dimensions of the droplets produced and studied through these strategies are typically in the micrometer length scale. In principle, in this range the solution can still be considered a bulk phase. However, right after its formation, these droplets undergo a continuous evaporation that may significantly shrink their volume. Acceleration of reaction rates in these systems is namely explained in terms of the concentration of the reagents in a small volume upon solvent evaporation allowing for fast diffusion and more frequent intermolecular collisions, or the extreme pH changes derived from such evaporation [54,81,85].

In this context, Mishra et al. have recently drawn attention on the distinctive features inherent to electrosprays that can accelerate reactivity but may not be equally ascribed to neutral, pristine water droplets [90]. Specifically, they attributed much of the catalytic effect in the oligomerization of isoprene to partially solvated hydronium ions formed during the rapid evaporation of water. Other factors that have been claimed as responsible for the increased reaction rates are [54,81,91]: (i) enthalpic effects derived from the partial desolvation of the reactants, which increase their potential energy thus lowering activation barriers; (ii) entropic effects arising from an exacerbated ordering of the reagents or the solvent, or from the reduction in the number of microstates [92] all factors which would raise the relative free energy of the initial state; (iii) alternative mechanisms that may proceed at the droplet interface; and (iv) local, abrupt temperature changes originating from energy release or removal, associated with exergonic or endergonic reactions, or with evaporation.

Figure 2 illustrates the free-energy profiles that can be expected for a given reaction involving an ionic species at the interface of a small droplet, in comparison with the corresponding profiles at the bulk and the gas phases. For these types of processes, reaction rates are favored by the surface/volume ratio [81].

An appealing example concerning water reactivity in neutrally sprayed microdroplets has been reported by Lee et al. [89]. In this study, reduction of various organic compounds by water was detected in droplets between 1 and 50 μm in the absence of any catalyst or reducing agents. This reaction is not spontaneous in bulk water, thus establishing that its activation is the outcome of confinement alone. The acceleration mechanism was not elucidated by the authors, though they hypothesized that the answer should be sought in the behavior of H_2O at the air–water interface, e.g., in the exacerbation of the reduction potential of the hydroxide ions to form hydroxyl radicals at the microdroplet periphery [89].

Thin films, microemulsions, and micelles provide alternative means to study the effect of confinement on reactivity [54,81,93,94]. In particular, micelles are spherical supramolecular structures resulting from the self-assembly of amphiphiles (molecules formed by a hydrophilic head group and a hydrophobic tail) in an aqueous media, with sizes in the range of a few nanometers. In a micelle, the polar sides of the amphiphiles, or surfactant molecules, are oriented toward the aqueous

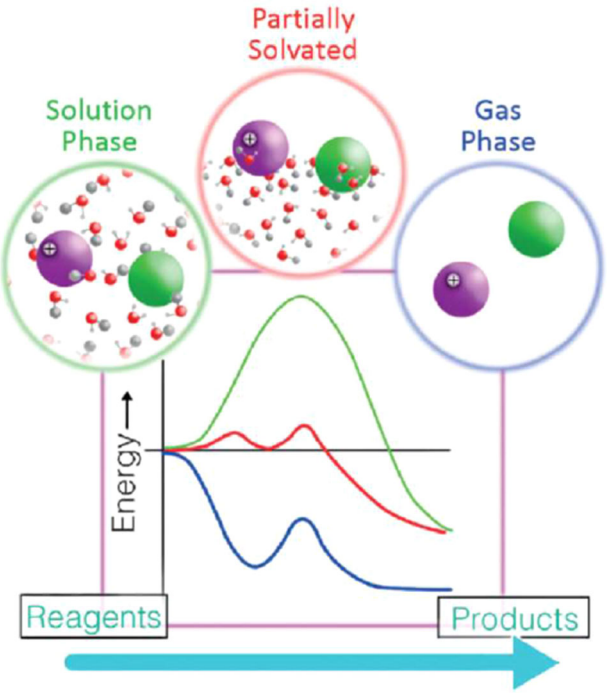

Fig. 2 Schematics of the free-energy profiles for a reaction involving an ionic species in the bulk and gas phases, and under confinement in a small droplet. The large surface/volume ratio favors desolvation thus lowering the activation barrier. Reproduced from Ref. [81] with permission of John Wiley & Sons

phase, while the hydrophobic chains, aligned parallel to their neighbors thanks to van der Waals forces, form the core of the structure. Ever since the 60s, many examples of organic reactions have been reported to occur inside micelles at both accelerated and inhibited rates (see [93,95,96] and references therein). Aside from the factors mentioned above to justify the enhancement of chemical kinetics in microdroplets, other mechanisms have been invoked to explain intra-micellar reactivity: solvation effects, concentration of the reactants on the micelle surface or its interior, and stabilization of transition states through interactions with the polar groups [93].

Reverse micelles, that is, water nanodroplets stabilized by surfactant molecules in a non-polar solvent are of particular interest to this review [97] (see Fig. 3). This kind of organized structures can be found in microemulsions, which are transparent and thermodynamically stable mixtures resulting from the addition of alcohol to a turbid and thermodynamically unstable emulsion [98]. The latter can be formed by mixing water with an immiscible, organic liquid in the presence of an amphiphile [98]. In microemulsions with a high organic/water ratio, the amphiphile molecules stabilize aqueous domains dispersed in the non-polar liquid. The size of these water droplets depends on the concentration of amphiphile, water, and the organic solvent, typically falling in the range from 1 to 100 nm [98].

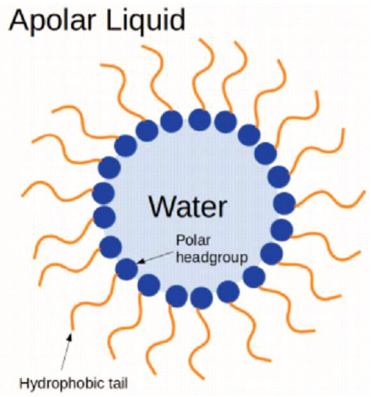

Fig. 3 Representation of a reverse micelle consisting of a core of water stabilized in a non-polar solvent by amphiphile molecules. These kinds of structures can be found in microemulsions, with sizes typically ranging from 1 to 100 nm depending on the water/organic ratio and surfactant concentration

In these environments, the proximity of polar or ionic species has been often recognized as the main factor that modulates the rate of reactions involving charged or polar intermediates. This effect, rather than the shape-selectivity concept attributed to other catalytic assemblies as zeolites or enzymes [55,99], seems to predominate in micellar environments. Thus, the cationic or anionic nature of the surfactants and their proportions is critical to determine acceleration or inhibition [93].

Mitra et al. have pointed out that water dynamics within reverse micelles can be drastically restrained by raising the proportion of an ionic surfactant at the interface [100–102], with strong implications on reactivity [102]. An analogous dependence has been observed for proton transfer kinetics: Levinger and other authors have argued that the dynamics of proton transfer in nanoscopic micelles can vary from bulk-like to a completely different mechanism according to the nature of the surfactant [103,104].

Baret and collaborators have proposed a simple "reaction–adsorption" model to interpret the enhanced kinetics in small droplets in which the reagents weakly interact with the interface, where they react and then the product diffuses back to the inner part of the compartment [105]. Their experimental results for a bimolecular reaction—synthesis of imine—in droplets of a few microns showed a linear dependence of the effective equilibrium and rate constants (K_{eq} and k_1, respectively) with respect to the inverse radius R^{-1} (see Fig. 4).

This behavior was rationalized in terms of the diffusion coefficient D and of the forward and backward rate constants for the bimolecular transformation in the bulk and at the surface of the droplet. From the corresponding kinetic equations, and in the limit of weak interactions and quick redistribution of the product ($R \ll \sqrt{D/k_{-1}}$, with k_{-1} the backward rate constant), the effective equilibrium turns out to be ruled by the

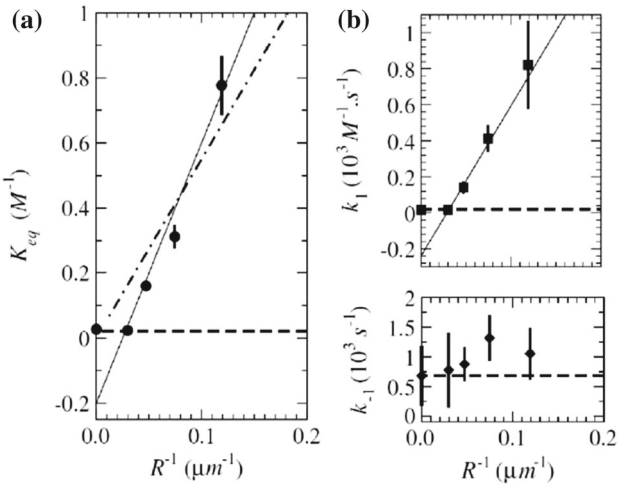

Fig. 4 Results from fluorescence imaging for the reactivity parameters of a bimolecular transformation inside micrometer-size water droplets. The panels show the effect of compartment dimensions on the equilibrium constant K_{eq} (**a**), on the forward reaction rate k_1 (**b**), and on the backward reaction rate k_{-1} (**c**). K_{eq} and k_1 exhibit a linear dependence with the inverse radius of the droplet, which can be explained on the basis of a reaction–adsorption mechanism. Reproduced from Ref. [105] with permission of the American Physical Society

following expression:

$$k_{\mathrm{eq}}^{\mathrm{eff}} = K_{\mathrm{eq}}^{s} \frac{3\delta_A^2}{R} K_r \tag{5}$$

with K_{eq}^{s} the thermodynamic constant for the reaction at the surface, and the parameters δ_{A} and k_{r} depending on the different rate constants [105]. Interestingly, this model predicts a shift in the confined reaction thermodynamics in favor of product formation with respect to bulk water. The authors expect this mechanism to be quite general for chemical transformation assisted by the interface in meso- and nanoscale compartmentalized environments. Thus, for those systems exhibiting a small dimension in comparison with the characteristic diffusion length of the product before it reacts back ($\sqrt{D/k_{-1}} \gg R$), and providing that the reaction occurs preferably at the boundaries—which appears to be a common feature in the realm of confined chemistry [55]—the equilibrium constant and the forward reaction rate would both scale as $1/R$, implying an increase in synthetic efficiency under confinement.

Porous and layered inorganic materials offer a different scenario where water dissociation and reactivity under confinement become critical pieces of a complex puzzle. In an early monograph, Pinnavaia expressed the common belief that the acidity of hydrated cations is intensified in nanoscopic confinement [106]. This assertion was mostly rooted in the interpretation of X-ray and infrared data in layered minerals [107,108]. More recently, the question on water dissociation in confinement has acquired paramount relevance in the development of porous catalyst for water splitting. In such a context, the last couple of decades have seen a proliferation of synthetic nanostructured catalysts designed to favor hydrogen and oxygen evolution reactions by promoting water activation through surface adsorption and dissociation [109–112].

These investigations, however, usually focus on cell performance, and conclusions about the reactivity of confined water are, with few exceptions, driven from indirect evidence, i.e., electrochemical indicators as current densities, capacitances, or overpotentials, seldom attaining a molecular level picture of the interface. Furthermore, the experimental data concerning acidities or surface charges of oxides, clays, and other porous solids are not always reproducible because it depends very much on preparation conditions and characterization techniques [113].

Results on surface charges and isoelectric points are typically the outcome of the average behavior on different exposed facets and geometries. Imaging methods with sufficient spatial resolution to probe the state of water for a local nanoenvironment at the solid–liquid interface are now starting to emerge [114]. Macias-Romero et al. mapped out the confined, curved water–silica interface of a microcapillary using second order harmonic microscopy [115]. In this system, the deprotonation equilibrium at the water–silica interface, $\equiv \mathrm{Si{-}OH} + \mathrm{H_2O} \leftrightarrow \equiv \mathrm{Si{-}O^-} + \mathrm{H_3O^+}$, determines the surface charge density. This study revealed the charge state and alignment of the water molecules at the interface, resolving the local pK_{a} as a function of position and time upon flowing a solution of controlled pH along the capillary. The top panel of Fig. 5 presents a sketch of the molecular structure of the solid–liquid boundary corresponding to different degrees of ionization. In the lower panels, pK_{a} values obtained from image processing are shown, together with curves of the surface potential which reflect the local charge state—at two particular spots on the interface as a function of the pH [115]. A different example can be found in a recent publication by Ali et al., who characterized the hydroxide distribution within the layer adjacent to TiO_2 nanoparticles in a nearly neutral NH_4OH solution employing X-ray photoelectron spectroscopy (XPS) and partial electron/fluorescence yield X-ray absorption spectroscopy [116].

In this article, the Stern and diffuse layers are described, respectively, as a first shell of NH_4^+ cations of ~ 0.35 nm width and a second stretch of OH^- anions extending for other ~ 0.44 nm, that the authors ascribe to a high degree of water dissociation next to the oxide surface. In this diffuse layer, the number of hydrogen bonds per hydroxide anion was found to be three, instead of four as expected for bulk water, denoting the particular structure of the aqueous phase in the proximity of the interface [116].

Finally, we draw attention to an interesting piece of research contributed by Hashikawa et al. [117]. In this study, a single water molecule was confined in a C_{60} derivative. This structure was decorated with

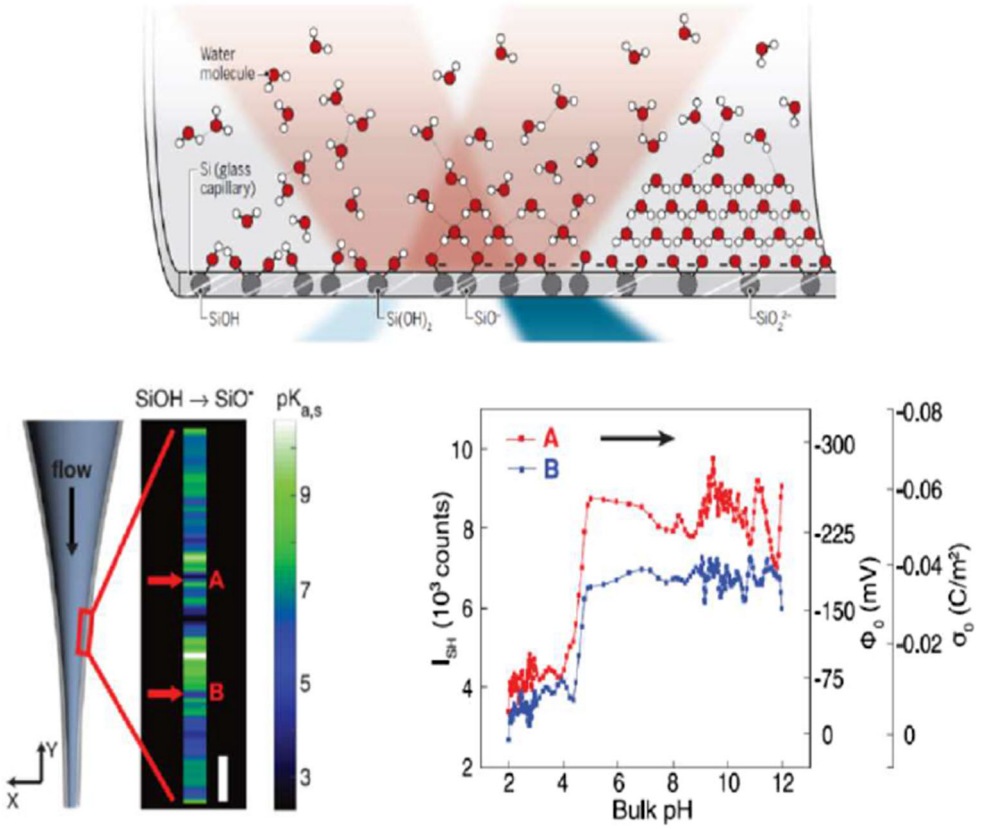

Fig. 5 The H_2O layers and surface charge at a confined water–silica interface of a glass capillary can be mapped with micrometer resolution using X-ray spectroscopies. The top panel displays a cartoon of the aqueous phase for different surface states of charge. The lower panel presents the pK_a values obtained along the longitudinal axis of the capillary, together with curves of the surface potential and charge versus bulk pH at the two spots marked A and B on the left bottom image. Reproduced from Refs. [114] and [115] with permission of the American Association for the Advancement of Science

hydroxyl groups which prevented the release of the water molecule to the solvent through hydrogen bonding. On the basis of NMR and H/D exchange experiments, the authors inferred that the dissociation of the enclosed H_2O molecule was inhibited with respect to the bulk, i.e., the pK_w under these confining conditions turned out to be higher than 14.

Beyond the case studies visited in this section, many other chemical platforms exist capable to modulate reactivity through confinement. These include from zeolites and metal–organic frameworks (MOFs) to covalent supramolecular cages and carbon nanotubes [55,94,118–120], among others. We, however, exclude them from the present subsection since their usually hydrophobic active sites are often better suited for nonpolar species and gases rather than aqueous phases. In any case, beyond the specific examples reviewed above, molecular-level knowledge of the aqueous phase in the vicinity of nanostructured interfaces or interstices is absent from the majority of studies devoted to the optimization of water reactivity through materials engineering. In particular, the dissociation constant of confined water remains a prevailing question that has not been experimentally answered to date. Here, state-of-the-art molecular simulations play a unique role, as it will be discussed in the following subsection.

3.3 Modeling water dissociation under confinement: from layered minerals to carbon nanotubes

Simulation of water reactivity at the molecular level requires methods capable to represent bond dissociation and formation. This can be typically achieved with first-principles electronic structure approaches, as considered in section II, although empirical reactive force fields can be also used to tackle this problem.

Sprik et al. pioneered the application of first-principles molecular dynamics simulations to investigate the reactivity of water at solid–liquid interfaces, with an emphasis on the computation of acidity constants and points of zero charge [121–125]. Whereas the focus of these studies was not necessarily the pK_w in confinement but the chemical equilibrium at the interfaces, they constitute an important precedent in the computational exploration of water reactivity in complex systems and in demonstrating the ability of DFT to interrogate water surface chemistry. The authors were able to iden-

tify the contribution of particular faces or surface moieties to the overall isoelectric point of titania [121], silica [123,124], gibbsite [125], and various clays [122,126], for which experimental measurements typically provide an average result arising from the heterogeneity of the samples. Other DFT studies, sometimes based on the implicit representation of the aqueous liquid phase via a dielectric continuum model, contributed to the microscopic understanding of the water–oxide or water–metal interfaces and the electric double layer [127–134].

Also, dissociative and reactive force fields have been applied to describe the chemical behavior of interfacial and confined water. In early studies, Rustad et al. used a classical potential to investigate the protonation of magnetite–water [135] and goethite–water interfaces [136]. In the latter case, simulation of goethite nanoparticles showed that, in comparison with flat regions, surface edges or asperities develop higher degrees of protonation because they can be more efficiently solvated [136]. In more recent work, several authors carried out molecular dynamics simulations with the ReaxFF force field to examine the dissociation of water in the interstices of layered calcium silicate hydrate gel [137–139,141] the main component of cement and structural model of cementitious materials. These studies showed that water spontaneously reacts in these nanospaces to form Ca-OH and Si-OH groups. The structure induced by H_2O dissociation on the rest of the intercalated water was used to interpret some of the mechanical features of the hydrated material, for example, a hydraulic increase in the shear strength [137] or an enhance in the loading resistance [139]. Some of these studies analyzed the impact of cement composition—which determines the interface charge and polarity—on the fluidity of the confined water [138] and the mechanical properties of the composite [141].

Liu et al. were the first to report the pK_w in confinement from molecular simulations [142]. They studied H_2O inside slit pores of a clay model, of approximate width 1.5 nm using DFT and the Car–Parrinello method. The coordination constraint proposed by Sprik [65] was adopted in combination with thermodynamic integration to sample the free energy of the dissociation process. This constraint is applied on the oxygen atom of a given water molecule, to force a proton release as the coordination number is shifted from 2 to 1 to produce a hydroxide ion. To analyze the effect of chemical structure, several possible configurations were considered for the cations intercalated in this mineral (Na^+ and Mg^{2+}), giving three different layer charge densities of 0 e (neutral), 0.5 e, and 1 e, respectively. Interestingly, the authors found that in the neutral clay, the dissociation constant of the confined free water molecules (those that were not coordinated to a cation) did not significantly differ from that corresponding to the bulk phase. Conversely, in the charged pores the acidity of the free water molecules was shifted down by around 1.5 pK_a units. This enhancement was also observed for the confined coordinated-water molecules when compared with coordinated H_2O molecules in solution. Hence, these results suggest that layer charge is the origin of enhanced acidity in nanoconfined water [142].

In a series of papers, on the basis of CPMD simulations, Marx and collaborators explored the behavior of water and of its ions inside the pores of mackinawite [143–146]. This is a layered mineral with formula FeS which pores constitute a "soft" confining environment, as they do not exhibit strong, specific interactions with the water molecules. In slit pores of width 1 nm, water was seen to organize in a bilayer structure presenting liquid-like dynamics [143]. Interestingly, the authors found that proton transfer was robust with respect to nanoconfinement, which had no impact on the standard Grotthuss diffusion of the excess $H^+(aq)$ [144], while it, however, affected substantially the mechanisms for OH^- transport, overstabilizing the anionic Zundel complex—a transient structure in the bulk phase [145]. In general, the free-energy landscape for this anion proved to be highly sensitive to the width of the pore. This outcome invites to conceive applications based on nanoconfined alkaline aqueous phases in membranes, solid electrolytes, or ion-exchangers where OH^- transport can be controlled by the size of the pores, without affecting the rate of proton conduction [145].

The pK_w at high pressure and temperature ($\sim$20 MPa and 500 K) was computed inside this pore in subsequent work of these authors [146] combining DFT molecular dynamics and thermodynamic integration with the coordination constraint defined by Sprik [65]. In contrast with the previous results by Liu et al. [142], here a shift in the equilibrium toward higher dissociation was reported, equivalent to a drop of roughly two units in the pK_w. This enhancement of the dissociation in confinement was ascribed to a raise in the dielectric response of water along the pore axis. This increase in the dielectric constant would explain, according to this work, the larger value of K_w in terms of a differential stabilization of the dissociation products, the hydronium and hydroxide ions, thanks to a better electrostatic screening in the confined media. In a related article, and using a similar methodology, Muñoz-Santiburcio and Marx conducted a systematic exploration of the reaction paths in the formation of a dipeptide (diglycine) from a single amino acid (glycine) within a pore of mackinawite at elevated pressure and temperature [147]. This chemistry is of relevance in the context of a prebiotic peptide cycle hypothesis. This exhaustive study, which considered seven intermediate species with their possible hydrolysis and back reactions, indicated a general tendency to lower reaction barriers in confinement compared to bulk solution in the same conditions of pressure and temperature. This effect was traced to the stabilization of charged species that provide alternative or smoother paths along the reactive cycle. For example, in some steps a modification from a concerted to a stepwise mechanism involving charged intermediates was detected when going from the solution to the pore [147].

More recently, Perez-Sirkin et al. investigated water dissociation in a (6,6) carbon nanotube, employing DFT molecular dynamics simulations and a free-energy

sampling scheme similar to the one discussed in the studies reviewed above [148]. In this kind of pores, with a diameter of around 8 Å, water molecules form one-dimensional wires where, according to different computations, proton diffusion is much faster than in the bulk phase [149–153]. Allegedly, this feature arises from the molecular alignment imposed by the pore that facilitates proton transfer with almost no reorganization of the hydrogen bonds, at variance with the corresponding mechanism in solution [71,75,154,155].

Under this one-dimensional confinement, the free-energy barrier to dissociation was found to increase by nearly 25%, amounting to a drop of about three orders of magnitude in K_w. The calculated free-energy profiles are displayed in Fig. 6. The highly restrained hydrogen-bond network around the ions imposed by the nanotube was considered to be the cause of this significant inhibition of water dissociation. The right panel of Fig. 6 illustrates the number of hydrogen bonds affecting the hydronium and hydroxide species both in the bulk phase and in confinement. It can be seen that this number, which fluctuates between 3 and 4 for both ions in solution, drops to only 2 inside the carbon nanotube. In the latter, the destabilization of charged species strongly penalizes dissociation, and thus, it is under coordination that dominates the chemical equilibrium in this kind of pores [148].

The incidence of quantum nuclear effects on proton and hydroxide diffusion, as well as on self-dissociation mechanisms, was examined in water clusters and wires resorting to path integral molecular dynamics or related approaches [153,156,157]. In small clusters at cryogenic temperatures, quantum proton tunneling contributes to the stabilization of charge separated, $[H_3O]^+[OH]^-$ ion pairs [157]. On the other hand, isotopic exchange in small clusters showed the predominance of the lighter isotope at dangling bonds, which becomes more significant at lower temperatures as a consequence of the quantum kinetics associated with core and surface atoms [158,159]. In general, quantum nuclear effects augment the amplitude of nuclear fluctuations, provoking the broadening of IR spectroscopic signals [156], but any substantial incidence of these effects on reactivity or dissociation of confined water at higher temperatures is unlikely.

3.4 A reflection on dissociation and confinement

As a summary of the studies analyzed in this section, current experimental and theoretical evidence indicates that confinement sensibly affects the physical chemistry of water and its solutions. This has been namely established for diffusivity and dynamics, transition temperatures, and dielectric response, to mention some of the most prominent properties analyzed.

Are water dissociation and reactivity affected to similar extents under confinement? In answering this question, it is central to recognize that it is often not possible to separate the effect of confinement from that of the interfacial interactions. The experimental literature on reactivity in confined aqueous nanophases reviewed in subsection 2.3 suggests that these interactions have the utmost responsibility for the acceleration or inhibition of reaction kinetics. While physical effects on equilibrium and rate constants derived from system dimensions, as those discussed in references [92] and [105], may have an impact in certain class of reactions, the main factor controlling mechanisms and energetic barriers appears to be the nature of the interface. Polar and charged surface groups, or substituents able to establish specific interactions with H_2O or to stabilize its ions, will have a more disrupting effect on reactivity than that arising from the size factor. As a matter of fact, to consider confinement separately from the immanent surface interactions or surface patterning is just an idealization. Even for clusters or nanodroplets dispersed in the vacuum or vapor phases, the gas–liquid frontier determines the structure and orientation of the outer water layers that may eventually affect reactivity [89].

Boundary effects are imposed as well by hydrophobic surfaces, on which water develops an ice-like character. In any case, confinement and interactions cannot be thought individually, but they are the two sides of the same coin.

At extreme or subnanometer confinement, however, interactions may become a secondary ingredient, and size constraints start to dominate the physical chemistry of water. This is the case of water wires in (6,6) carbon nanotubes, or bidimensional water monolayers in slit pores. Here, the molecular rotational degrees of freedom and the hydrogen bond network are deeply affected, and it is geometry and size that determines the water structure. On the other hand, the physical behavior of confined water rapidly converges to that of the bulk beyond 1 nm from the interface, where interactions are already screened or decorrelated; this means that in pores larger than 5–10 nm, in which the region subject to interfacial interactions represents already a minor fraction of the enclosed volume, “confinement effects” start to fade.

4 Slow dynamics of water in hydrophilic nanopores

Water has a major influence on properties of substrates in different applications in biology, chemistry, desalination, carbon materials, cements. From a more fundamental point of view, it is also of great interest to understand how the properties of water are modified by the interaction with the substrates [160]. Bulk water shows a peculiar behavior upon supercooling with a number of anomalies with respect to other simple liquids [161]. In recent years among the various scenarios that have been hypothesized for explaining these anomalies experiments and computer simulations indicated the existence of a liquid–liquid critical point (LLCP) in the region where supercooling is still experimentally very difficult. This would be the terminal point of the coexis-

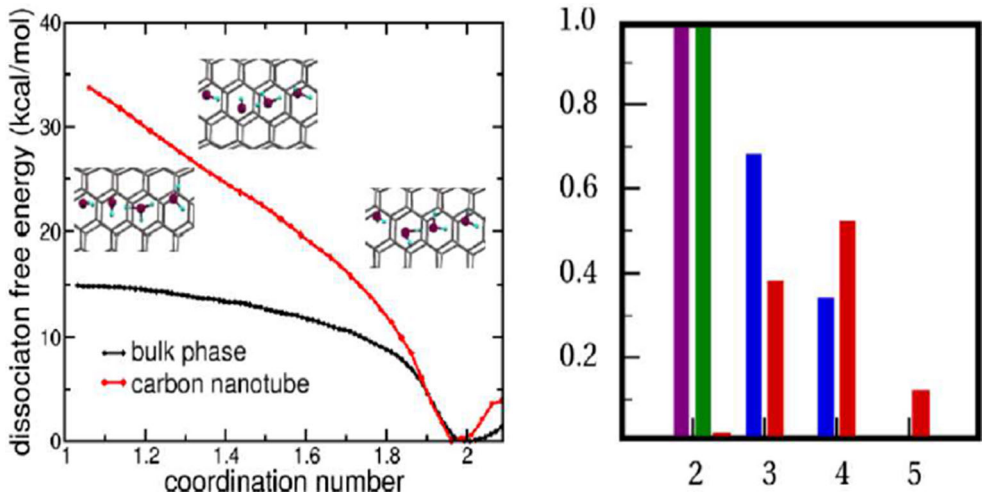

Fig. 6 Left panel: free-energy profiles for the dissociation of water in bulk (black) and confined in a (6,6) carbon nanotube (red), computed from first-principles Car–Parrinello molecular dynamics using the coordination number as the reaction coordinate: 2 and 1 correspond to initial state and final dissociated state, respectively (see text). Configurations sampled along the reaction coordinate are depicted in the insets. Right panel: Histogram of the number of hydrogen bonds formed by the hydronium and the hydroxide ions. Blue: hydronium in the bulk phase. Red: Hydroxide in the bulk phase. Green: hydronium in the nanotube. Indigo: hydroxide in the nanotube. Reproduced with permission from Ref. [148]. Copyright 2018 American Chemical Society

tence of a high-density liquid (HDL) with a low-density liquid (LDL) [6,7,162–166].

The existence of a LLCP implies the presence of a Widom line, the locus of the maxima of the correlation length emanating from the LLCP in the single-phase region [167].

The Widom line was found to have an important role both in thermodynamics and in dynamical properties of supercooled water being connected to the so-called Fragile to Strong Crossover (FSC) that water undergoes upon supercooling [168] both in experiments on confined water and in computer simulations in bulk water, in aqueous solutions and in confined water [169–175]. The Widom line has been recently measured in bulk supercooled water [7,164]. The FSC is present also in hydration water close to the surface of proteins and biomolecules [176–178] and in aqueous solutions of electrolytes [175].

Due to the relevant role of water on hydrophilic substrates and/or in hydrophilic pores, it is important to understand how the static and dynamical properties of supercooled water change when it is confined.

In this section, we focus on the interplay between thermodynamics and dynamics of confined water. Since confining water in restricted geometry often prevents crystallization if the substrate is disordered, making less difficult to perform experiments in the supercooled region, the behavior of confined water can be a possible route to the definitive clarification of the origins of the bulk water anomalies.

We review in the following the main results that some of the authors of this paper obtained in computer simulation of water confined in hydrophilic silica pores.

An important insight on the dynamics of water in confinement was given in refs. [179–183]. By means of molecular dynamics simulations, it was studied water confined inside a cylindrical silica nanopore of 4 nm diameter, closely mimicking the structure of Vycor glass.

The silica nanopore was carved inside a silica glass obtained from simulation by quenching a melted SiO_2 crystal followed by a proper elimination of all silicon atoms with less than four oxygen neighbors, and saturation of dangling bonds of the resulting corrugated inner surface of the pore with acidic hydrogens. Water was simulated with the SPC/E model [184]. For the first time, it was realized how water molecules in close contact with a hydrophilic substrate are able to arrange themselves in a way that makes it possible for the remaining of the water molecules to recover a bulk-like behavior.

The study of the slow dynamics in hydrophilic nanopores was extended by subsequent studies [174, 185–187] with a different model of nanopore, a model representing the ordered mesoporous silica material MCM-41. The cylindrical pore was built with the same realistic procedure as the pore of Vycor and it was carved with a much smaller diameter of 1.5 nm. As in the previous study, the internal surface of the nanopore is corrugated and highly hydrophilic. The pore was filled with SPC/E water. A snapshot of the pore is shown in the upper panel of Fig. 7.

The density profiles of the water contained in Vycor and inside the MCM-41 pore are qualitatively similar. The MCM-41 case is shown in the bottom panel of Fig. 7. Water in contact with the pore surface forms a well-defined layer where the H-bond network is strongly modified (bound water). The bound water screens the hydrophilic interaction so that the internal layers are

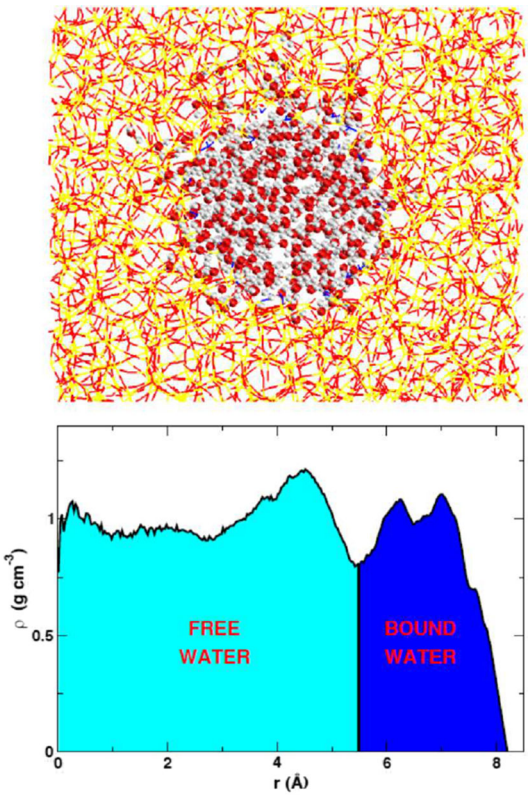

Fig. 7 Upper Panel: snapshot of the MCM-41 system projected in two dimension at $T = 300\,\mathrm{K}$. The box length is $L = 4.278\,\mathrm{nm}$, and the diameter of the cylindrical pore is 1.5 nm. The acidic hydrogens are the inner, darker sticks, the water molecules are the dark and light spheres, and the silica molecules are the outer sticks. Figure from Ref. [186]. IOP Publishing. Reproduced with permission. All rights reserved. Bottom Panel: density profile of oxygen atoms of water confined in MCM-41 along the pore radius with origin at the center of the pore at $T = 300\,\mathrm{K}$. The density of the free water is around $1.0\,\mathrm{g/cm^3}$. Reprinted with permission from Ref. [174]. Copyright 2017 American Chemical Society

composed by molecules arranged in a network similar to bulk water (free water).

The crossover between bound and free water is at the end of the first oscillations at higher density of the density profiles, and it is at a distance of 0.6 nm from the pore surface that corresponds approximately to two water layers. Both in Vycor and in MC-M41, the hydrogen bond network of bound water is distorted and the residence time of the water molecules is found to be dependent on the distance in the region close to the substrate. The first two layers closer to the substrate show in fact high residence times [182,183,185]. The interaction of bound water with the substrate affects therefore not only the structure and the hydrogen bond network, but also the dynamics. Bound water is indeed observed to be nearly immobile, and upon supercooling, the interactions with the substrate lead to a strong decrease in mobility, a subdiffusive behavior, and a very important increase in relaxation times [182,183,185].

Conversely, free water behaves, both in Vycor and in MCM41, as bulk water of comparable density also upon cooling. It is a consequence of these layering effects that free water shows static and dynamical properties that are very similar to bulk water under supercooling.

Through a proper shell analysis of the Self Intermediate Scattering Functions (SISFs), the translational dynamics of bound and free water has been studied in detail separately. While bound water is in the glassy state already at ambient temperature, the free water undergoes a kinetic glass transition. Moreover, the dynamics of supercooled free water is equivalent to that of bulk water [174,179,180,186]. In particular, it follows the predictions of the Mode Coupling Theory (MCT) of glassy dynamics [188] as found for bulk water [189,190].

MCT is a popular theory which is able to describe the slow stretched dynamics of water and other glass-forming simple liquids in the region of mild supercooling. MCT makes precise predictions on the temperature behavior of the α-relaxation time, τ_α, which characterizes the timescale of the structural relaxation of the liquid. The α-relaxation times can be, in general, extracted from the long-time decay of the water SISFs by modeling these correlators with a stretched-exponential function. SISFs of free water were calculated by excluding the bound water contribution and the α-relaxation times of free water were obtained in Refs. [174] and [179] in the case of MCM-41 and in Vycor, respectively.

The α-relaxation time, as well as the diffusive coefficient, $D \sim 1/\tau$, of free water follows upon cooling the power-law behavior in temperature predicted by the MCT:

$$\tau \sim (T - T_C)^{-\gamma} \tag{6}$$

where T_C is the MCT crossover temperature and γ the MCT exponent. A liquid whose relaxation time is described by Eq. 6 is called fragile. The super-Arrhenius relaxation times of fragile glass-formers can be equivalently described through the phenomenological Vogel–Fulcher–Tammann (VFT) relation:

$$\tau \sim e^{BT_0/(T-T_0)} \tag{7}$$

where B is the fragility parameter and T_0 is an ideal glass transition temperature. Equation 7 is widely employed in the analysis of experimental data. The α-relaxation time of the free water in MCM-41 is shown in Fig. 8 as a function of the temperature. The continuous line is a fit of the data according to Eq. 8 [174]. The fit yields $B = 0.25$ and $T_0 = 200$ K. Importantly, the values obtained are similar to the experimental values [169,191].

The fit of the same data to Eq. 6 shows a very good agreement with the simulation data of the free water in the pore and yields: a value for the MCT crossover temperature of $T_C = 195\,\mathrm{K}$ and a value for the power law exponent $\gamma = 3.2$ [186]. These values are quite similar

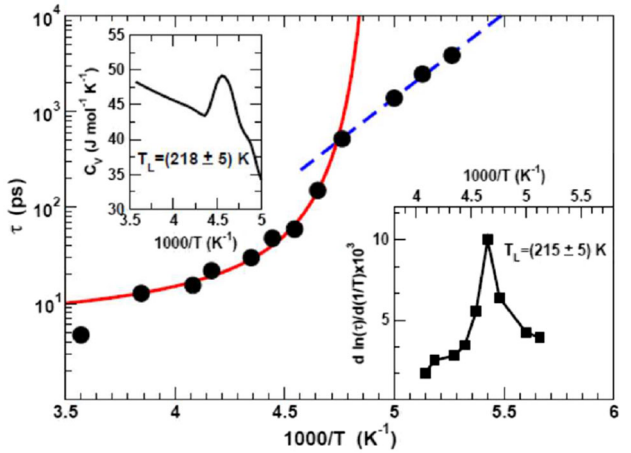

Fig. 8 Main frame: α-relaxation time τ of the free water confined in MCM-41 silica as function of $1000/T$. The continuous red line is the VFT fit via Eq. 7. The dashed blue line is the Arrhenius fit via Eq. 3. The FSC takes place at $T_{\mathrm{L}} \sim 215\,\mathrm{K}$. Upper Inset: specific heat of the system as function of 1000/T showing a peak at the FSC. Bottom Inset: inverse temperature derivative of ln (τ), used to precisely locate the temperature of the FSC. Adapted with permission from Ref. [174]. Copyright 2010 American Chemical Society

to the values obtained by simulations in the bulk phase [189,190]. The dynamics of free water contained in the MCM41 was also intensively tested for other MCT predictions [185], such as the time–temperature superposition principle and the scaling exponents of the theory. All the tests done revealed how free water contained in a hydrophilic confining material follows MCT behavior in the region of mild supercooling.

Upon further supercooling, the MCT no longer holds, and free water undergoes a dynamical transition, where the fragile MCT behavior turns in a regime dominated by activated processes characterized by an Arrhenius law for the α-relaxation time. In this regime, the liquid is called strong and the relaxation time can be fitted with the Arrhenius behavior,

$$\tau \sim \ e^{E_{\mathrm{A}}/k_{\mathrm{B}}T} \tag{8}$$

where $E_{\mathrm{A}} = 34\,\mathrm{kJ/mol}$ is the activation energy of the liquid, again similar to the experimental value [169].

As stated above the transition from a fragile to a strong behavior is called Fragile to Strong Crossover (FSC), and it is observed in the free water in MCM-41 at temperature $T_{\mathrm{L}} \ \sim 215\,\mathrm{K}$ [174,185], in agreement with experiments of quasielastic neutron scattering [169,191] and nuclear magnetic resonance measurements [192,193]. For comparison, bulk water at comparable density shows the FSC at the same temperature $T_{\mathrm{L}} \sim 215\,\mathrm{K}$ [194]. Simultaneously with the FSC of the relaxation time of free water, at T_{L} also a clear peak of the specific heat of the system was observed. The peak of the specific heat can be considered a signature of the Widom line. So, the FSC appears to take place at the crossing of the Widom line also in confinement. This result indicates that the important connection between dynamics and thermodynamics in water found for the bulk [168–173] remains also in confinement.

The interplay between dynamics and thermodynamics and also structure of the free water confined in MCM-41 was further investigated in the simulation study of Ref. [187], in terms of the two-body entropy. The two-body entropy, s_2, is the second-order term of the n-body expansion of the excess entropy. The excess entropy, s_{e}, of a liquid gives an estimation of the accessible configurations, and it is related to the diffusion by the equation [195,196]:

$$D \sim Ae^{Bs_{\mathrm{C}}/k_B} \tag{9}$$

where A and B are two constants.

The excess entropy can be approximated by the two-body entropy s_2, of which it is an upper bound:

$$s_e \sim s_2 \tag{10}$$

It should be noted that both the entropies of water, s_{e} and s_2, independently show anomalous behavior in the phase diagram, correlated with the well-known anomalies of density, diffusion, and relaxation times [197]. The two-body entropy is a particularly important quantity as it can be calculated from the static radial distribution function (RDF), $g(r)$, through:

$$s_2/K_B = -2\pi\rho \int [g(r)\mathrm{In}g(r) - (g(r) - 1)]r^2\,\mathrm{d}r \tag{11}$$

Therefore, under the approximation of Eq. 10, it is possible to estimate the accessible configurations from structural correlations of the liquids. From the radial distribution functions of a liquid, the two-body entropy can be calculated via Eq. 11 and the behavior of the two-body entropy upon supercooling can be linked to the dynamics of the liquid through Eq. 9. The link between entropy and dynamics and in particular in connection with the FSC was already found on bulk water [196,198].

In Ref. [187], oxygen–oxygen RDFs of free water were calculated from simulations of water in MCM-41 spanning a temperature range from 300 K down to 200 K. RDFs were then corrected accounting for the cylindrical geometry in which the water is confined. It was observed also that the first peak of the RDFs of free water is as sharp and high as in bulk water, while the minimum between the first and second peak is shallower in free water with respect to bulk water, allowing some of the molecules of the second shell to penetrate inward. The corrected-RDFs were then plugged into Eq. 11 to obtain the two-body entropy at all the temperatures investigated. The choice of using only the oxygen–oxygen contribution is motivated by the fact that the study aims to relate the two-body entropy to the translational dynamics of water, where the center of mass nearly coincides

to the oxygen atoms. Results are shown in the upper panel of Fig. 14. s_2 decreases upon cooling because the structural order of the system increases.

To connect the behavior upon supercooling of s_2 to the MCT, we can plug in Eq. 6 into Eq. 9, using the approximation of Eq. 10. In this way, we obtain the temperature behavior of s_2 predicted by the MCT:

$$s_2/K_B \sim a + b\,\mathrm{ln}(T - T_C) \tag{12}$$

where a and b are two constants. Equation (12) implies that the two-body entropy logarithmically diverges in approaching the mode coupling temperature T_C.

Equation (12) is tested against the two-body entropy of the free water and it is reported in the upper panel of Fig. 14 as a continuous line. The free fit parameters are the two constant a and b, while $T_C = 195$ K is kept fixed at value extracted from the analysis of the α-relaxation time.

As it is evident from the upper panel of Fig. 9, s_2 follows the predictions of Eq. 12 at higher temperatures and down to the mild-supercooling region. As the temperature goes further down, it deviates from the theoretical MCT prediction and this happens at a temperature around T_L, where the relaxation time τ shows the FSC. It is clear therefore that the FSC marks the deviation from the MCT both in the relaxation times, a purely dynamical quantity, and in the two-body entropy, a thermodynamic quantity related to the structure of water.

In the bottom panel of Fig. 9, the inverse of τ is plotted against the two-body entropy. Continuous line is the fit according to Eq. 9 with the approximation of Eq. 10. It is very well satisfied in the MCT regime, while deviations are observed at temperatures below T_L. The behavior of s_2 can therefore indicate whether the dynamics of the liquid is following the MCT. s_2 gives also evidence of the deviations from MCT, in analogy with the relaxation time.

The results shown in this section evidentiate that the strict relation between thermodynamics and dynamical behavior found in supercooled bulk water is maintained when water is confined, provided the layering effect is taken appropriately into account. In particular, it is found that confined water moving in the inner part of the pores has a MCT behavior in the region of mild supercooling with a FSC that happens upon crossing the Widom line. The calculation of the excess entropy implies that in free water, as it was found for bulk water, the static pair correlation functions give the main contribution to the entropy at least in the MCT region. Below the FSC in bulk water, hopping phenomena intervene to restore ergodicity and erase the divergences of the structural relaxation times and the two-body entropy [173]. This does not imply that below the FSC there is a decoupling between the excess entropy and the dynamics, but it is possible that in the deeply cold regions higher-order terms in the n-body expansion of s_2 are required.

Nevertheless, in water and in free water confined inside hydrophilic nanopores the deviation observed in

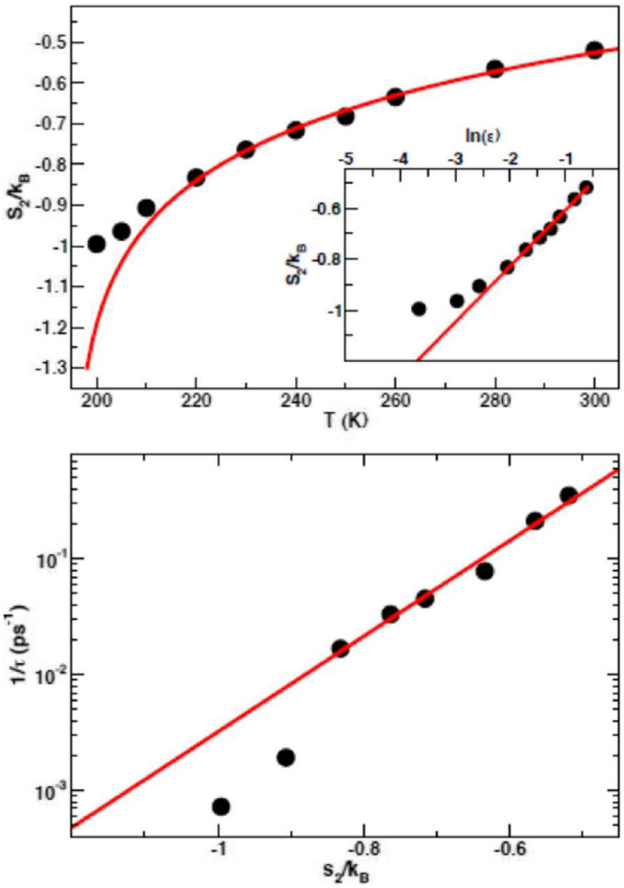

Fig. 9 Upper panel: two body entropy, s_2 for the free water confined in MCM-41 silica as a function of the temperature. The continuous red line is fit to the MCT behavior in Eq. 12 with $T_C = 195$ K. In the inset, the data are shown as function of ln ε, where $\varepsilon = (T - T_C)/T_C$. Bottom panel: inverse of the α-relaxation time, τ, as function of the two-body entropy, s_2 for the free water confined in MCM-41 silica. The red curve is the fit to Eq. 9. Adapted from Ref. [187], with the permission of AIP Publishing

s_2 can be very useful to detect the lower temperature limit of the MCT and the crossover from the fragile to the strong regime of the dynamics. Importantly static RDFs are measured experimentally, and therefore, these behaviors can be tested.

5 Anomalous dynamics in confined water under extreme conditions

In this section, we will discuss some recent computational findings and some open questions about water under extreme confinement. We start discussing the behavior of water when confined between walls—as in the case of water inside a nanopore made by two graphene walls. Next, we overview the dynamics of water inside nanotubes and, finally, the behavior of water and salty water flowing through nanopores in 2D

materials—as the ones observed in graphene or MoS_2 sheets.

5.1 Water under extreme confinement between walls

Calero and Franzese [199], using all-atom molecular dynamics simulations, study the properties of water nanoconfined between rigid graphene plates. They show that water dynamic and thermodynamic properties exhibit oscillatory dependence, with multiple minima and maxima, on the plates separation. At variance with the behavior observed earlier by Krott and Bordin [200] using a core-softened approach, Calero and Franzese find that sub-nm confined water diffuses faster than bulk [199]. Building upon the well-known correlation between layering and dynamics, Calero and Franzese explain this behavior by connecting it to the oscillations of the free energy and the pressure, clarifying the peculiar role of the hydrogen bonds. To mimic the conditions in which confined water is mostly encountered in nature, and in possible applications, Calero and Franzese simulate a system confined between two $24.6°A \times 25.5°A$ rigid graphene plates at separation widths $w/°A = 7, 9, 12.5$ and 14, coupled to a large reservoir of $N = 2796$ TIP4P/2005-water molecules [201] at constant temperature ($T = 300$ K, if not indicated otherwise) in a fixed volume $V = 42 \times 42 \times 51° A^3$. Water interacts with the carbon atoms placed in a rigid graphene configuration through a Lennard–Jones potential with parameters from the CHARMM27 force field [202]. To minimize boundaries effects, they calculate the observables within a region with section $A = 15° A \times 15° A$ and width w. Since the reservoir is at constant N, V, T, the central region is at constant μ, P,T.

As expected, they find that water organizes into layers parallel to the confining walls (Fig. 10a) [199]. Water forms separated layers at well-defined values of w. As we will conclude at the end of this section, these *perfect sizes* of the slit-pore, at $T = 275$ K, are $w_1 \approx 6.75°A$ for one layer; $w_2 \approx 9.5°A$ for two layers; $w_3 \approx 13.5°$ A for three layers, in agreement with previous works under similar conditions [203].

As a consequence of the formation of layers, the number of water molecules, N_w, confined in the central region, i.e., the internal slit-pore *hygroscopicity*, exhibits a step-like dependence on plate separation w, as seen also in [203]. The derivative, dN_w/dw (Fig. 10b), is a measure of the variation of the slit-pore hygroscopicity upon changing w and exhibits a non-monotonic behavior. Minima in hygroscopicity variation occur around perfect sizes w_i for a number i of layers. Maxima in hygroscopicity variation occur at slit-pore intermediate sizes $w_{i,i+1} \equiv (w_i + w_{i+1})/2$, with integer $i \geq 1$. Maxima variations imply that a small increase (decrease) of w induces a large increase (decrease) of N_w, while minima instead imply weak dependence of N_w on w. Hence, maxima are related to an instability of the system, while minima to stable configurations. As we will discuss at the end of this section, perfect and intermediate sizes correspond to minima and maxima in the free energy of the confined water, respectively [199]. Hence, dN_w/dw is a proxy of the free energy.

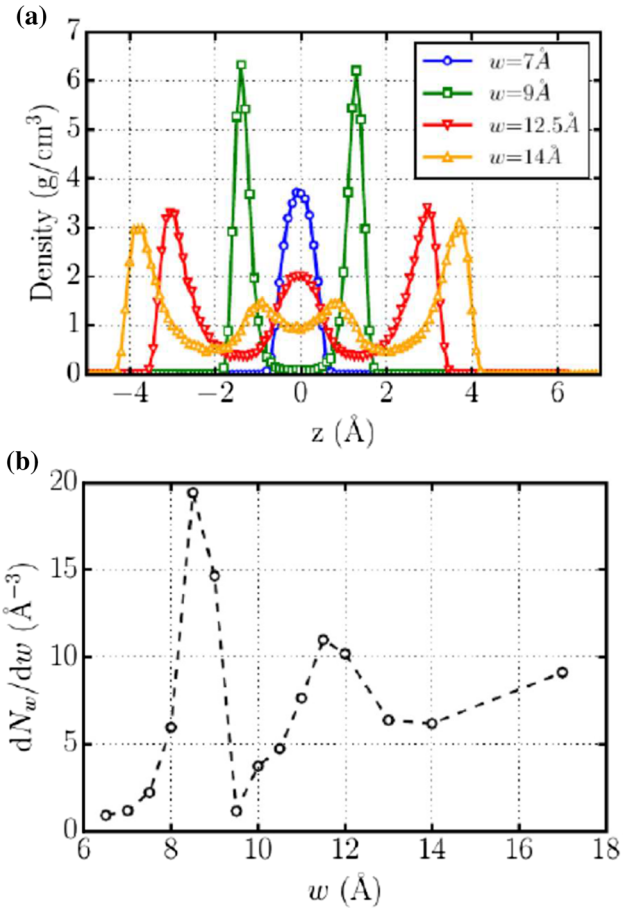

Fig. 10 **a** Water density profile as a function of the distance, z, from the center of the nanoconfined region between the plates, for different slit-pore widths, $w/°A = 7, 9, 12.5$ and 14. **b** Variation of the internal slit-pore hygroscopicity, i.e., the derivative of the number of water molecules, N_w, in the analyzed central region (see text), as a function of w. Adapted from Ref. [199] with permission from Elsevier

Next, Calero and Franzese study the dynamics of water confined in the central region at two different temperatures, $T = 300$ K and at $T = 275$ K, and find that both the diffusion coefficient parallel to the walls, $D_{\parallel}$, and the rotational relaxation time, τ_2, exhibit a non-monotonic dependence on the slit-pore width w (Fig. 11) [199]. At the lower T, with resulting pressure $P = 400$ bar, the water diffusion stops for $w \approx w_2$, due to a phase transition from liquid to hexagonal ice bilayer [204,205]. Hence, water in a graphene slit-pore has a reentrant melting transition around w_2 at $T = 275$ K and $p = 400$ bar, i.e., at ≈ 28 K above the the equilibrium melting temperature of the Ih-ice phase of bulk TIP4P/2005 [206].

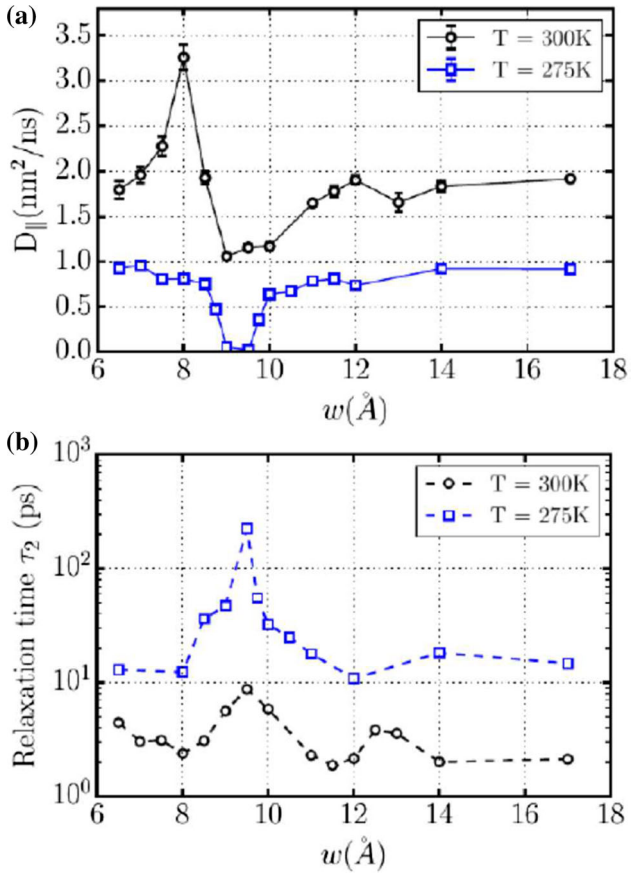

Fig. 11 Dynamics of confined water molecules as a function of graphene-plate distance w at $T = 300\,\mathrm{K}$ and $T = 275\,\mathrm{K}$. **a** Diffusion coefficient parallel to the plates $D_{\parallel}$. **b** Reorientation relaxation time τ_2. Adapted from Ref. [199] with permission from Elsevier

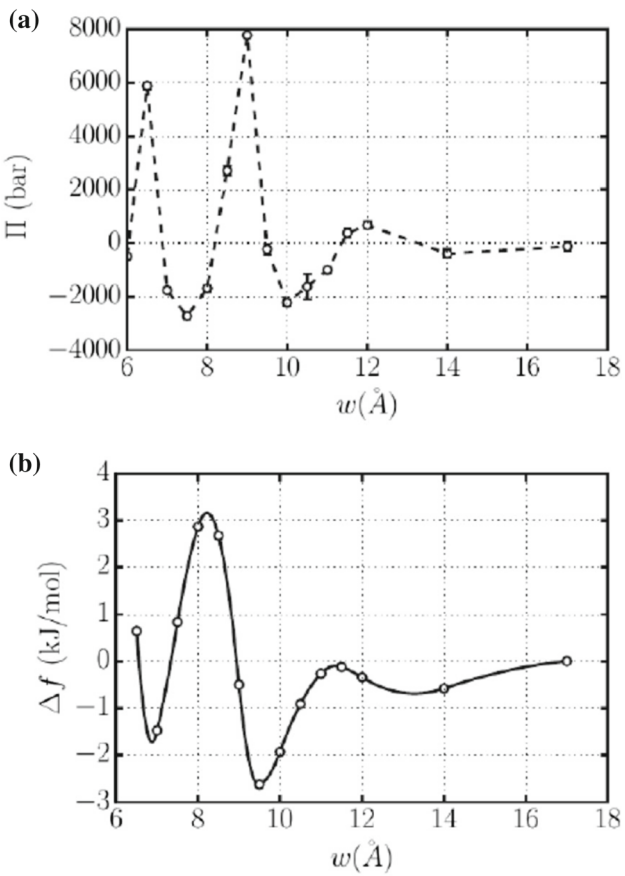

Fig. 12 **a** The hydration pressure Π as a function of the slit-pore width w at $T = 300\,\mathrm{K}$ is vanishing at perfect and intermediate size values of w (see text) is maximum at undersized values of w and minimum (negative) at oversized values of w. **b** Work, per confined water molecule, performed to approach the graphene plates from w_0 to w, as a function of the separation w, for $T = 300\,\mathrm{K}$. Adapted from Ref. [199] with permission from Elsevier

They notice that the non-monotonic dependence of the water dynamics on the slit-pore width w shows a clear correlation with the hygroscopicity variation, $\mathrm{d}N_\mathrm{w}/\mathrm{d}w$, with w. The dynamics is faster at the intermediate sizes $w_{i,i+1}$, where the hygroscopicity variation is maximum, and slower at the perfect sizes w_i, where the hygroscopicity variation is minimum, consistent with the observation that maxima in $\mathrm{d}N_\mathrm{w}/\mathrm{d}w$ correspond to instabilities and minima to stable configurations. Hence, their observation supports the intuitive understanding that unstable configurations increase the mobility, challenging the conclusion that the water-flow enhancement in sub-nm channels is due to an increased structural order of water under extreme nanoconfinement [207] also affects the hydration pressure, $\Pi \equiv p^{\perp}_{in} - p^{\perp}_{out}$, i.e., the difference between the water pressure inside, $p^{\perp}_{in}$, and outside the slit-pore, $p^{\perp}_{out}$, and perpendicular to the walls. They find that Π oscillates between positive and negative values as a function of the slit-pore width w (Fig. 12a). They observe the same behavior at $T = 275$ K (not shown) [199], where the maximum reaches 1 GPa. At both, $T = 300\,\mathrm{K}$ and $T = 275\,\mathrm{K}$, Π is, therefore, of the same order of magnitude of the disjoint pressure found in the experiments [207].

The pressure Π vanishes both at perfect and intermediate sizes, w_i and $w_{i,i+1}$, respectively. This can be understood considering that w_i ($w_{i,i+1}$) correspond to free-energy minima (maxima), i.e., stable (unstable) equilibrium configurations. To understand the maxima and minima in Π, Calero and Franzese calculate the free-energy variation per confined water molecule, $\Delta f(w)$, as the work against the hydration forces to approach the two plates from a large separation, e.g., $w_0 = 17°$ A, to any smaller w [208,209],

$$\Delta f(w) \equiv -A \int_{W_0}^{w} \Pi(w')/N_{w'}\,\mathrm{d}w'. \qquad (13)$$

Because Π oscillates, also $\Delta f(w)$ does (Fig. 12b), with minima corresponding to the perfect sizes of the slit-pore, and maxima to the intermediate sizes, with an absolute minimum, $\Delta f(w) \approx -3.0\,\mathrm{kJ/mol}$, at $w \approx w_2$,

i.e., for a bilayer (Fig. 12b). This is consistent with the stable bilayer hexagonal ice found at lower T at the same size [204,205]. Other free-energy minima at w_1 and w_3 are $\approx 30\%$ and $\approx 60\%$ weaker, respectively, consistent with experiments [210–212], and simulations [203], showing that nanoconfined water, under similar conditions, forms preferentially bilayers and, less frequently, monolayers. The free-energy barrier between the two minima at w_1 and w_2 is twice as large as the thermal energy per mole at the considered T, making unlikely the spontaneous crossing from w_2 to w_1.

Calero and Franzese discuss in detail also the different origin of the two free-energy minima at w_2 and w_1, showing that the first is controlled by the internal energy due to effective attractive forces as in Lennard–Jones liquids [208]. The second at w_1, instead, has an entropic origin, due to the disordering of the water hydrogen bonds under the action of effective repulsive forces, and it is absent in Lennard–Jones liquids [209]. Finally, from the free-energy analysis it is clear that the maxima of hydration pressure occur for slit-pore sizes between $w_{i,i+1}$ and w_{i+1}, i.e., undersized widths, while minima for sizes between w_i and $w_{i,i+1}$, i.e., oversized widths. In conclusion, Calero and Franzese give a rational for recent experiments with water under extreme confinement in terms of the unique properties of water and its hydrogen bond network.

5.2 Water-like liquids under extreme confinement

Krott and Bordin employed a simpler model to study the behavior of water confined under extreme conditions [200]. As a computationally cheaper alternative to atomistic models, core-softened (CS) potentials have been extensively applied to understand the behavior of fluids with water-like anomalies [213–215], although they lack the hydrogen bond directionality that is responsible for the characteristic entropy–energy balance of water [216]. In this way, they simulated a system composed of spherically symmetric CS particles interacting by the potential proposed by de Oliveira et al. [214]. The confining walls were simulated as flat repulsive surfaces, and two distinct scenarios were explored. In the first one, the walls were considered fixed, separated by a distance L_z—as in the atomistic approach by Calero and Franzese [199]—and a second case were the wall were treated as pistons free to oscillate around the equilibrium position given an applied pressure p_z in the confining direction. The presence of two-length scales in the CS potential mimics the two characteristic lengths in water molecules interactions: a further distance that represents the case of formed hydrogen bonds, and a closer length scale, observed when the H bond is broken and the molecules can approach.

The CS study indicated an oscillatory behavior in the dynamical properties when the walls are fixed in space, as we show in Fig. 13a. The location of the minima in the diffusion coefficient is related to changes in the structure, with the particles moving from the second to the first length scale—in other works, the H bonds are being broken and the system is becoming disordered. Interesting, if the walls are free to oscillate, the oscillatory behavior in the CS fluid dynamics vanishes, as we show in Fig. 13b.

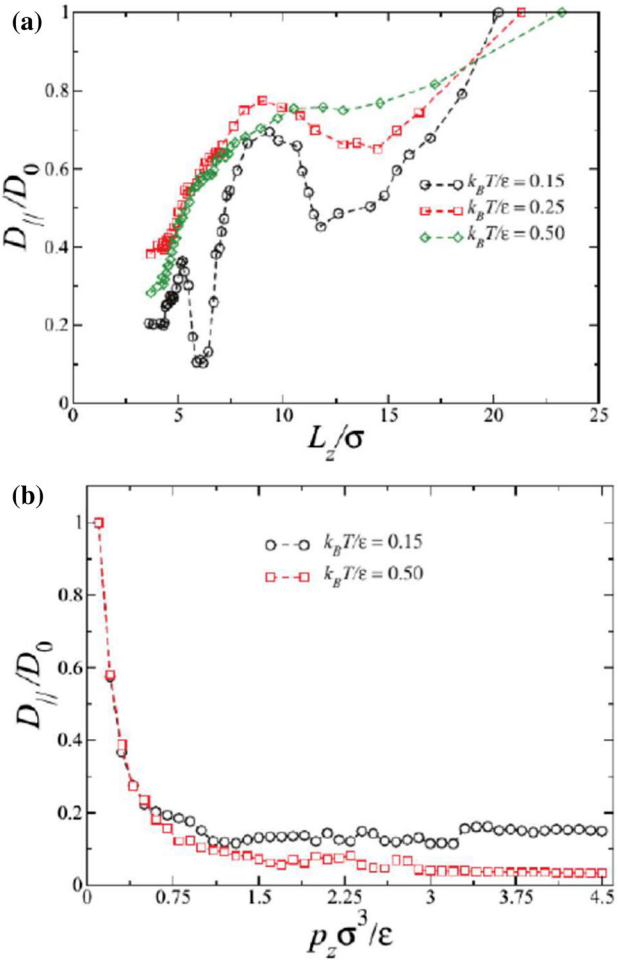

Fig. 13 **a** Lateral diffusion constant normalized by the bulk diffusion as function of the walls separation for the CS fluid confined between fixed walls at distinct temperatures. **b** Lateral diffusion constant normalized by the bulk diffusion as function of the wall pressure for the CS fluid confined between oscillatory walls at distinct temperatures. Adapted from Ref. [200], with the permission of AIP Publishing

This indicates that the wall properties play a major role in the water behavior under extreme confinement. For instance, Krott et al. also have shown that the rugosity of the confining wall can change the phase diagram and influence the water-like anomalies for CS potentials [217]. They observed that the existence of the liquid–liquid transition is sensitive to the rugosity and nanopore width. Likewise, the wall structure prevents the crystallization observed when the fluid is confined inside smooth nanopores, affecting the anomalous dynamic behavior [218].

A more recent work by Yang and Guo has observed how the graphene wall chirality affects the dynamics of water using atomistic simulations [219]. They

found that the chirality-dependent behavior was mainly induced by the variation of the liquid–solid interaction energy barrier when the confined water was driven along different crystallographic orientations of the graphene wall. Therefore, the behavior of water under extreme confinement is extremely dependent from the walls characteristics. In this sense, we explore in the next section how the dynamics of water is affected by the confinement inside different nanopores.

5.3 Anomalous dynamics inside nanotubes

Bulk water presents a unusual dynamical behavior. While for most materials the self-diffusion coefficient, D, decreases with the system pressure (or density), water shows a increase and a maximum in D as function of the pressure [220–222]. This peculiar feature is related to the hydrogen bonding network of water: In the anomalous regions, there is an excess of bonding compared to the non-anomalous regime, with each water molecule forming, in average, more than 4 H-bonds [222]. An alternative explanation, based on the cooperative rearranging regions of the hydrogen bonds, is presented in Ref. [223]

Water under extreme geometrical constraints, as the observed in confinement inside natural and artificial nanopores, will have the average number of H-bonds per molecule suppressed by the confinement. With this, we can expect not only new morphological and structural features, but distinct dynamical behavior, unseen in bulk water. In fact, the seminal works by Martí and Gordillo [223,224], new vibrational bands and frequency shifts, do not observed in bulk, were observed in water confined inside carbon nanotubes (CNTs). This indicated that constrictions imposed by the carbon nanotubes wall can strongly affect the dynamics of water, in ways that are not predicted by the classical fluid mechanics.

The solution of classical equations, as Navier–Stokes, for the dynamics of fluids under cylindrical constriction shows that the flow (or the self-diffusion coefficient D) should decrease as the confinement becomes more extreme [226,227]. So, we can expect a smaller D as the CNT radius shrinks. However, as observed by Mashl et al. [228] and later by other works [229,230], water inside CNT has a peculiar behavior, with two distinct regimes.

Above a certain threshold, D decreases as the radius gets smaller—the usual behavior. At the threshold, where the radius is approximately twice the water molecule size, the water freezes or has a minimum in the diffusion coefficient. These results make sense—as we shrink the tube, the water should stop moving. But the unexpected is observed as the radius becomes even small: D increases as the radius decreases! This anomalous dynamics, observed in molecular simulations, was later confirmed by experiments. For instance, Majumder et al. [231], Holt et al. [232], Qin et al. [233] and Sechi et al. [234] observed a water flow enhanced hundreds of times in comparison with the expected from the classical solutions for CNT with diameter smaller than 2 nm.

As Striolo has shown first [235], and others works extended this discussion [236–238], the huge flow is related to the so-called single-file regime. In this regime, the water molecules assume a linear conformation, with long time lasting hydrogen bonds. Due to the confinement and the hydrophobic characteristic of the CNTs, the water flows almost without friction with the surface. In fact, at this length scale of confinement, the fluid-wall friction plays a major role compared with the fluid viscosity itself [239,240].

One of the main reasons from the deviation from the classical fluid mechanics is related to the continuum regime. Under extreme confinement, as inside CNTs with small radii, the fluid is ordered in layers, i.e., the density is not smooth, with one or more maxima and minima. This discontinuity in the density leads to the failure in the classical solution. As Bordin et al. have shown [241], the flow enhancement and the density discontinuity are strongly connected not only in the single-file regime at narrow nanotubes, but even for wider CNTs. In fact, it was observed in the two layers regime two distinct diffusive regimes. Therefore, each layer has distinct structural and dynamical properties. This computational result was later corroborated by the experiments of Hassan et al. [242] and by Parmentier et al. [243].

A question that arises is: Can we control the enhanced flow of water inside nanotubes? One method to do this is to tune the water-wall interaction by chemical or physical functionalization, making it more or less attractive, changing the CNTs hydrophobic nature [244–247]. As Hummer et al. have shown [248], small changes in the water–CNT interaction can lead to drastic changed in the water filling and confined flow. Striolo [249] showed that controlling the charge discontinuity, introduced by adding hydrophilic oxygen groups on the nanotube wall, can change a non-hydration regime to a Fickian diffusive regime.

Inspirations by biological nanopores can also be employed to tune the water flow inside nanotubes [250–253]. In these cases, the CNTs are designed to be partially hydrophobic, partially hydrophilic. All well, directional modifications inspired in the aquaporins proteins [254] proposed by Zuo et al. [255] are effective to control the water dipole orientation inside carbon nanotubes.

The location and distribution of the hydrophilic sites, controlling the hydrophobic–hydrophilic rate, are a useful tool to control the water flux. As Ramazani and Ebrahimi have shown, a small hydrophobic region in the tube entrance, with lower interaction in comparison with the pristine CNT, might interrupt the flow of water molecules [256]. In fact, the functionalization of the CNTs entrances with distinct molecules can change the flow rate, as Chen et al. [257] have shown by decoration the entrances with hydrophilic or hydrophobic molecules. Increasing the number of hydrophobic sites can increase the flow up to a threshold, as Moskowitz et al. have shown [258]. Above this threshold, the water structure affects the diffusion, preventing the flow

increase, as observed by Bordin and Barbosa [259]. Similar threshold was found by Xu et al. [260]: As the water channel attraction increases, the flow increases rapidly first and then decreases gradually.

Recently, Foroutan et al. showed that rolling a boron nitride nanotube around a CNT can change the water structure and flow inside the CNT [261]. Along the same lines, Bordin, Barbosa et al. have made a series of studies to analyze how the water behaves inside CNT more or less attractive to water. For instance, if the water density is low, the dynamical behavior is not affected by the water–wall interaction regardless the CNT diameter. However, at high densities and low CNT diameter the behavior is completely distinct inside hydrophilic or hydrophobic nanotubes [262]. In this scenario, the Stokes−−Einstein relation, that indicates that the self-diffusion coefficient has to decrease when the viscosity increases, i.e., $D \propto T\eta^{-1}$, is broken inside hydrophobic nanotubes, but maintained inside hydrophilic nanotubes [263]. In agreement with other works [239,240], our simulations indicated that the hydrogen bonds rule the distinct behavior. Another ingredient to add is the temperature—at low temperatures the behavior is the same inside hydrophobic and hydrophilic nanotubes, but at high temperatures the diffusion is affected by the wall interaction [264].

In addition to the size and the presence of functionalization of the nanotube, the chirality of the carbon nanotube also impacts the water mobility at extreme confining geometries. The water inside the (9,9) nanotube freezes, while for the (16,0) zigzag tube which has a similar diameter, water is still mobile. The distinction between the two tubes is that the hydrophobic carbon atoms are arranged at different structures in the armchair when compared with the zigzag tubes what impacts the water arrangements [265,266]. This result seems to indicate that a very important ingredient for the freezing of water is rather the space inside the tube than the presence of hydrophobic or hydrophilic sites.

Nanofluidics is not restricted to carbon nanotubes. Another example of a single-layer material that once wrapped forms a nanotube is the molybdenum disulfide (MoS_2) which consists of a middle-Mo layer sandwiched between two S layers. Differently from graphene, water spontaneously fills the region separated by two MoS_2 nanosheets showing that water inside the bilayer of MoS_2 is more structured when compared with the water within graphene sheets [267]. In the case of MoS_2 nanotubes, water also exhibits a freezing followed by a single line behavior as observed for carbon nanotubes [268]. But the presence of the hydrophobic and hydrophilic sites at the MoS_2 tube induces a non-Fickian regime [268] and a single-file arrangement at smaller diameters when compared with the carbon nanotube system.

Another example of water confinement in nanostructures is the metal–organic systems made of metal oxide clusters and organic linkers with large surface areas. Differently from the carbon nanotubes, they are easy to be produced in controlled sizes, volume, and functionalization. However, even though water is diffusing inside these structures, they present relatively low water permeability when compared with carbon nanotubes [269] what might be due to the roughness of the wall.

Other zeolites as the $AlPO_4$ are also easy to be implemented in nanoscale. They form periodic structures that can be prepared in a highly crystalline form with nanopores of 1.3 nm. These systems present hydrophobic and hydrophilic sites what makes water to form lines at the wall [270]. These water chains diffuse in helicoidal chains of the adsorbed water molecules. This mobility is very different from the observed in water in nanotubes or inside all-silica isomorph, SSZ-24, which follows single linear chains running along the channel axis. The difference is responsible for the mobility of water inside the zeolites to be lower than the observed in the nanotubes or in the silica structure [271].

5.4 Confinement in 2D nanopores and water purification

Nanofluidics of the nanostructures described in the previous section such as carbon nanotubes suggest that water inside such structures can flow at rates greater than predicted by continuum fluid dynamics. This superlubricity can be understood in the framework of the failure of the continuous stress conditions of the classical theory as the nanotube diameter decreases. The same explanation can not be employed in the case of the flow through nanopores where the thickness of the membrane is not consistent with the hydrodynamic approach.

However, these materials exhibit a huge water permeability not observed in macroscopic systems.

For practical applications, such as desalination, membranes made of carbon nanotubes have been limited by low salt rejection [272]. The zeolites, even though present a larger salt rejection, show low water permeability [273]. Therefore, single-layer membranes became an interesting option for these applications.

The first work which analyzed the water performance of water in functionalized graphene was made by Cohen-Tanugi and Grossman [11] using molecular dynamics (MD) simulations. They showed that this material could produce more than 99% with water permeance 2–3 orders of magnitude higher than that of current commercially available reverse osmosis membranes [274,275]. They studied systems with pore of different sizes passivated with with hydroxyl groups and hydrogen atoms. The water permeability observed by Cohen-Tanugi and Grossman [11] and later confirmed by Wang et al. [276] for small pore diameters shows better performance for hydroxyl groups. The cation rejection is larger for passivation with hydrogen atoms, while anion rejection is larger for the passivation with hydroxyl groups [276]. The computational results indicate that graphene membranes are a good option for desalination and possible to be produced experimentally with different pore diameters [277,278] showing an ultrafast water mobility [279].

Even though the functionalization of the graphene layer enhances its permeability, it reduces desalination efficiency [11]. The functional groups create an hydrophilic region at the pore where the water agglomerates what enhances the flux but depending on the type of the atom at the entrance of the pore it also allows for the entrance of salt what reduces the desalination.

Another option for membrane desalination is a single layer of transition metal dichalcogenides, in particular the molybdenum disulfide. Compared with graphene, a MoS_2 single layer has two types of atoms, molybdenum and sulfur. The membrane forms three layers connected: S–Mo–S. Depending on the form, the pore is built and it can expose the Mo, S, or both. MoS_2. These three types of membranes are an interesting strategy for water purification and salt rejection. Simulations show that Mo only pores (when Mo the atoms are exposed in the MoS_2 pore) perform better than the other two options (when S or the S and Mo atoms are exposed in the MoS_2 pore) [280]. This difference was attributed to the local charge differences between Mo and S. However, pore sizes and shapes in both cases (Mo or S exposed) are different, and it is unclear whether a larger exposed charge would enhance water velocity inside the pore, or whether this larger velocity would be solely the result of its size and shape.

What is the most relevant factor for water permeability, size, shape, or charge? Molecular dynamic simulations for pores with fixed size but different charge distributions indicate that the difference in water permeability between the pores with 0.74 and 0.94 and 1.33 nm is larger than the differences due to the presence of charges when the water is not frozen [281]. This result suggests that while the charges at the pores are very important for the salt rejection, they are less relevant for water permeability in the absence of salt.

MoS_2 with pores with diameters from 0.5 to 1 nm shows strong rejection to salt even at simulational high pressures [280]. When mixed with monovalent, divalent, and trivalent salt ions, the nanopore shows a higher rejection rate for multivalent ions, particularly trivalent, for any pore radius, while the rejection is high for monovalent salt ions only for the small pore diameters. The water permeation does not vary with the cation valence, having dependence only with the nanopore geometric and chemical characteristics [282].

In the case of the water permeation, rate is theoretically enhanced by two to five orders of magnitude using MoS_2 compared with commercial polymeric seawater reverse osmosis or zeolite [283] membranes. The MoS_2 shows an improvement in the permeation of 70% when compared with graphene when all conditions identical in the simulations [280]. The combination of different metal dichalcogenide membranes indicates that the transition metal atom shows a larger change in the water permeation when compared with changes in the chalcogen atom due to differences in the polarization of water in the vicinity of the double local charge.

The drawback of using simulations is that they are quite dependent on the specific water and salt models employed. A comparison between the most used models showed that water permeability and salt rejection by the membrane are more influenced by the salt model than by the water model, especially for the narrow pore. Even though water in MoS_2 exhibits a higher permeability and salt rejection than in other membranes, the specific value depends on the particular salt model employed [284].

Experimental realizations of near atom-thickness 2D transition metal dichalcogenides membranes are still rare. Using chemical vapor deposition, Hao Li et al. created a few-layer 2D molybdenum disulfide of 7 nm thick. They observed that this membrane with porous of different diameters ranging from 0.5 to 1.5 nm shows high water permeability (> 322 L $m^{-2} \cdot h^{-1} \cdot bar^{-1}$) and high ionic sieving capability ($> 99\%$) [285].

An additional aspect of the nanopores is the impact of the addition of a second pore. Classical analyses assume a single pore size. Analytical calculations employing hydrodynamic equations showed that pressure drop across the microfilter versus the flow rate indicates that the flow through one pore is affected by the addition of a second pore [286]. This calculation, however, is not valid at the nanoscale. In order to answer the question of the impact of a second pore in the permeability of water in MoS_2 membranes, molecular dynamic simulations for systems with various pore distances were performed. The water flow through two nanopores in MoS_2 membranes does not show any significant hydrodynamic interactions between adjacent pores. The water flow in nanoconfined geometries depends on the local interactions, which is governed by the layered structure of the liquid in the nanopore region. Consequently, the collective effect of hydrodynamic interaction between pores disappears even for very high pressures [287].

As emerges from the results presented in this section, it is worth noting that the behavior of water is fascinating and intriguing from bulk to extreme conditions. Some unique properties from bulk remain, while others are enhanced. Probably, the most promising enhanced property is the anomalous superflow of water in narrow nanopores. As we discussed, recent computational and experimental results show that we have the technology to control the water flow in nanopores and to make nanometric devices with high efficiency in water purification [288,289]. Water structure inside the nanopores plays a key role to understand their mobility [290]. The structure is not only influence by the water properties, as the two length scales evolved in the H-bond crating/breaking process or the water polarization, but the nanopore structure and mobility are a key parameter as well.

The most recent research indicates that chemicals modifications, as the decoration/functionalization of the nanopores with distinct molecules, or physical modifications, as deformations or increase in the degrees of freedom, of the nanopore walls can change and control the water properties under extreme confinement [200,247,259,262,265]. Although there are challenges to overcome, a large advance in the understanding of

water behavior inside narrow pores has been achieved. It leaded to the understanding of natural biological and geological process and is leading to large technological advances. However, a huge question remains open: Will the computational results be confirmed by the experiments? Although advances were made in this direction in recent years [233,234,291–293], most of the facts regarding the nature of water diffusion in nanopores at the molecular scale have been almost solely acquired by computational studies.

6 Transport properties of water and ions under confinement: an experimental approach

The transport properties of water and aqueous ions in natural and synthetic mesoporous materials have practical relevance in a number of fields, such as energy storage and conversion, nanofluidics, catalysis, and desalinization. For this reason, the experimental studies performed to shed some light on the main features on the transport properties of water and ionic solutes in nanometric sized pores have grown rapidly in the last years and they will be reviewed in this section.

Most of the experimental studies on the diffusion of water and ionic solutes have been performed on silica mesoporous materials, because different types of ordered (MCM-41 and SBA-15), with single pore size, and disordered pore network materials, with a wide range of pore size, are available. Thus, the self-diffusion of water was determined in porous silica materials by resorting to the pulsed-field gradient (PFG)—^{1}H NMR [294–300] and quasielastic neutron scattering (QENS) [301–307], while the orientational relaxation dynamics was studied using ultra-fast IR spectroscopy [308]. The inter-diffusion of aqueous salts confined in mesoporous silica in contact with bulk water was also determined by following the depletion of salt concentration from monolithic samples using visible spectroscopy [309–311], or by measuring the increasing electrical conductivity of the water phase [299]. There are also some studies of self-diffusion of water confined in other materials, such as activated carbon [312], metal–organic nanotubes [313], and convex pores of alkylsulfonate amphiphiles [314], while the diffusion of ions confined in water nanofilms and nanodroplets was analyzed by synchrotron X-ray microprobe [315] and dielectric spectroscopy [316], respectively.

The ionic current flowing through a nanopore filled with an electrolyte is affected by the translocation of molecules and ions across it. Thus, individual molecules can be detected by applying a voltage across the nanopore and measuring the current change due to the translocation [317–319]. Nanopores in two-dimensional (2D) materials, such as graphene, molybdenum disulfide (MoS_2), and hexagonal boron nitride (hBN), due to their atomic thickness naturally give spatial resolution at the molecular scale for detecting DNA nucleotides or other biomolecules [320].

In pore size smaller than the Debye length, ions can be transported selectively due to the differences in ion dehydration and chemical and electrostatic interactions with the walls. Thus, new practical applications emerge, such as desalination, pressure retarded osmosis, reverse electrodialysis, battery electrodes, and supercapacitors [321–323]. In this section, we will review the diffusion of water and the diffusional and electrical mobility of ions confined in mesopores materials, where the length of the pore is much larger than its diameter.

6.1 Diffusion of water in porous silica

It is common to relate the inter-diffusion coefficient of a specie i, D_{i}, confined in porous media with that of the bulk, D_i^0, through the expression:

$$D_i = \frac{\varepsilon D_i^0}{\tau} \tag{14}$$

where ε is the material porosity, which accounts for the free space available for the transport of the confined species, and τ is called tortuosity ($\tau > 1$), a dimensionless parameter that accounts for the real length of the pores compared to an ideal linear pore. In addition to this simple geometric effect, the tortuosity factor is affected by the interaction of the species with the pore surface. In the case of the diffusion of confined water and aqueous ions, the hydrophobic or hydrophilic character of the pore walls is a fundamental property to be considered.

In the case of experimental methods that measure the self-diffusion of water or aqueous ions confined in pores, such as NMR and QENS, the porosity should be discarded in Eq. (14), and the ratio $D_i^0/\ D_{\mathrm{i}}$ is a direct measure of the tortuosity factor.

Figure 14 summarizes the ratio $D_i^0/\ D_{\mathrm{i}}$ for ordered (MCM-41 and SBA-15) and disordered porous silica, determined by NMR and QENS, as a function of the pore diameter. A first look indicates that, at the same pore size, the tortuosity factor is much higher in the case of disordered materials, which can be assigned to the local rugosity of these materials that becomes relevant at pore size below 5 nm, where a clear change with the pore size is observed. However, it could not be discarded that the fabrication methods have an influence on the hydrophilic/hydrophobic nature of the pore surface. It is expected that the presence of larger surface concentration of silanol groups on the wall's pore contributes to reduce the mobility of water near the surface, an effect that is exacerbated in small pore materials.

6.2 Diffusion of aqueous ions in porous silica

Takahashi et al. [311] analyzed the pore size effect on the diffusion of aqueous nickel nitrate in mesoporous silica by UV−−visible spectroscopy and observed that,

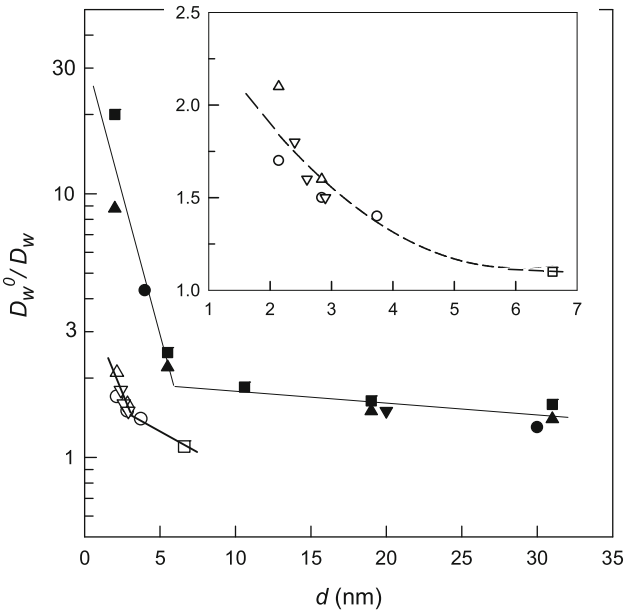

Fig. 14 Tortuosity factor for the diffusion of water in ordered (empty symbols) and disordered (full symbols) silica as a function of the pore size: (●) Vycor/Bioran glass [295]; (▲) CARIACT [296]; (■) CARIACT [299]; (▼) GelSil [300]; (○) MCM-41 [301], (△) MCM-41 [302]; (▽) MCM-41 [307]; (□) SBA-15 [306]. The inset shows a zoom of the small pore ordered silica, and the lines are a guide for the eye

for materials with pore diameters larger than 5 nm, the tortuosity was close to unity and independent of the pore size, while it increases rapidly with decreasing pore diameter because of the reduction in the microscopic mobility of the ions due to their interactions with the wall. A similar trend has been reported by Kunetz and Hench [310] for the diffusion of chromium nitrate in porous sol−gel silica monoliths, with tortuosity increasing suddenly in pores smaller than 3 nm. Koone et al. [309] reported diffusion coefficients for Er^{3+} ions in the 4.2 nm diameter pores of a sol−gel glass without discussion about confinement effects.

The mobility of ions confined in nanopores is expected to be determined by ion−−surface interactions and by the structure and mobility of water, which depends on the nature of the water−surface interactions. However, little attention has been paid in the literature to the experimental study of the coupling of ionic and water diffusion in mesoporous materials over a wide range of pore sizes. Corti et al. [299] studied the diffusion of aqueous alkali chlorides electrolytes (LiCl, KCl, and CsCl) in silica mesoporous materials with average pore diameters between 2 and 58 nm by resorting to the measurement of the electrical conductivity of well-stirred water in contact with macroscopic mesoporous samples filled with aqueous electrolyte solutions. The diffusion of water inside the pores follows the same trend with pore size that the diffusion of electrolytes indicates a coupling between the ions and water diffusional mobilities.

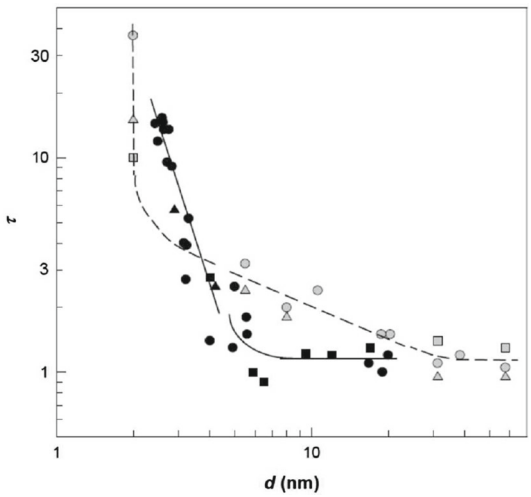

Fig. 15 Tortuosity factor for the diffusion of aqueous ions confined in mesoporous silica. Symbols: Li^+ (●), K^+ (▲), and Cs^+ (■) in CARIACT [299]; $Er(NO_3)_3$ and $Nd(NO_3)_3$ (▲) [309] $Cr(NO_3)_3$ (●) [315], and $Ni(NO_3)_2$ (■) [311] in sol–gel glasses. The lines are a guide for the eye

The tortuosity effect on the diffusion of all studied electrolytes and water shows a monotonic slight increase with decreasing diameter for pores larger than 5 nm, while the tortuosity factor increases markedly for smaller pores, as shown in Fig. 15. In microporous and mesoporous silica with pore sizes below 10 nm, the tortuosity factor of Li^+ ion is much larger than those for K^+ and Cs^+ ions, since its diffusion is hindered by a stronger electrostatic interaction with the ionizable silanol groups on the pore wall, and also, larger than that for water diffusion which it is retarded by a weaker hydrogen bond interaction with the silanol groups. The differences in tortuosity factors among alkaline chlorides and water become negligible for pore sizes larger than 10 nm. The spin−lattice relaxation time measurements of ^{1}H-water and Li^+ ions confirm this behavior [299].

6.3 Ionic conductivity under confinement

Most of the experimental studies of ion transport in nanopores usually focused on the conductivity of aqueous salts, mainly KCl, as a function of the concentration and pore size, although some of them include the analysis of selectivity and ion rectification effects. The conductivity of salts in nanopores is measured on well-defined geometries that allow comparing the results with those obtained for the bulk aqueous solutions.

Stein et al. [324] were the first to observe that aqueous KCl confined in silica rectangular channels 70–1000 nm thick exhibits a remarkable degree of conduction at low salt concentrations that departs strongly from bulk behavior. The conductivity of the confined salt decreases with decreasing concentration following the bulk conductivity, but below a concentration, close to 0.01 M, the conductivity reaches a constant value

with it is independent of the salt concentration, c, and the channel thickness, h. Thus, at low KCl concentration the conductivity in the channel exceeded the expected on the basis of the bulk conductivity by orders of magnitude. This behavior could be explained by considering the effect of the negative charge density, σ, on the channel wall that rejects the Cl^- coions and attracts the K^+ counterions forming an electric double layer. In the low concentration regime, where $\kappa h \ll 1$ (κ being the Debye screening length), and $|\sigma| \gg ech$, the conductivity is independent of c and h [324].

A similar concentration dependence of the conductivity in confined electrolytes was found for HCl confined in ≈7–8 nm silica nanochannels [325], for KCl, NaCl, and HCl confined in 2 nm glass nanochannels [326], for NaCl confined in silicon nitride nanopores between 2.1 and 26 nm in diameter [327], for KCl confined in cylindrical boron nitride nanotubes with diameters in the range 15–40 nm [328], and for KCl confined in silicon nitrides pores in the range 1–3.2 nm [329]. In the mesoporous system, that is, those with pore size between 2 nm and 50 nm, the saturation conductivity of the electrolytes increases when the pore size decreases.

The saturation conductivity in dilute confined electrolytes is a consequence of the increasing contribution of the surface conductivity in comparison with the bulk conductivity. The Dukhin length, defined as the ratio between the surface concentration and the salt concentration outside the pore or channel, σ /c, is a key parameter, since conductivity saturation will occur as the channel width or pore diameter is smaller than the Dukhin length [330]. The surface conductivity that predominates in the low concentration regime depends inversely on the size of the confinement [330], which explains the results above mentioned.

Ma et al. [327] observed that, contrary to the common expectation, ion mobility is reduced with respect to bulk behavior at high electrolyte concentrations. This behavior is due to the combined effects of the low mobility of surface bound ions and enhanced pairing and collisions between partially dehydrated ions of opposite charges. The study concludes that the ion mobility in nanopore/channels continuously decreases as the electrolyte concentration increases.

What are the main features of ionic transport through nanopores with sizes < 2 nm (micropores according to the IUPAC nomenclature)?, particularly subnanometer pores with diameters approaching the hydration size of the ions. Although this subject has been addressed mainly through molecular simulation, some recent experimental studies have shed some light on the mechanics involved.

Esfandiar et al. [331] fabricated atomically flat angstrom-scale slits, with dimensions approaching the size of small ions and water molecules, by separating two graphite, boron nitride or MoS_2 crystals with either a bilayer of graphene or a monolayer of MoS_2. The assembly was kept together by vdW forces, and the resulting channels had a height of ∼7 Å, given by the vdW thicknesses of the separators, comparable to the diameter of aquaporins. The results for KCl conductivity were similar to that observed for channels with higher heights; that is, saturation is reached at low salt concentration. The saturation conductivity increases in the order MoS_2 > BN > graphene, following the decreasing order of surface charge. The authors also analyzed the conductivity of various chlorides and observed that their conductivity decreases monotonically with the hydration diameter of the cation, following the order $K^+ > Na^+ > Li^+ > Ca^{2+} > Mg^{2+} > Fe^{3+} > Al^{3+}$. The fact that there is no abrupt steric exclusion when the hydrated cation is larger than the slits height implies that the ions are able to partially shred or flatten their hydration shells. Indeed, the reduction of the cation mobility scales with the hydration energy, and they decrease by a factor 10 from K^+ to Al^{3+}. Contrarily, the mobility of the Cl^- is almost constant for all the salts and it is three times smaller that in bulk solutions, as a consequence of the presence of OH^- groups on the surface of the hydrated anion, which interacts stronger than cations of the same size (as K^+ ions) with the graphene and boron nitride walls [331]. Similar results regarding the reduction of mobility of cations in sub-nm pores were reported recently by Rigo et al. [332] in fabricated nanopores ranging in diameter from 0.28 to 1.0 nm, sputtered through a thin (7–12 nm) silicon nitride membrane.

Ionic transport in CNT of molecular dimensions is dominated by the peculiar dynamics properties of water when confined in such media, as discussed in Sect. 5.3. Water confined in hydrophobic nanopores of diameter similar to its molecular size demonstrates slip-flow at the walls, reduced viscosity and increased proton transport rates. Thus, Noy et al. [333] have shown that 0.8-nm-diameter carbon nanotube porins, which promote the formation of one-dimensional water wires, can support proton transport rates exceeding those of bulk water by an order of magnitude. However, in nanotube porins 1.5 nm in diameter, proton transport rates become comparable to bulk water. Interestingly the proton transport rates in these narrow nanotube pores also exceed those of biological channels and Nafion, which opens the application as proton conducting membranes for PEM fuel cells. It is worth to note that Nafion nanofibers 400 nm in diameter obtained by electrospinning exhibits proton superconduction due to the alignment of the cylindrical micelles formed by the polyelectrolyte chains having a central core of water of around 2 nm in diameter [334]. In this case the nanoconfinement is highly polar but it also seems to promote the Grotthuss mechanism of proton conduction.

Lindsay et al. [335] have shown that ion current through single-walled CNT (SWCNT) 1.7 nm in diameter is about two orders of magnitude larger than predicted from the bulk resistivity of the electrolyte. The vast majority of the current is carried by electroosmosis, with only a small contribution from the electrophoretic and diffusion currents. The very large electroosmotic current arises from the nearly frictionless flow of water inside the SWCNTs. The system displays stable p-type ionic transistor characteristics, showing that the charge carriers are cations when a KCl electrolyte is used. Ion

transport is turned off by the application of a positive gate bias, indicative of a negative charge on the channel. The magnitude of the excess current and its control by a gate electrode are correctly predicted by the Poisson–Nernst–Planck–Stokes equations.

In summary, the experimental approach for understanding the ionic transport through nanopores driven by concentration or electrical potential gradients have shed some light on the main features governing such processes.

However, further studies are needed to elucidate their fundamental aspects, particularly in aqueous electrolytes confined in pores with size below 2 nm. This type of extreme confinement is accompanied by unusual physical behavior such as the breakdown of electroneutrality, which has been reported for electrolytes confined in 0.9 nm carbon nanopores using NMR techniques [336].

7 Aqueous solutions of ionic liquids under nanoconfinement

Room temperature ionic liquids (RTILs) are molten salts that combine organic cations—such as alkyl-substituted imidazolium, pyridinium, or phosphonium groups—and organic or inorganic anions ranging from simple ionic species (e.g., Cl^-, Br^-) up to more bulky and hydrophobic moieties, like BF_4^- or PF_6^-. Compared to classical organic solvents, these liquids exhibit several appealing physicochemical properties that make them suitable to host reactive processes in an "environmentally friendly" fashion. The list includes: low melting point, low volatility and flammability, high chemical and thermal stability, and high polarity, to cite a few relevant characteristics. The incorporation of water to ionic liquids leads to a wide variety of new phases determined, to a large extent, by the range of miscibility of each particular salt. In the vast majority of cases, the miscibility is controlled by the corresponding anion [337]. From a microscopic perspective, the structure of these ionic phases is far from being simple [337–343]. In many cases, the amphiphilic nature of the cationic species leads to spatial heterogeneities at the mesoscopic level involving clustering [344–346] and self-organization phenomena [347–352]. Aqueous solutions of ILs present a series of practical applications in a variety of areas such as extraction processes in analytical chemistry [353,354], synthetic routes [355], and cooling cycles [356].

The combination of an inorganic porous material filled with a ionic liquid solution gave rise to a novel class of hybrid materials, often called ionogels, with promising applications. The development of such materials is technologically challenging because the properties of the ILs are modified upon confinement [357,358].

The presence of a macroscopic solid–liquid or gas–liquid interface brings more complexities in the microscopic scenario. Most notable are those associated with local concentration fluctuations [359–362] and enhancement of orientational correlations involving different molecular groups at the vicinity of the interfaces [363–365]. Significant changes in the structural and physical properties of RTILs confined into nanoporous matrices have been reported, which could strongly affect the behavior of devices employing ionogels. In particular, RTILs in strong confinement conditions can undergo a liquid to solid-like transition, which may dramatically affect their physical properties like the ionic mobility [366,367], the viscosity, and the electrical properties, and may give rise to interesting catalytic applications [368–370]. The incorporation of a liquid into a solid host material generally reduces the overall liquid mobility, resulting in smaller diffusion and lower ionic conductivity [371,372]. Therefore, new strategies must be evaluated in order to minimize those drawbacks. The main scientific challenge in this area consists in the development of new materials that are able to maintain a high conductivity when the ionic liquid is confined. Technological applications would require, in addition, the stability of the system properties under high temperatures and pressures, such as in the case of fuel cells [373].

It is also of interest to examine how the resulting structures of these binary solutions can be even further modified when they are confined within pores or slits [374,375] with nanometric linear dimensions. For example, using a combination of differential scanning calorimetry and spectroscopic measurements, Singh et al. [376] detected changes in phase equilibria of imidazolium-based ionic liquids confined in a silica gel matrix with nanometric dimensions. In addition, Coasne et al. [377] have examined the structure and dynamics of RTILs, tightly bound to the walls of silica pores at different filling conditions. Iacob and collaborators have reported results from dielectric spectroscopy and magnetic resonance experiments that reveal up to tenfold reductions in the diffusion coefficients of ionic liquids in oxidized nanoporous silica membranes [378]. Yet, the information about microscopic characteristics of confined water/RTIL solutions is still very scarce. A large body of studies have reported slower dynamics of ionic liquids confined within nanocavities or silica slabs [379]. In contrast, theoretical methods have also predicted the opposite trend, i.e., a faster dynamics of ionic liquids in nanocavities. Namely, Shi and Sorescu [380] have investigated the sorption of CO_2 and H_2 into a ionic liquid confined within carbon nanotubes. Their predictions show self-diffusion coefficients that are about 1–2 orders of magnitude larger for the trapped ionic liquid than for the corresponding bulk phases. Experimental evidence of dynamical enhancements upon confinement has also been reported. An increment in the diffusivities by more than two orders of magnitude has been measured by Iacob et al. [381] using spectroscopic techniques in ionic liquids contained in nanoporous membranes. Neutron scattering experiments performed by Chathoth et al. [382] have shown that ionic liquids confined in mesoporous carbon have diffusion coefficients that are comparatively larger in the confined state. Similar diffusion enhance-

ments have been measured when the ionic liquids are confined in carbon nanotubes [383,384]. Besides, taking into account the specific molecular details of the confining cavity, the increment of ionic mobility in confined phases is attributed to changes in ion packing due to the reduction of the density of the trapped liquid in the pore. In the absence of strong ionic liquid/surface wall interactions, the dynamics seems to be controlled not only by thermal but also by density fluctuations. A complete review of computational studies on RTILs under confinement within graphene and carbon nanotubes has been recently published by Foroutan et al. [385].

In the following we review the main results obtained by a series of molecular dynamics simulations involving aqueous solutions of imidazolium-based ILs confined within cylindrical silica pores with radius ranging around to 1–3 nm [371,386]. In a previous work, aqueous NaCl solutions have been examined within similar pores [387]. Although the two systems could be cast within the same conceptual framework, the latter simulation results revealed that the structural and dynamical features of the confined RTIL solutions differ from those observed in simpler aqueous electrolytes at a qualitative level. The case of a pure RTIL confined within functionalized silica cavities is also discussed for completeness [386].

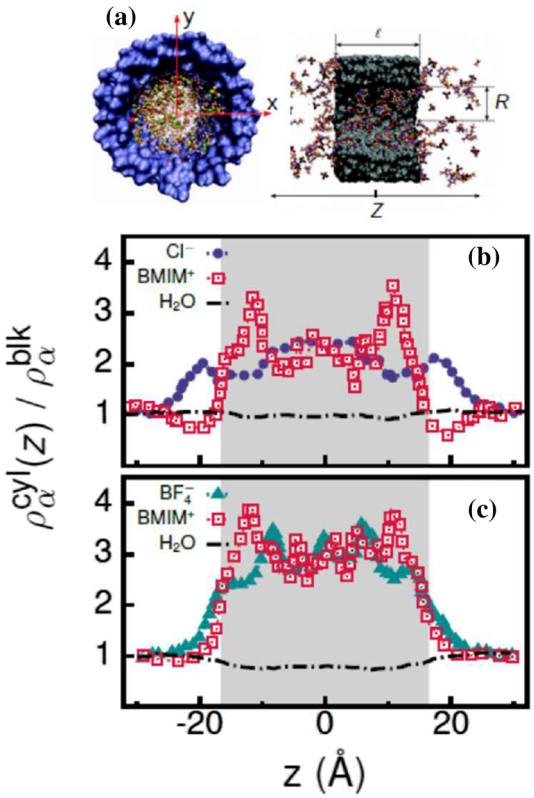

Fig. 16 Normalized density fields along the z-axis for aqueous solutions of **b** $[BMIM]^+[Cl]^-$ with $C_{IL1}^{blk} = 0.87$ M and **c** $[BMIM]^+[BF_4]^-$ with $C_{IL2}^{blk} = 0.78$ M, obtained from a restricted sampling along a central cylindrical volume of radius R. The vertical shading region denotes the pore location. Typical snapshots from different views of the model system, comprising the central pore and lateral bulk reservoirs are shown on top (**a**). For clarity purposes, water molecules have been removed. Adapted with permission from Ref. [174]. Copyright 2012 American Chemical Society

7.1 Equilibrium solvation structures

The density fields of the ionic aqueous solutions of BMIM Cl and BMIM BF_4 along the axial direction of the silica hydrophobic cavity are displayed in Fig. 16. The profiles revealed a 10–20% reduction of the water content inside the pore compared to bulk results, whereas a clear enhancement of salt concentrations was observed, more marked in the case of BMIM BF_4. We remark that these features contrast sharply with the ones observed for confined aqueous solutions of NaCl, where the global salt concentrations within hydrophobic pores were found to be smaller than the values observed in the bulk [387].

Results for the density distributions along the radial direction are displayed in Fig. 17 for the different species. In line with what we have found in the results for the density distributions along the axial direction, for both RTILs the most prominent fluctuations are those observed for the cationic $[BMIM]^+$ species, which remain tightly adsorbed to the wall of the hydrophobic pores. At shorter radii, the profiles exhibit an inner region practically deprived of $[BMIM]^+$ cations, whereas at the central region, the local concentrations attain practically bulk values. Regarding the density distribution of anionic moieties, distinctive features are observed: while Cl^- exhibits adjacent segregated states from $[BMIM]^+$ cations, the more hydrophobic $[BF_4]^-$ anions are compatible with partially overlapped-wall solvation structures. These structural differences might be relevant to the mechanisms that control molecular mobilities, leading to modifications in the transport properties of the confined liquids.

The analysis of the orientational correlations showed than in both RTILs, wall-solvation states are characterized by cations with their ring planes parallel to the solid interface.

Singh et al. investigated the ionic liquid BMIM PF_6 confined within multiwalled carbon nanotubes (MWCNTs) of size in the range 2–3 nm, by means of molecular dynamics simulations [388]. In agreement with previous works, they have also found significant layering in the mass density profiles of the cations and anions in the radial direction; with the cations close to the pore walls having their imidazolium ring parallel to the surface. Regions of high and low density were observed in both the radial and the axial directions upon reduction in the pore loading.

In summary, the structural features of RTILs and aqueous solutions confined within pores of nanometric dimensions analyzed in this section suggest that

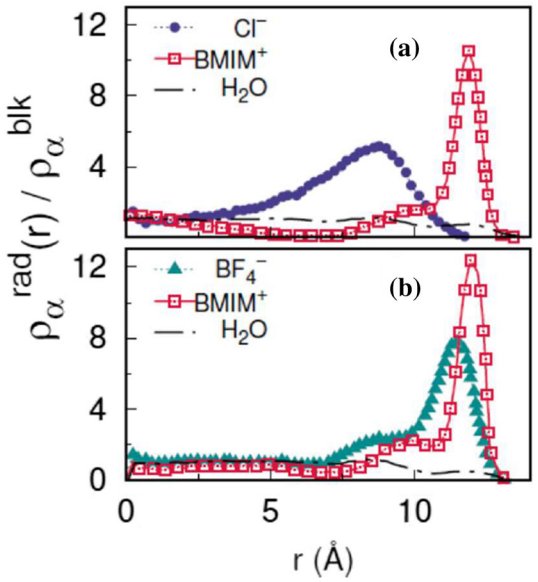

Fig. 17 Normalized radial density fields for different species of confined RTILs within hydrophobic pores of radius $R = 12.5$ Å. Adapted with permission from Ref. [371]. Copyright 2012 American Chemical society

the presence of a hydrophobic, solid-like interface promotes enhancements of the local densities of bulky ionic groups at its close vicinity. More specifically, the results revealed a preferential wall adsorption of $[BMIM]^+$ cationic groups and a somewhat more attenuated propensity for $[BF_4]^-$ anionic species. To preserve electroneutrality, the excess of the positive charge at the interface goes hand in hand with local increments of the concentrations of the corresponding counterions. As a result, these modifications lead to overall concentrations of the ionic species that are between 2 and 3 times larger than the ones in bulk regions.

7.2 Dynamical analysis: transport properties

7.2.1 Diffusion

The dynamical analysis is often performed in terms of the computation of self-diffusion coefficients, via the mean-square displacements and the Einstein classical equation. Figure 18 shows typical features of the mean square displacements of the different species in aqueous RTIL confined solutions. In the case of the simple NaCl electrolyte aqueous solution confined within hydrophobic silica pores of dimensions ~ 2–3 nm, the diffusion coefficients of the ionic species exhibited a 10% drop compared to bulk values, whereas within hydrophilic pores—in which unsaturated O-sites at the silica walls were transformed into polar Si–OH groups—a 50% reduction was observed [411]. In the case of RTIL aqueous solutions confined within hydrophobic silica pores, a drop of similar magnitude in the diffusion coefficients of water and $[Cl]^-$ was observed [371].

Modifications in the transport of bulkier and more hydrophobic ions are much more dramatic: upon confinement, the diffusion coefficient of $[BF_4]^-$ drops a factor of ~ 7–8, whereas the ones for $[BMIM]^+$ get reduced by up to a factor of ~ 20. We remark that these modifications in the transport correlate reasonably well with the magnitude of the structural modifications operated in the local density fields described in the previous section. More interestingly, these effects seem to be also controlled, to some extent, by the presence of nearby bulkier anions which—as in the case of heavier $[BF_4]^-$ groups—may reinforce the retardation effects imposed by the presence of a nearby static, solid interface.

The analysis of diffusion of a pure RTIL, such as the aprotic 1-methyl-3-hexylimidazolium bis-(trifluoromethanesulfonyl)imide (C_6C_1ImTFSI), revealed an overall retardation in the average diffusive motions of cations and anions in both hydrophobic and hydrophilic silica pores, compared to their mobility in the bulk phase [386]. In going from a fully filled pore to the lowest simulated loading in hydrophilic systems, the diffusion coefficients exhibited a reduction of one order of magnitude. In contrast, in hydrophobic pores, the silanization of the silica walls significantly reduced the magnitude of the retardations, and the diffusion coefficients were roughly independent of the filling fraction, resulting close to the bulk value. From a local perspective, the diffusion exhibited a sharp drop of one order of magnitude near the pore walls in hydrophilic cavities, compared to that at the center of the pore, because of hydrogen bonding between the IL and the interfacial SiOH groups, whereas in hydrophobic cavities this effect was less marked because of weaker liquid/wall surface interactions.

Ori and collaborators have investigated the properties of 1-butyl-3-methylimidazolium bis (trifluoromethylsulfonyl)imide RTIL confined within a different geometry by MD simulations [389,390]. They modeled a porous chalcogenide by assembling two GeS_2 flat surfaces separated by a distance H. Hydrogenated GeS_2 surfaces have also been examined. Their findings share many features with those confined in more conventional matrices (silica, carbon, etc.): such similarities are likely to be inherent to confinement and surface interaction effects. Owing to their different roughness and charge surface properties with respect to silica, GeS_2 surfaces affect the properties of the confined IL to a lesser extent. Likewise, they observed that the hydrogenation of the GeS_2 surface affects both the structural and dynamical properties of the confined RTIL, due to the stronger interaction of the IL anion with the hydrogen atoms of chalcogenide surfaces.

The diffusion coefficients computed by Singh et al. for the BMIM PF_6 ionic liquid inside MWCNTs were much smaller than in the bulk phase; being the cations relatively faster than the anions [388]. In a very recent work, Lahrar et al. investigated the structure and dynamics of BMIM PF_6 confined within complex porous carbons, by classical MD simulations [391]. They performed a systematic study of the effects of ion and pore size variations on liquid properties. They found larger dif-

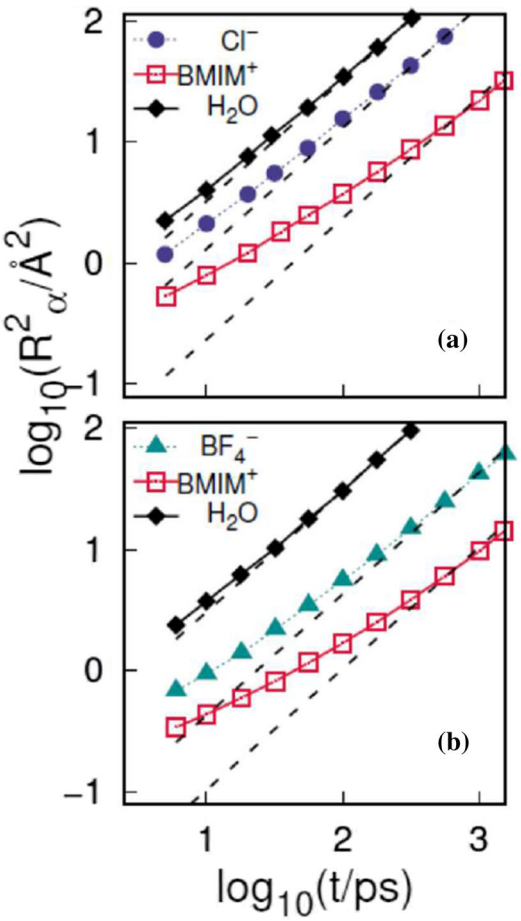

Fig. 18 Mean square displacements, R^2, for different species of confined RTILs solutions within pores of radius $R = 12.5$ Å. Individual diffusion coefficients were computed from the limiting slopes of the mean square displacement (MSD), i.e., $D = \lim_{t\to\infty}(R^2(t)/2t)$ The dashed lines correspond to asymptotic linear plots, with slope one. The MSDs of the confined ions remain in the sublinear temporal regime over time spans unusually long for standard liquid phases. Given the characteristics of the wall-solvation states already described, the sublinear temporal regime might reflect the presence of mechanisms akin to highly correlated "single-file-diffusion" motions, in which surpassing episodes between different particles are severely hindered. Adapted with permission from Ref. [371]. Copyright 2012 American Chemical Society

fusion coefficients with larger anion size and, surprisingly, with the quantity of adsorbed ions. Both findings were interpreted by the authors in terms of confinement, suggesting that when the in-pore population increases, additional ions are located in less-confined sites and diffuse faster. Simulations in which the pores were enlarged while keeping the topology constant supported the above observations.

7.2.2 Ionic conductivity

Within the Green–Kubo linear response formulation [392], ionic conductivities, σ, can be calculated in terms of the time correlation function of the microscopic charge current. Equivalently, that relation can be transformed—via parts integration and invoking time symmetry—into the Einstein–Helfand relation [393–396], obtaining a generalized mean square charge displacement correlation function. This function contains a collective quantity that includes not only single-particle contributions (σ^{NE}, the so-called Nernst–Einstein component) but also distinct contributions: $\sigma = \sigma^{NE}(1 + \Delta)$. As such, its calculation is likely to be subjected to larger errors compared to the case of single-particle properties. Usually, Δ is a negative quantity; in other words, the incorporation of correlations between different particles leads to an overall reduction in the electrical conductivity. While this feature holds for pure RTILs [391,396–398] and for aqueous solutions as well, the simulation results revealed that this characteristic is not satisfied in confined solutions [371].

In the case of the aqueous solutions of RTILs, whereas the confinement leads to a lower conductivity than in the bulk for BMIM BF_4, a greater conductivity was found for BMIM Cl. This was unexpected and the physical interpretation of these changes is not always straightforward. We remark that such positive deviations have also been reported in molten salts comprising noble metal halides [399–402]. In principle, a delicate balance between the increment in the number of charge carriers within the pores and the observed mobility retardations could be invoked. Still, the simple consideration of the differences in the spatial correlations of the different species within the pore may provide some clues. However, a more detailed analysis of the contributions to Δ must be considered. Indeed, as a collective quantity, it contains cross-dynamical correlations between distinct molecules, which could be determined by the characteristics of the different ionic densities within the pores As a plausible argument to account for the conductivity increment, it is likely that the segregation of $[Cl]^-$ and $[BMIM]^+$ groups in adjacent, concentrical shells with boundaries perpendicular to the z-direction could reinforce cooperative effects between the equally charged ions.

In contrast, in BMIM BF_4 solutions, the spatial overlap between the cation/anion radial density distributions would indicate a larger extent of cancellations, leading to a smaller value of Δ. Incidentally, similar connections between segregation and transport within nanocavities have been established in a computational study of cross fluxes of mixtures of protic–aprotic solvents [403].

Ori et al. [390], computed the ionic conductivity of the RTIL confined in amorphous porous chalcogenides; they found that the conductivity remains close to its bulk counterpart and is almost insensitive to pore size and surface chemistry. Oppositely, the ionic conductivity measured in cylindrical silica hydrophilic pores resulted $\sim$ 50 % lower than in the bulk phase—

and dropped down to 50 times smaller than bulk at the smallest loading–, whereas within the functionalized hydrophobic pores, the conductivity resulted 30% larger than in hydrophilic cavities and showed weak dependence on loading [386]. These features, namely, a strong dependence of the conductivity on the pore filling fraction in hydrophilic cavities and a much weaker dependence in functionalized pores have been also observed in the experimental study of Garaga et al. [404].

To conclude, we remark that the localization of a sizable fraction of the ionic species at interfacial regions within the pore brings down the diffusion coefficients of the trapped species by a factor of ≈ 0.5 for the fastest Cl^- ions. For bulkier groups such as $[BMIM]^+$ and $[BF_4]^-$, the drop may go down by practically 2 orders of magnitude. A detailed interpretation of the changes observed in the electrical conductivity in terms of microscopic features is not straightforward, because, as a collective property, it involves the interplay of cross correlations between like and unlike species involving bulk-like and surface-adsorbed molecules of well-differentiated dynamics.

In summary, the examples and systems reviewed in this article shed light on the structural and dynamical features of ionic liquids and aqueous solutions confined within pores of nanometric dimensions. The density fields associated to the ionic species revealed a preferential wall adsorption of these groups, leading to increments of the ionic liquid concentrations within the pores that are between 2–3 times the bulk ones. These modifications resulted more marked in solutions containing more hydrophobic anionic species.

Concerning transport properties, the segregation of the ionic species toward the pore wall promotes a sharp drop in the individual ionic diffusion coefficients. Non-uniform trends in the variations of the electrical conductivity were found; this phenomenon seems to be a result of a complex interplay of, at least, three main competing effects: (i) the retardations of the diffusive motions; (ii) the variations in the concentrations of charge carriers within the pore; and (iii) cross-dynamical correlations, which would be largely determined by the characteristics of the detailed local densities.

8 Hydrophobicity, nanoconfinement and the context-dependent nature of molecular interactions

Biological organization processes, as well as many self-assembly processes in material science, imply the association of complex surfaces that attract each other by means of non-covalent interactions taking place within an aqueous nanoconfined environment. This is the case, for instance, of the drying transition that triggers the hydrophobic collapse in protein folding. Descriptions borrowed from the bulk could prove themselves misleading for this intrinsically nanoscale scenario, since the particular nanoconfinement conditions might affect the local hydrophobicity and modulate (possibly non-additively) the non-covalent interactions. The study of simple model systems is thus relevant not only to try to isolate the different ingredients at work within this complex picture but also to rationalize their possible mutual interplay under controllable settings. Thus, beyond their inherently basic interest, investigations on these lines would help to identify generalizable principles toward a picture of nanoconfined water and a theory of hydrophobicity at the nanoscale, while simultaneously aiming at detecting design elements of general validity for rational design in applied fields of great relevance.

Within this context, we shall hereby review the relationship between local hydrophobicity and non-covalent interactions in a couple of simple illustrative situations. We shall first focus on the self-assembly of graphene and graphene-based materials to show that, while usually regarded as hydrophobic, these systems in fact exhibit a rather hydrophilic behavior due to their dense atomic network that adds up the effect of several weak carbon-water van der Waals interactions [405,406]. This example illustrates the fact that the notions of "apolar" and "hydrophobic" should not be necessarily taken as synonyms. Then, we shall study how the local hydrophobicity affects electrostatic interactions operating under nanoconfined water environments, a situation of relevance, for instance, for certain protein–protein association processes. We shall focus on pairs of parallel flat surfaces with attractive electrostatic interactions by employing model systems functionalized with different charged, hydrophobic, and hydrophilic groups [407]. Such studies demonstrate that, by increasing the local dehydration propensity, a hydrophobic local environment is able to strengthen the electrostatic attraction in a non-additive way, thus fostering the self-assembly process.

8.1 Hydrophilic behavior of graphene and graphene-based materials

The comprehension of the behavior of water at interfaces and under nanoconfinement is central for a wide range of scientific fields, particularly for biological systems like proteins and lipids membranes [408–414]. Under such conditions, water is known to usually display a behavior quite different from the bulk. For example, it presents a subdiffusive behavior at short times even at room temperature, a slow dynamics reminiscent of glassy systems [412,415–426]. In particular, the hydrophobic effect is central for protein folding and binding and also plays a major role in contexts of materials self-assembly within aqueous environments. The hydrophobic collapse initiates when a pair of formerly hydrated surfaces undergo a dehydration process upon approaching each other. Indeed, below a critical separation water might become thermodynamically unstable, thus inducing a drying or de-wetting transition that promotes the self-assembly process [408–411]. In

fact, a current successful paradigm of protein binding [427–436] implies that ligand association involves the replacement of easily removable (labile) hydration water from the binding region. Binding sites, thus, exhibit an enhanced dehydration propensity (high local hydrophobicity) that favors drying upon ligand binding.

It is usual to speak of hydrophobic and apolar as synonyms, but a word of caution is in order on this matter. For instance, apolar systems like graphene and graphene-based structures like graphite, carbon nanotubes and fullerenes are usually regarded as paradigms of hydrophobic materials while they are actually far from being so [405,406,437–442]. It is well known that water penetrates carbon nanotubes of very small radius [420,442] (much smaller than the thinnest tunnel that gets filled in certain model hydrophobic materials [420]). Inside such carbon nanotubes, the water molecules loss significant hydrogen bond coordination. It is evident that the water-wall attractions should provide certain compensation. But the carbon-oxygen van der Waals interactions are weak. This conundrum is solved when we consider that graphitic-like structures have a high density of carbon atoms and, thus, a water molecule interacts simultaneously with several carbon atoms. Thus, even when the constituent atoms are apolar, a local high-density context is able to drastically reduce the local hydrophobicity. In fact, further artificial weakening of the Lennard–Jones interactions between C and O in molecular dynamics simulations make thin carbon nanotubes to desorb [420,442]. Such a hydrophilic behavior of graphene has also been recently corroborated experimentally [437]. Specifically, water contact angle measurements over clean graphene-based surfaces yielded a rather hydrophilic value, indicating that the hydrophobic-like data reported in previous studies would in fact result from contamination by hydrocarbon adsorption from the air [437]. The self-assembly properties of graphene sheets have also been compared with that of pairs of alkane-like self-assembled monolayers (SAM, employed as a control) by means of potential of mean force calculations [407]. Even when the final equilibrium state is indeed the collapse of the sheets, molecular dynamics studies demonstrated that parallel graphene sheets present a strong tendency to remain fully hydrated for moderately long times and, thus, they are less prone to self-assembly than the SAM surfaces which readily undergo a hydrophobic collapse [407]. In turn, potential of mean force calculations indeed made evident that the solvent exerts a repulsive contribution on the self-assembly of graphene surfaces, as can be learnt from Fig. 19a [407]. This result makes evident the attraction of hydration water by the graphene surfaces, being thus difficult to remove and implying a manifest hydrophilic behavior.

To make this observation more quantitative, one should employ a hydrophobicity measure. Among the parameters that have been employed to quantify local hydrophobicity, a useful approach has been the study of local water density fluctuations. In fact, water abhors vacuum thus promoting hydration of both polar and apolar surfaces, and displaying typical density profiles with layered structure. However, it has been shown that water density fluctuations are significantly enhanced at hydrophobic surfaces. Thus, hydrophobic systems present a higher vacating probability and thus a lower free energy of cavity creation at small volume [443,444].

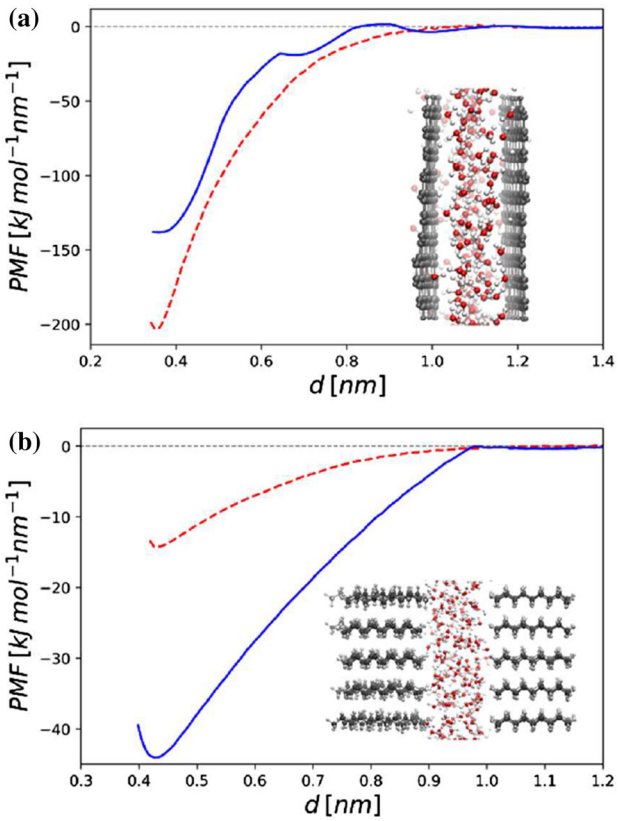

Fig. 19 Potential of mean force (PMF) as a function of the separation between **a** two graphene sheets and **b** two self-assembled monolayers. In both figures, full lines correspond to the PMF calculated in TIP3P water while dashed lines correspond to the PMF obtained in vacuum

This kind of study has thus been employed on graphene surfaces [406,407]. Figure 20 displays the probability distributions for observing N water molecules within a small observation sphere of radius 3.3 Angstroms (similar to the volume of a methane molecule) placed over different surfaces: a hydrophilic SAM (functionalized with OH), a hydrophobic SAM (functionalized with CH_3), a graphene sheet and a graphene sheet where the C–O interactions (graphene–water interactions) have been weakened roughly to one half of their value in the simulations. We can observe that the graphene sheet displays a hydrophilic behavior since its water vacating probability (P(N=0)) is very low, comparable to that of the hydrophilic SAM. By lowering the water–graphene LJ attraction interactions, the graphene surface is made more hydrophobic, thus making evident the relevance of the mildly attractive water–carbon interactions.

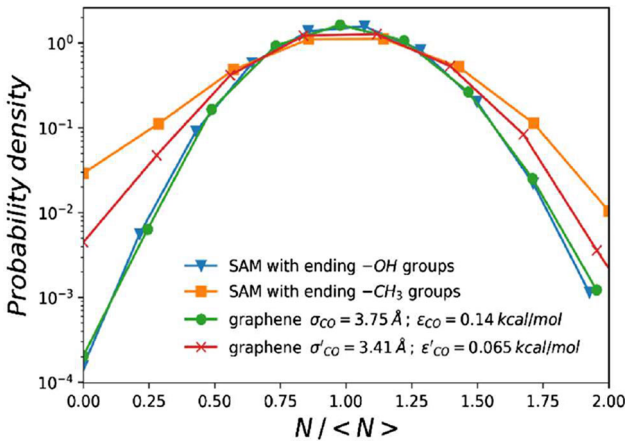

Fig. 20 Probability distributions for observing N water molecules within a small spherical observation volume of radius 3.3 A (similar to a methane molecule) tangent to the different surfaces studied

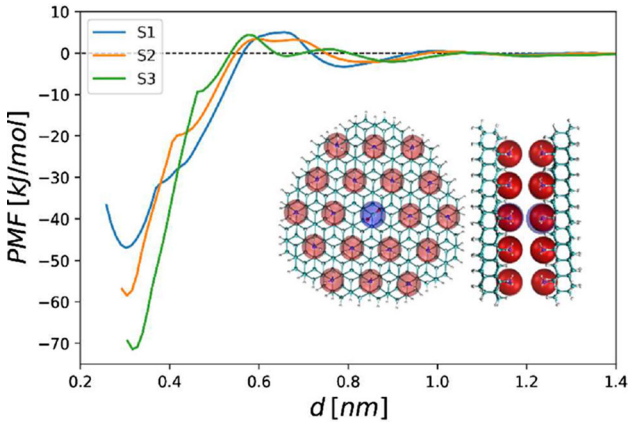

Fig. 21 Potential of mean force in water (TIP3P) for the different simulated systems with charged group in the center of each surface (NH_3^+ in one of them and CO_2^- in the other), as a function of the plate distance (the distances are measured between the positions of the charged groups of both plates): S1 for parallel surfaces with polar groups ($-NH_2$) environment; S2 for parallel surfaces, one with apolar groups ($-CH_3$) environment and the other with polar groups ($-NH_2$) environment and S3 for parallel surfaces with apolar groups ($-CH_3$) environment

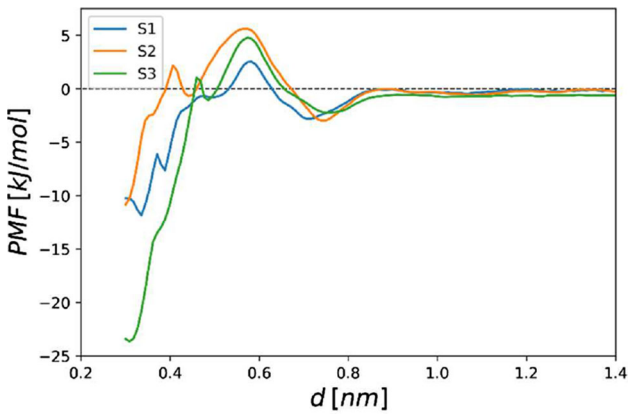

Fig. 22 Arithmetic difference between the PMFs obtained for the charged and neutral systems in TIP3P water: S1 for parallel surfaces with polar groups ($-NH_2$) environment; S2 for parallel surfaces, one with apolar groups ($-CH_3$) environment and the other one with polar groups ($-NH_2$) environment and S3 for parallel surfaces with apolar groups ($-CH_3$) environment

Hence, again we find that it is not the strength of the C–O interaction that rules the local hydrophobicity but the local context (carbon network) within which the hydration takes place. Since the carbon density on the graphene sheet is high, a hydrating water molecule interacts simultaneously with many C atoms being thus difficult to remove. As already indicated, the degree of hydrophobicity of a surface is not only dependent on the polarity of its constituent units.

8.2 Electrostatic interactions within aqueous nanoconfined environments

To evidence the role of the local nanoconfined environment in modulating electrostatic interactions, simple model systems were studied. The self-assembly of pairs of diamond-like carbon structures with functionalized faces were built. This implied the inclusion of a functional group of given polarity (NH_2, polar, or CH_3, apolar) on each surface site, which we shall call from now on as "environment," and a charged group in the center of each surface (NH_3^+ in one of them and CO_2^- in the other).

In Fig. 21 [407] we show the potential of mean force (PMF) for the cases when both parallel surfaces include polar groups, when one of them has apolar groups and the other one has polar groups, and a third case when both of them have apolar groups. Since the PMF in vacuum are extremely similar for all cases, the differences in the attraction of the two surfaces are mostly due to the effect of water [407]. From Fig. 21 we can learn that as the degree of hydrophobicity of the environment is increased (from hydrophilic to hydrophobic), the self-assembly energy grows, thus making evident the fact that the local hydrophobicity enhances the attraction.

In turn, in Fig. 22 [407] we subtract from the PMF curves of Fig. 21, the PMF curves of the corresponding non-charged relatives (when the central charged functional groups are replaced by a group of the corresponding non-charged environment). The large differences displayed by such Figure make evident the significant modulation that a hydrophobic environment exerts on the electrostatic interactions.

In turn, a study of the local distribution of water molecules for the above-mentioned charged plates at short plate separation [407], has shown that a hydrophobic environment triggers the dehydration of the charged central group thus favoring the self-assembly process. On the contrary, a hydrophilic environment promotes a tight local hydration around the charged central group.

Finally, it is interesting to note the effect of positional differences in identical composition systems. A study of a system of parallel (electrostatically attractive) plates each with a charged group within a hydrophobic environment shows that as the charged groups are moved from the center toward the border of the plates, the PMF becomes less attractive since the charges are being increasingly exposed to the solvent and, thus, their local environment gets less hydrophobic [407].

Taken together, the previous results show that increase in the local hydrophobic properties of a surface exacerbates, in a non-additive manner, charge interactions that occur within nanoconfinement. When the local dehydration propensity increases, the electrostatic interaction strengthens and the drying process is facilitated, thus promoting the self-assembly process. This means that a proper combination of charged groups and a local hydrophobic environment could provide a useful expedient for binding strategies, as, for example, in shaping protein binding sites.

In summary, the examples described in this section show that a simple extrapolations of concepts derived in bulk contexts might be misleading when trying to rationalize nanoconfined situations wherein the mutual interplay between local hydrophobicity and non-covalent interactions is usually not trivial. This fact is not only relevant from a basic perspective but might also be crucial in applied contexts where a rational design is demanded.

9 Theoretical insights into polymer-coated nanopores in aqueous solution

Nanopores widely exist in biological systems as they connect functional compartments that culture different biomolecule profiles and physiochemical environments. From aquaporin [445], ion channels [446], to the nuclear pore complex (NPC) [447], nanopores regulate many biological functions such as the conduction of water, the generation of action potentials, and the storage of genetic material. Biological nanopores are made of proteins that can stabilize a void structure of membranes and undergo structural changes in response to a wide assortment of stimuli. Although the densities of biological nanopores are highly variable across different cell types and regulated by biological signals, their dimensions and shapes are of good consistency to fulfill their functions as selective transporters. Many diseases such as neurological disorder and cancer are associated with nanopore dysfunction and mutation of related genes [448]. Through these functional gates in biology, we can gain a deeper understanding of life and pathological processes.

While biological nanopores are still under intensive study, man-made nanopores and porous materials have emerged as promising solutions to challenging problems such as water purification [449–451], biosensing [452–457], nanofluidic logic gating [458–460], and energy conversion [461–464]. Advanced fabrication and etching techniques have been developed to address the size and shape control of artificial nanochannels [465–467]. Surface modification of solid-state nanopores with coating materials such as polyelectrolytes [469–472], polypeptides [473–475], oligonucleotides [476–478], and lipid layers [479,480] has further realized the separation of pore synthesis and its functionalization, which allows for more design freedom for specific applications [481]. Nevertheless, this vast repository of coating materials also poses new challenges to the design of artificial nanopores, as the traditional bottom-up design from the synthesis variable to the targeted function via experimental trial-and-error will be impractically slow and expensive. Facing such challenge, engineers have turned to biological systems to seek inspiration. Many biomimetic nanopores with advanced functions have been developed during the last two decades [482–484]. For example, inspiration from biological ion channels has led to the development of crown ether embedded [485] or attached [486] nanopores that selectively transport monovalent ions. Solid-state nanochannel with pH responsive polyelectrolytes at its two ends has been built as an artificial analogue to biological ion pumps [487]. Inspired by glucose-sensitive channels, artificial chiral gating has been realized by introducing host–guest systems that can recognize the chirality of glucose [488]. With superior mechanical and thermal stability than their biotic analogues, these biomimetic nanopores can work at unphysiological conditions to meet the demand of broad applications.

Besides learning from nature on nanopore design strategies, it is also useful to understand the fundamental physics and chemistry of aqueous solutions under nanoconfinement for optimization principles. Knowledge of molecular and ionic transport at the nanoscale is not only of vital importance in life and physical sciences, but it also holds the key to the development of artificial nanopores beyond mimicking nature. When the confinement reaches nanoscale, which is typical in nanopores and nanofluidic systems, the behavior of liquids can be exotic as they start to deviate from that in bulk solution. For instance, the boundary condition can have strong impacts on the diffusion of solvent molecules and the friction of their flow [489–493]. The hydrogen bond network of water is disturbed under extreme confinement such as inside carbon nanotubes, which can lead to fast transport [494,495]. For charged molecules confined by a nanopore, electrostatic interactions are very strong when the size of the pore is narrowed down to the Debye length. A surface-charged nanopore with radius comparable to the Debye length can result in a "unipolar solution," which is dominated by ions that carry the opposite charge to that of the pore surface [324,496]. When the nanopore is coated by macromolecules or polymers of similar size to the pore dimension, the coating molecules will experience strong curvature effect as their conformational freedom is topologically constrained by the concave surface [497,498]. Solvent effect is yet another factor that adds to the complexity of the coating morphology

inside nanopores. Within the confined geometry, changing the quality of solvent can give rise to richer phase behaviors of polymers than those in unconfined conditions [499–501]. For example, coating polymers grafted to the inner surface of a nanopore in poor solvents can either collapse to the center or the wall of pore dependent on the ratio between the polymer length and the pore radius. Apart from these physical arguments, nanoconfinement could also create local environment with apparent equilibrium constants of chemical reactions that are shifted from the bulk values [469,499]. These reactions include chemical-base equilibrium, redox reaction, ligand–acceptor binding, and so on. It is worth noting that chemical equilibria are often strongly coupled to physical interactions at the high crowding level inside polymer-coated nanopores, giving rise to unique molecular behaviors that can regulate the gating response to external stimuli.

The gating properties of polymer-coated nanopores as well as the underlying molecular mechanisms have attracted extensive theoretical research efforts. From scaling arguments [502–504] to mean field theories [499,500,505–512] to computational simulations [501, 513–515], different modeling methods have offered rich insights into this growing field. In this paper, we briefly review the modeling works in recent years, with a focus on those based on a molecular theory methodology. The molecular theory is a theoretical framework developed in our group over the last two decades, which has been widely used to study confined and end-tethered polymers in a broad spectrum of solvent conditions and surface curvatures [498,499,516–519]. By inputting a large set of molecular conformations of the coating polymers generated from self-avoiding rotational isomeric state model [520], Monte Carlo (MC), or molecular dynamics (MD) simulations, the theory explicitly considers the coupling between molecular organization, physical interactions, and chemical equilibria. As a density functional theory, it readily outputs the free energy and other thermodynamic properties of the system, which could be non-trivial to obtain from MD simulations. Unlike conventional mean field methods, molecular theory accounts for more molecular details of the confined polymers and is comfortable of handling heteropolymers with complex sequences of distinct monomers. Herein, we review theoretical insights on the effects of solvent, charge, and polymer sequence on the gating behaviors of coating polymers in both artificial and biological nanopores. We discuss the interplay between these effects in confined geometry and how to use the theoretical understanding to optimize nanopore-controlled transport.

9.1 Structural phases and chemical equilibria of homopolymers in nanopores

Homopolymers comprised of identical monomers are the most common polymeric materials for nanopore functionalization. Homopolymers with end-to-end length on the same order of magnitude with or larger than the characteristic lengths of the nanopore (i.e., the pore diameter and length) are expected to be strong gating agencies of the system. Note that nanopores whose lengths are larger than their diameters are often called nanochannels, but in this paper we will stick to the term “nanopore” for simplicity. The morphology of homopolymer has been theoretically shown to be sensitive to its grafting position of the pore [500]. Changing the grafting point from the middle of inner pore surface to the pore exits and further to the outer surface of the pore can change the orientation and spatial distribution of the free end of the polymer. Scaling arguments have depicted qualitative phase diagrams for neutral homopolymers grafted to the inner surface of nanopore, as a function of the pore width and the grafting density of the polymers [502]. Such analyses have been applied to both the good and poor solvent conditions, which leads to the prediction that under certain coating conditions the nanopore can be switched between open and closed states by changing the solvent quality [504]. Guided by these predictions, MD simulations have been carried out to demonstrate that morphology switching process of neutral homopolymer can be triggered by co-nonsolvent [504].

Morphological change of end-tethered polyelectrolytes is often associated with ionic gating, which can be controlled by pH or multivalent bridging ions of opposite charges [499,509]. However, it should be stressed that the acid–base equilibrium of weak polyelectrolytes, when immobilized to surfaces, can behave very differently from those of mobile ones in bulk solution [518]. This phenomenon has been studied by different theoretical methods including scaling theory [521,522], self-consistent field approaches [523,524], MC simulation [525], and systematically investigated by molecular theory for different surface curvatures [499,517,518,526]. The shift of acid–base equilibrium can be even more significant, when the end-tethered polyelectrolytes are confined in nanopores. Moreover, such shift of chemical reactions is not uniform within the nanopore but dependent on the location of the chemicals. Therefore, the reactions can be thought to have varying local reaction constants throughout the confined space. Nanopores coated with polyelectrolytes can serve as ionic gates whose conductivity can be turned on and off by the proton concentration in surrounding environment. One example is a long nanopore coated by poly(4-vinyl pyridine) (P4VP) brushes as schematically shown in Fig. 23A, which has been constructed by Yameen et al. in experiment [469]. Molecular theory study [499] shows that the acid–base equilibrium of P4VP is shifted with the apparent pKa being 3.7, which is significantly lower than the bulk value of 5.2. As shown in Fig. 23B, this shifted reaction equilibrium is predicted to cause a different pH dependence of conductivity than that is expected based on the bulk pKa value. The theoretical prediction from molecular theory is in good agreement with the experimental observation of pH dependent conductivity [499].

The ideal solution approximation of chemical reactions in general does not apply in nanopores. Besides

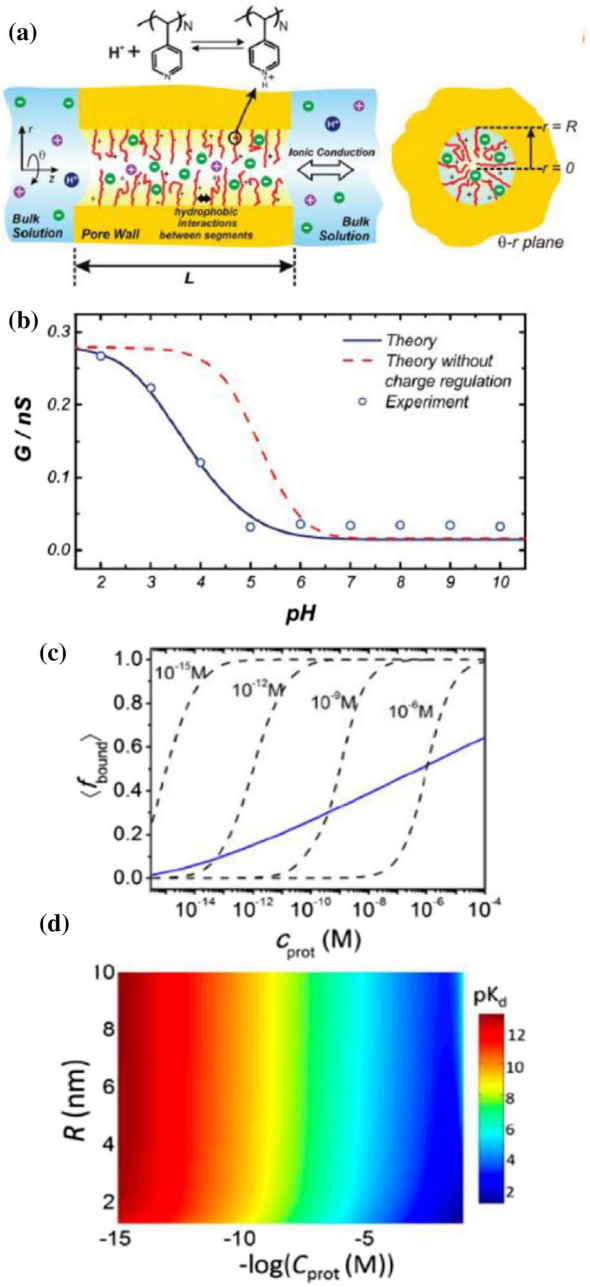

Fig. 23 Shifted equilibria of chemical reactions in polymer-coated nanopores. **a** Schematic representation of the polyelectrolyte brush modified long nanopore. The inner surface of the pore is modified with end-tethered chains of poly(4-vinyl pyridine). **b** Comparison between experiment and molecular theory on the pH-dependent conductivity. Reprinted with permission from Ref. [499]. **c** Molecular theory prediction of average fraction of bound ligands inside a nanopore as a function of the molar concentration of the proteins in bulk solution (solid blue line), in comparison with the predictions of the Langmuir isotherm for different values of the dissociation constant (black dashed lines). **d** Apparent dissociation constant as a function of the pore radius and the molar concentration of the proteins in bulk solution. Reprinted with permission from Ref. [527]. Copyright 2015 American Chemical Society

acid–base equilibrium, another example is ligand–receptor binding under nanoconfinement [527]. In this case, the binding curve has been predicted to span more than 10 orders of magnitude in bulk protein concentration as shown in Fig. 23C. The width of the transition regime is much larger than those that are predicted by the commonly used Langmuir isotherm, regardless of the choice of dissociation constant [527]. This unexpected behavior suggests that the concept of dissociation constant does not necessarily hold in nanoconfined environment as the apparent constant itself would depend on the protein concentration as shown in Fig. 23D. This means a different language is needed to describe the ligand–receptor binding picture inside nanopores. Since proteins bound to the coating ligands can change the ionic conductivity of the nanopore, understanding such nanoconfined binding is useful for the design of nanopore-based biosensors.

9.2 Sequence design of stimuli-responsive copolymers

Nanopores coated with stimuli-responsive layers are promising elements in nanofluidic circuits. For the integration of multiple stimuli responses into a single nanopore, one strategy is to use copolymers made of distinct monomers. This approach is becoming more practical as the copolymer synthesis technology advances. Surface-attached copolymer brushes can be achieved by using either “grafting from” or “grafting to” methods [528]. It is even possible to control the chemical sequence of the target copolymer at the resolution of single monomer [529]. Ananth et al. have recently synthesized artificial unfolded proteins with designed amino-acid sequences and attached them to the surface of a solid-state nanopore [530]. DNA origami scaffold has been developed to further enable position control of protein grafting within nanoconfinement [466,468]. With these fast-growing experimental tools, sequence-designed polymer coating could become a new frontier of artificial nanopores.

Theoretical designs of copolymer-coated nanopores have been attempted in the last decade. Cheng and Cao reported a MD simulation of triblock copolymer with the design of one hydrophilic charged block being flanked by two hydrophobic neutral blocks [501]. Such copolymer design leads to a temperature-responsive gating mechanism, in which the nanopore adapts a collapse-to-the-center morphology at low temperature, and a collapse-to-the-wall morphology at high temperature. The center phase requires the charged polymer block to stretch out against an entropic penalty. This penalty is, however, too large at high temperature for the center phase to be thermodynamically stable.

A molecular theory study [508] of responsive copolymer gate has been done for a short nanopore as schematically illustrated in Fig. 24A. The sequence of the copolymer is shown in Fig. 24B. The copolymer gate is designed to have two blocks with different charge and hydrophobicity. The first block is

neutral and hydrophobic, while the second block contains alternating neutral and ionizable monomers. (One copolymer gate employs only one kind of ionizable monomers, either acidic or basic.) The second block is attached to wall and responsive to the proton concentration of the solution since the hydrophobicity of ionizable monomers is pH-dependent. The competition between hydrophobic attraction and electrostatic repulsion shapes the gating structure of the nanopore. When the hydrophobic attraction dominates, the copolymer will collapse to the wall of the nanopore. With enough electrostatic repulsion, the end-tethered block will stretch out to enable the neutral block to collapse into the pore center. Taking into consideration of the coupling between physical interactions and chemical reactions, molecular theory predicts a phase diagram of the copolymer-coated nanopore (Fig. 24C), which shows that besides pH, salt concentration can also strongly impact the gating of the copolymer. This unexpected result highlights the dual rule of salts in screening the electrostatic interactions and shifting the acid–base equilibrium. The transition between wall and center phases is rather abrupt as shown in Fig. 24D, which could happen in a wide range of pH (marked gray in Fig. 24E) but most likely when the free energy matches between the two states. The ionization fraction of the copolymer can experience a discontinuous change at the transition pH, which can be used for logic gating of ions (Fig. 24F). The above examples of theoretical nanopore design demonstrate the potential of sequence-controlled polymers as multifunctional nanofluidic gates.

9.3 Theoretical understanding of the nuclear pore complex

As the largest biological nanopore and the sole intracellular channel in eukaryotic cells, the nuclear pore complex (NPC) controls the biomass transport in and out of the cell nucleus in a highly selective yet efficient way. The overall architecture of the NPC is a "hairy" pore [531] as schematically depicted in Fig. 25a. Unlike most of the transmembrane protein channels whose gating relies on the conformational change of folded proteins, the NPC uses hundreds of intrinsically disordered proteins (IDPs) as its gatekeeper. These IDPs are called FG-nucleoproteins (FG-Nups) as they contain many hydrophobic phenylalanine–glycine (FG) repeats separated by hydrophilic spacers. More than 10 kinds of FG-Nups form a selective permeability barrier, which transports water, ions, and macromolecular cargoes with nuclear import/export signals (short amino-acid sequences) while blocking unrecognized macromolecules.

Karyopherins (Kaps) that can bind to the FG repeats through hydrophobic interactions serve as transport agents for large cargoes and shuttle between the nucleus and cytoplasm. Given the unfolded and flexible nature of the FG-Nups, the NPC is essentially a copolymer-coated nanopore with the sequences of the copolymers optimized by biological evolution. Therefore, structural knowledge of the NPC is not only of fundamental importance in biology, but also valuable in guiding the rational design of copolymer-coated artificial nanochannels. However, despite the experimental progress in understanding the scaffold structure of the NPC [532,533], the functional structure of the permeability barrier still remains elusive and debated by different hypotheses [534,535]. The small size of the pore, fast dynamics of the FG-Nups, together with the aqueous working environment poses a great challenge for the experimental resolution of the molecular gate. Modeling and simulation efforts are especially crucial to elucidate the gating structure and reconcile conflicting views.

Various theoretical methodologies have been applied to study the yeast NPC, using different levels of coarse-graining to deal with the molecular complexity of the system [506,511,513–515,519,536,537]. In classical mean field treatments, the FG-Nups are modeled as homopolymers with each monomer representing one or several amino acids. The electrostatic, van der Waals, and hydrophobic interactions between amino acids are absorbed into a χ parameter that describes the overall cohesiveness between the coarse-grained monomers. With such simplification, mean field theory provides an efficient tool to investigate the structural behavior of FG-Nups under different in vitro conditions. For example, mean field theory has been applied to describe the phase separation of FG-Nups in solution [492], as well as how Kaps affect the structure of FG-Nup brushes attached to surfaces of varying curvatures [506,539].

MD simulations of the FG-Nups fall into two categories: all-atom and coarse-grained. Considering the size of the NPC, all-atom simulations are so far limited to single or several FG-Nups, often of the same type such as Nsp1. Even with the full atomistic details, results from different simulations are not necessarily consistent with each other due to the differences in the chosen force fields, parameterizations, and the treatment of water. Nevertheless, all-atom simulations have provided rich molecular insights on the conformations of FG-Nups and their binding with the Kaps. Gamini et al. performed all-atom MD simulation with implicit water to predict that FG-Nups form a network of protein bundles [540]. The bundles typically consist of 2–6 proteins and are interlinked by single FG-Nups. On the other hand, all-atom simulations with explicit water suggest that FG-Nups are highly flexible and unstructured, even in the presence of multivalent Kaps [541]. Nevertheless, the physical extension of FG-Nups is found to be sensitive to the choice of force field for the explicit water [542]. Coarse-grained simulations have been conducted to study either a subset of FG-Nups under nanoconfinement or the whole NPC. By comparing to reference systems integrated with mutated FG-Nups, coarse-grained simulations results highlight the importance of charge and sequence effects in the structuring of the permeability barrier [536]. The whole NPC simulation by Ghavami et al. showed that the native FG-Nups assume a donut-like morphology [515], which is consistent with the peripheral passageway of Imp β

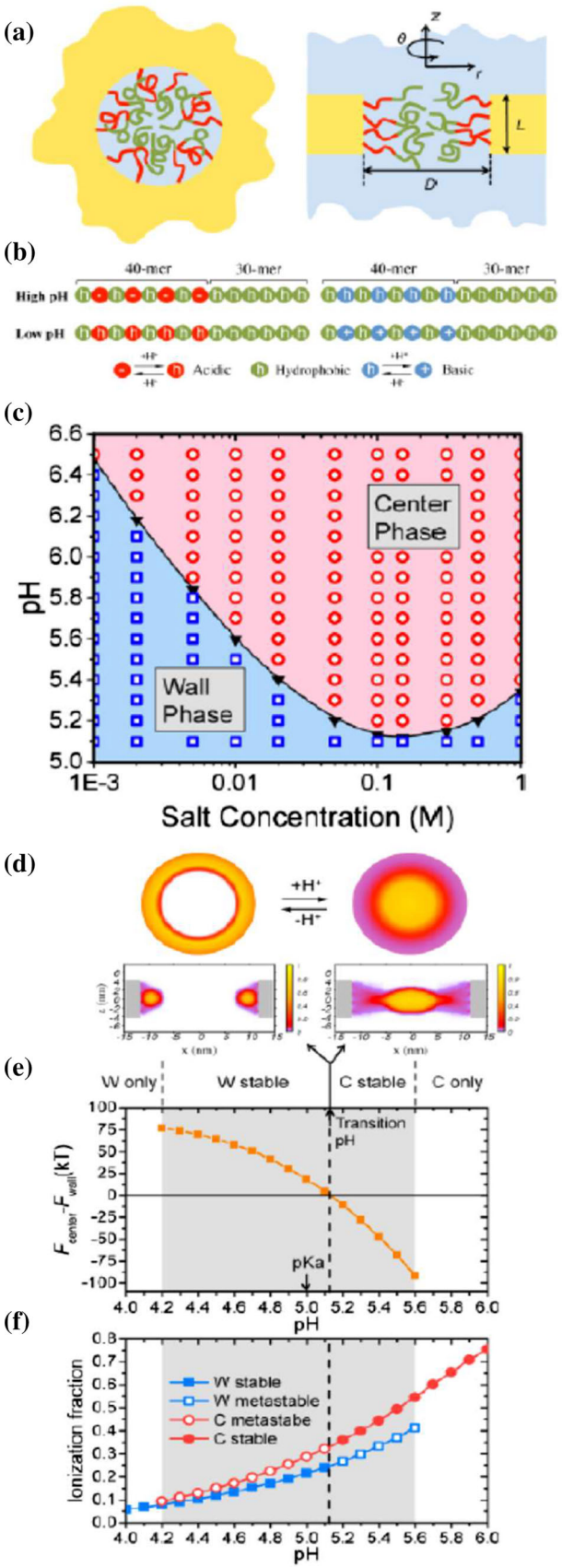

Fig. 24 Design of copolymer for smart (stimuli-responsive) nanopore. **a** Schematic representation of the copolymer grafted short nanopore. **b** Sequence design of the copolymer. The copolymer contains in total 70 monomers, which can be classified into two groups according to their ionizability. The ionizable ones are hydrophilic as they get charged, and hydrophobic when they are neutral. **c** Phase diagram of the nanopore. **d** Switching between center and wall phases at the transition pH. **e** Free-energy difference between the two phases and the metastable regime. **f** Ionization fraction of both phases within the metastable regime. Reprinted with the permission from Ref. [508]. Copyright 2017 American Chemical Society

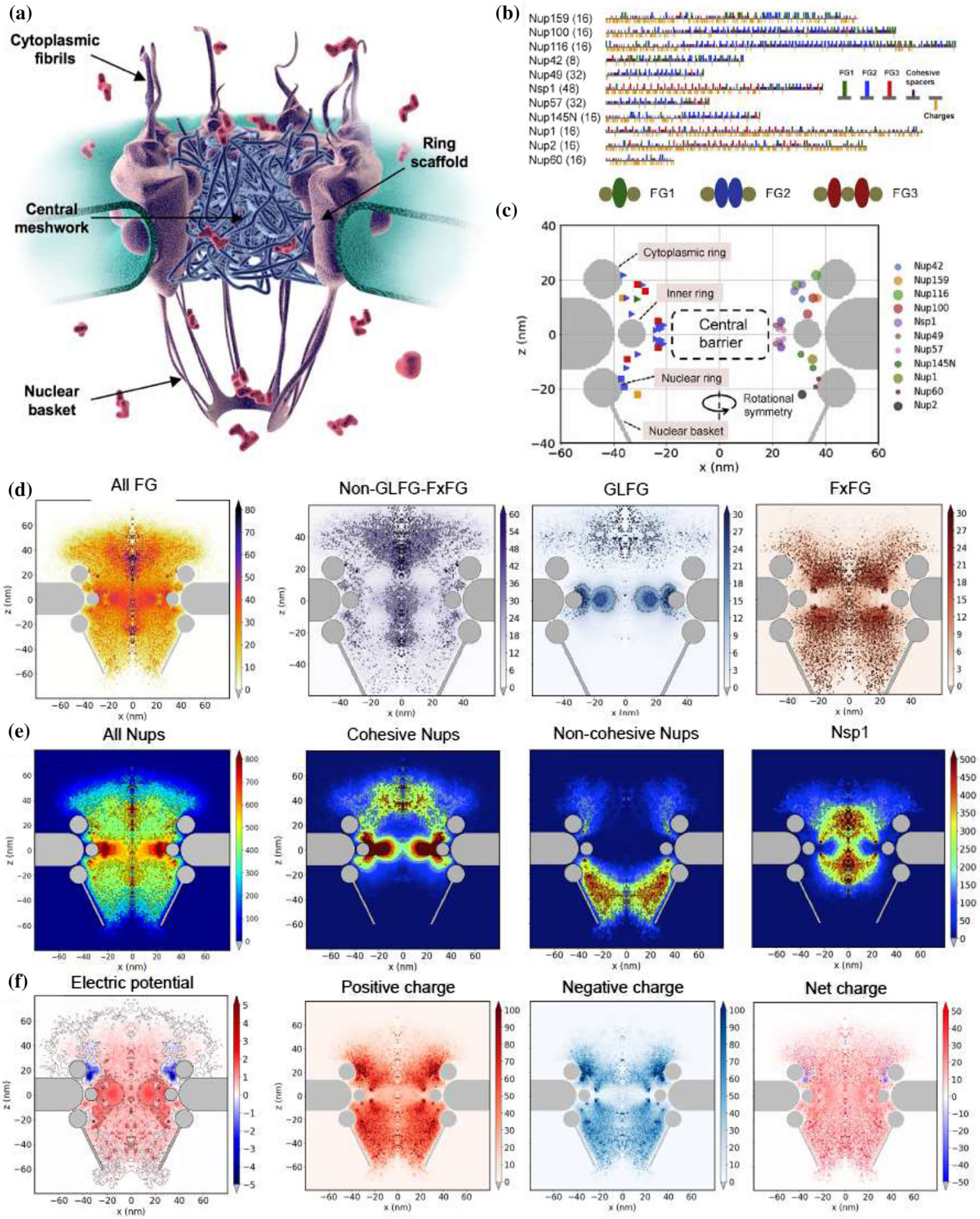

Fig. 25 Molecular theory of the yeast NPC. **a** Schematic representation of the NPC. Reprinted with permission from Ref. [525]. **b** Stoichiometry and amino-acid sequences of the FG-Nups. **c** Coarse-grained scaffold structure and anchor positions of the FG-Nups. **d** Spatial distributions of FG groups. **e** Spatial distribution of FG-Nups. **f** Electric potential and charge distribution throughout the NPC. All the color maps for amino acid concentrations are in the units of mM. The color map for electric potential is in the units of mV. Reprinted with permission from Ref. [511], Copyright 2020 Biophysical Journal

observed in single-molecule florescence experiment but cannot explain the central transporter revealed by electron microscopy [543].

Recent experiments showed that certain hydrophilic spacers are more cohesive than others [544], suggesting the molecular interactions are more complicated than previously thought. These cohesive spacers are distributed in subdomains on the sequences of FG-Nups, as shown in Fig. 25B. Recent experiments have also updated the anchor (Fig. 25C) and stoichiometry information [533,545] of the FG-Nups, which are key players in determining the gating structure of the biological nanopore. Taking these new experimental data into consideration, a structural model of NPC has been developed within the framework of molecular theory [511]. The model predicts a mosaic distribution of different FG groups in space as shown in Fig. 25D, suggesting different Kaps can take distinct transport pathways. The overall structure of the permeability barrier is a composite of condensates and low-density zones orchestrated by FG-Nups of different cohesiveness (Fig. 25E). Last but not least, Fig. 25F shows that the self-built electric potential throughout the NPC is highly polarized, although most of the opposite charges have similar spatial distributions with the net charge being relatively homogeneous in space. Together, these theoretical insights depict a gating picture in which the fast yet selective transport through the NPC is enabled by multiple routing mechanisms including FG, entropic, and electrostatic steering. The sequence–structure–function relation of the FG-Nups can be a great source of bioinspiration for the rational design of programmable nanopores functionalized by sequence-controlled copolymers.

To summarize, in this section we reviewed recent theories and models of polymer-coated nanopores in aqueous solution, with a special focus on the insights from molecular theory. Polymer-coated nanopores are potential solutions for biomedical, energy, and environmental problems, and also great model systems to study the molecular organization and transport at the nanoscale. The theoretical results reviewed here showcase the complexity of the coupling between different physical interactions and chemical reactions inside nanopores. Even for simple homopolymers, the topological constraints and spatial confinement can lead to considerable shift of reaction constants or new equilibria that cannot be described by classical theories. Going from homopolymer to copolymer coating materials opens broad avenues to design and engineer the gating properties of synthetic nanopores. Multiple stimuli responses can be integrated into a single nanopore with copolymer functionalization. We used the NPC as biological example to show how sequence optimized biopolymers arrange themselves into an intricate transporter of protein cargoes. These biological insights can be used to improve artificial nanofiltration toward higher selectivity and efficiency.

Given the richness of the topic, we have limited the review to thermodynamic equilibrium conditions. It is worth noting that external fields such as pressure and biased voltage can drive the system out of equilibrium. When the driving force is strong, the large molecular flux will deform the coating polymer, which will in return impact the transport. Understanding this coupling between coating morphology and molecular transport at non-equilibrium conditions is a theoretical challenge of practical importance.

Another phenomenon that is often associated with nanopores is symmetry breaking which allows for directional control of the confined transport. For example, solid-state nanopores with asymmetric shape such as conical nanopores can serve as ionic current rectifier.

Although in this review we mostly focused on symmetric nanopores (the NPC is the only asymmetric one), it merits a note that polymer coating provides an additional dimension for symmetry breaking in nanopores. Symmetric nanopores can acquire diode-like properties by surface modification of polymers in an asymmetric manner. Theoretical efforts are needed to understand the asymmetric transport under nanoconfinement and to guide the design of symmetry-broken nanopores.

10 General conclusions

In this work, we reviewed recent work on the structure, thermodynamics, and dynamics of water and aqueous systems confined in nanopores both of synthetic and biological origin. First, we showed that main questions on the thermodynamics of confined solutions are still open. For instance, while certain thermodynamic aspects of nanoconfined aqueous solutions are captured by Gibbs–Thompson equation and its extensions (for example, the melting temperature depression as a function of pore size and concentration), the current description of the glass transition is still incomplete since it lacks a proper consideration both of system–pore interactions and of possible nanosegregation effects. We also focused on the effect of confinement on water reactivity and on its dissociation constant by considering both size effects (confinement) and interfacial interactions, showing their mutual interplay and also exploring the spatial lengths at which each of them become prominent. The interplay between thermodynamics and dynamics for supercooled water within hydrophilic nanopores was also reviewed from results of computer simulations in order to elucidate the molecular determinants of water anomalies. Additionally, we reviewed the diffusion of water through small nanopores, with emphasis on superflow properties, a matter of great current applied interest. Within this context, we showed that computational studies provide relevant clues, but further experimental verifications are still required. The transport properties of ionic aqueous solutions were also reviewed with an eye on their impact on electrochemical systems of energy storage and conversion and also for water remediation. In turn, the structure and diffusion of nanoconfined aqueous solutions of ionic liquids were also reviewed tak-

ing into account the role of hydrophobic effects both on the structure and transport properties of the liquid. More generally, we also considered the interplay between local hydrophobicity and non-covalent interactions in model nanoconfined aqueous systems to show that simple extrapolations of ideas from bulk contexts might be misleading if the modulation effect induced by the local context is not taken into account, a fact that suggests design concepts that might be relevant for materials science and for biological systems. Finally, we also reviewed polymer-coated nanopores in aqueous solution evidencing the complexity of the coupling between different physical interactions and chemical reactions inside the nanopores which can lead, even in the simplest cases, to considerable shifts in the reaction constants of the chemical reaction taking place within them or the emergence of new equilibria. We also reviewed transport properties of these systems in relation to biological contexts of great interest. The way in which bioinspiration can guide advanced nanopore development and, in turn, how these models help to unravel main underpinnings of complex biological processes was also illustrated.

Acknowledgements JRB and MCB thank the Brazilian Agencies Capes, CNPq, and FAPERGS for the financial support. MPL, HRC, DS, GAA, MDE, JR, and DHL are members of CONICET. GAA acknowledges support form CONICET, UNS and ANPCyT (PICT 2017/3127). HRC thanks CONICET for the financial support (PIP 112 201301 00808). IS gratefully acknowledges funding from the National Science Foundation (USA) Biological and Environmental Interactions of Nanoscale Materials 1833214. CC and GF acknowledge the financial support of Spanish Grant PGC2018-099277-B-C22 funded by MCIN/AEI/10.13039/501100011033 and by "ERDF A way of making Europe". GF acknowledges the financial support of ICREA Foundation (ICREA Academia prize). GAA and HRC acknowledge support from CONICET, UBA, and CNEA for organizing the 3rd International Workshop "Structure and Dynamics of Glassy, Supercooled and Nanoconfined Fluids," Buenos Aires (Argentina), July 2019, which was the germ of this review work.

Author contribution statement

All authors contributed equally to the paper.

References

1. F. Franks, *Water: A Matrix of Life*, 2nd edn. (Royal Society of Chemistry, Cambridge, 2000)
2. C.A. Angell, in *Water: A Comprehensive Treatise*, vol. 7, ed. by F. Franks (Plenum, New York, 1982)
3. P.G. Debenedetti, J. Phys.: Condens. Matter **15**, R1669 (2003)
4. M. Chaplin, Anomalous properties of water. http://www.lsbu.ac.uk/water/anmlies.html (2020)
5. P. Ball, Chem. Rev. **108**, 74 (2008)
6. P. Gallo et al., Chem. Rev. **116**, 7463 (2016)
7. P. Gallo, H.E. Stanley, Science **358**, 1543 (2017)
8. J.W.F. Robertson, Biological pores on lipid bilayers, in *Engineered Nanopores for Bioanalytical Applications. Chap. 4*. ed. by J.B. Edel, T. Albrecht (Elsevier, Amsterdam, 2013)
9. C.I. Lynch, S. Rao, M.S.P. Sansom, Chem. Rev. **120**, 10298 (2020)
10. K. Zhang, L. Liu, G. Huang, Geophys. Res. Lett. **47**, e2020GL087999 (2020)
11. D. Cohen-Tanugi, J.C. Grossman, Nano Lett. **12**, 3602 (2012)
12. J. Qian, X. Gao, B. Pan, Environ. Sci. Technol. **54**, 8509 (2020)
13. L. Xu, J. Wang, Crit. Rev. Environ. Sci. Technol. **47**, 1042 (2017)
14. M. Macha, S. Marion, V.V.R. Nandigana, A. Radenovic, Nat. Rev. Mater. **4**, 588 (2019)
15. P. Bampoulis, K. Sotthewes, E. Dollekamp, B. Poelsema, Surf. Sci. Rep. **73**, 233 (2018)
16. I.N. Tsimpanogiannis, O.A. Moultos, L.F.M. Franco, M.B. de M Spera, M. Erdős, I.G. Economou, Mol. Simul. **45**, 425 (2018)
17. O. Mishima, H.E. Stanley, Nature **396**, 329 (1998)
18. A. Bogdan, T. Loerting, J. Chem. Phys. **141**, 18C533 (2014)
19. H. Findenegg, S. Jähnert, D. Akcakayian, A. Schreiber, Chem. Phys. Chem. **9**, 2651 (2008)
20. R. Denoyel, R.J.M. Pellenq, Langmuir **18**, 2710 (2002)
21. O. Petrov, I. Furó, Phys. Rev. E **73**, 011608 (2006)
22. G.K. Rennie, J. Clifford, J. Chem. Soc. Faraday Trans. 1 **73**, 680 (1977)
23. Y. Hirama, T. Takahashi, M. Hino, T. Sato, J. Colloid Interface Sci. **184**, 349 (1996)
24. E.W. Hansen, H.C. Gran, E.J. Sellevold, J. Phys. Chem. B **101**, 7027 (1997)
25. K. Morishige, K. Kawano, J. Chem. Phys. **110**, 4867 (1999)
26. A. Schreiber, I. Ketelsen, G.H. Findenegg, Phys. Chem. Chem. Phys. **3**, 1185 (2001)
27. S. Kittaka, S. Ishimaru, M. Kuranishi, T. Matsuda, T. Yamaguchi, Phys. Chem. Chem. Phys. **8**, 3223 (2006)
28. S. Kittaka, M. Kuranishi, S. Ishimaru, O. Umahara, J. Chem. Phys. **126**, 091103 (2007)
29. S. Kittaka, Y. Ueda, F. Fujisaki, T. Iiyama, T. Yamaguchi, Phys. Chem. Chem. Phys. **13**, 17222 (2011)
30. E.N. Ashworth, F.B. Abeles, Plant Physiol. **76**, 201 (1984)
31. P. Mazur, Ann. N. Y. Acad. Sci. **125**, 658 (1965)
32. J.P. Acker, J.A.W. Elliott, L.E. McGann, Biophys. J . **81**, 1389 (2001)
33. F. Liu, L. Zargarzadeh, H.-J.- Chung, J.A.E. Elliot, J. Phys. Chem. B **121**, 9452 (2017)
34. C.M. Burba, J. Janzen, Thermochim. Acta **615**, 81 (2015)
35. E. Jantsch, C. Weinberg, M. Tiermann, T. Koop, J. Phys. Chem. C **123**, 24566 (2019)
36. D.C. Martinez-Casillas, M.P. Longinotti, M.M. Bruno, F. Vaca Chavéz, R.H. Acosta, H.R. Corti, J. Phys. Chem. C **122**, 3638 (2018)
37. Z.-X. Luo, Y.-Z. Xing, Y.-C. Ling, A. Kleinhammes, Y. Wu, Nat. Commun. **6**, 6358 (2015)

38. T. Koop, B. Luo, A. Tsias, T. Peter, Nature **406**, 611 (2000)
39. T. Koop, Z. Phys. Chem. **218**, 1231 (2004)
40. R.M. Leberman, A.M. Soper, Nature **378**, 364 (1995)
41. J. Meissmer, A. Paruse, G. Findenegg, J. Phys. Chem. Lett. **7**, 1816 (2016)
42. K. Hofer, R. Mayer, G.P. Johari, J. Phys. Chem. **95**, 7100 (1991)
43. K. Elamin, H. Jasson, S. Kittaka, J. Swenson. Phys. Chem. Chem. Phys. **15**, 18437 (2013)
44. K. Elamin, J. Björklund, K. Nyhlén, M. Yttergren, L. Märtensson, J. Swenson, J. Chem. Phys. **141**, 034505 (2014)
45. L. Zhao, L. Pan, Z. Cao, Q. Wang, Chem. Phys. Lett. **647**, 170 (2016)
46. J. Swenson, K. Elamin, G. Chen, W. Lohstroh, V. Garcia Sakai, J. Chem. Phys. **141**, 214501 (2014)
47. J. Swenson, K. Elamin, H. Jasson, S. Kittaka, Chem. Phys. **423**, 20 (2013)
48. M.P. Longinotti, V. Fuentes-Landete, T. Loerting, H.R. Corti, J. Chem. Phys. **151**, 064509 (2019)
49. I. Angarita, M.F. Mazzobre, H.R. Corti, Phys. Chem. Chem. Phys. **23**, 17018 (2021)
50. G.P. Johari, A. Hallbrucker, E. Mayer, Nature **330**, 552 (1987)
51. K. Murata, H. Tanaka, Nat. Mater. **11**, 436 (2012)
52. O. Mishima, L.D. Calvert, E. Whalley, Nature **76**, 314 (1985)
53. V. Soprunyuk, W. Schranz, Soft Matter **14**, 7246 (2018)
54. Z. Wei, Y. Li, R.G. Cooks, X. Yan, Ann. Rev. Phys. Chem. **71**, 31 (2020)
55. A. Grommet, M. Feller, R. Klajn, Nat. Nanotechnol. **15**, 256 (2020)
56. K. Fu, S.R. Kwon, D. Han, P.W. Bohn, Acc. Chem. Res. **53**, 719 (2020)
57. J. Zhong, M. Kumar, J.S. Francisco, X.C. Zeng, Acc. Chem. Res. **51**, 1229 (2018)
58. C.E. Kolb, D.R. Worsnop, Ann. Rev. Phys. Chem. **63**, 471 (2012)
59. A. Küchler, M. Yoshimoto, S. Luginbuhl, F. Mavelli, P. Walde, Nat. Nanotechnol. **11**, 409 (2016)
60. F. Persson, B. Halle, Proc. Natl. Acad. Sci. U.S.A. **112**, 10383 (2015)
61. M. Eigen, L. De Maeyer, J.D. Bernal, Proc. Royal Soc. Lond. Ser. A **247**, 505 (1958)
62. R. Car, M. Parrinello, M. Phys, Rev. Lett. **55**, 2471 (1985)
63. M. Tuckerman, K. Laasonen, M. Sprik, M. Parrinello, J. Phys. Chem. **99**, 5749 (1995)
64. B.L. Trout, M. Parrinello, Chem. Phys. Lett. **288**, 343 (1998)
65. M. Sprik, Chem. Phys. **258**, 139 (2000)
66. P.L. Geissler, C. Dellago, D. Chandler, J. Hutter, M. Parrinello, Science **291**, 2121 (2001)
67. A. Hassanali, M.K. Prakash, H. Eshet, M. Parrinello, Proc. Natl. Acad. Sci. U.S.A. **108**, 20410 (2011)
68. A.A. Hassanali, F. Giberti, G. Sosso, M. Parrinello, Chem. Phys. Lett. **599**, 133 (2014)
69. Y.L.S. Tse, C. Chen, G.E. Lindberg, R. Kumar, G.A. Voth, J. Am. Chem. Soc. **137**, 12610 (2015)
70. J. Cuny, A.A. Hassanali, J. Phys. Chem. B **118**, 13903 (2014)
71. A.A. Hassanali, F. Giberti, J. Cuny, T.D. Kuhne, M. Parrinello, Proc. Natl. Acad. Sci. U.S.A. **110**, 13723 (2013)
72. N. Agmon, H.J. Bakker, R.K. Campen, R.H. Henchman, P. Pohl et al., Chem. Rev. **116**, 7642 (2016)
73. M. Strajbl, G. Hong, A.J. Warshel, Phys. Chem. B **106**, 13333 (2002)
74. Z. Cao, Y. Peng, T. Yan, S. Li, A. Li, G.A. Voth, J. Am. Chem. Soc. **132**, 11395 (2010)
75. C. Knight, G.A. Voth, Acc. Chem. Res. **45**, 101 (2012)
76. J. Behler, M. Parrinello, Phys. Rev. Lett. **98**, 146401 (2007)
77. T. Morawietz, A. Singraber, C. Dellago, J. Behler, Proc. Natl. Acad. Sci. U.S.A. **113**, 8368 (2016)
78. B. Cheng, E.A. Engel, J. Behler, C. Dellago, M. Ceriotti, Proc. Natl Acad. Sci. U. S. A **116**, 1110 (2019)
79. R. Yuan, J.A. Napoli, C. Yan, O. Marsalek, T.E. Markland, M.D. Fayer, ACS Centr. Sci. **5**, 1269 (2019)
80. F. Pietrucci, A.M. Saitta, Proc. Natl. Acad. Sci. U.S.A. **112**, 15030 (2015)
81. X. Yan, R.M. Bain, R.G. Cooks, Angew. Chem. Int. Ed. **55**, 12960 (2016)
82. J. Fenn, M. Mann, C. Meng, S. Wong, C. Whitehouse, Science **246**, 64 (1989)
83. E. Crawford, C. Esen, D. Volmer, Anal. Chem. **88**, 8396 (2016)
84. R.M. Bain, C.J. Pulliam, F. Thery, R.G. Cooks, Angew. Chem. Int. Ed. **55**, 10478 (2016)
85. M. Girod, E. Moyano, D.I. Campbell, R.G. Cooks, Chem. Sci. **2**, 501 (2011)
86. T. Müller, A. Badu-Tawiah, R.G. Cooks, Angew. Chem. Int. Ed. **51**, 11832 (2012)
87. A. Li, Q. Luo, S. Park, R. Cooks, Angew. Chem. Int. Ed. **53**, 3147 (2014)
88. R. Bain, C. Pulliam, R. Cooks, Chem. Sci. **6**, 397 (2015)
89. J.K. Lee, D. Samanta, H.G. Nam, R.N. Zare, J. Am. Chem. Soc. **141**, 10585 (2019)
90. A. Gallo, A.S.F. Farinha, M. Dinis, A.-H. Emwas, A. Santana et al., Chem. Sci. **10**, 2566 (2019)
91. S. Mondal, S. Acharya, R. Biswas, B. Bagchi, R.N. Zare, J. Chem. Phys. **148**, 244704 (2018)
92. M. Polak, L. Rubinovich, Nano Lett. **8**, 3543 (2008)
93. T. Dwars, E. Paetzold, G. Oehme, Angew. Chem. Int. Ed. **44**, 7174 (2005)
94. D.M. Vriezema, M. Comellas Aragones, J.A.A.W. Elemans, J.J.L.M. Cornelissen, A.E. Rowan, R.J.M. Nolte, Chem. Rev. **105**, 1445 (2005)
95. J.H. Fendler, Acc. Chem. Res. **9**, 153 (1976)
96. H. Morawetz, Advances in catalysis, in *Catalysis and Inhibition in Solutions of Synthetic Polymers and in Micellar Solutions*, vol. 20, ed. by D. Eley, H. Pines, P.B. Weisz (Academic Press, London, 1969), pp. 341–371
97. N.E. Levinger, Science **298**, 1722 (2002)
98. M.-J. Schwuger, K. Stickdorn, R. Schomaecker, Chem. Rev. **95**, 849 (1995)
99. B. Smit, T. Maesen, Nature **451**, 671 (2008)
100. A. Patra, T. Luong, R. Mitra, M. Havenith, Phys. Chem. Chem. Phys. **15**, 930 (2013)
101. A. Das, A. Patra, R. Mitra, J. Phys. Chem. B **117**, 3593 (2013)

102. R.K. Mitra, S.S. Sinha, P.K. Verma, S.K. Pal, J. Phys. Chem. B **112**, 12946 (2008)
103. M. Sedgwick, R.L. Cole, C.D. Rithner, D.C. Crans, N.E. Levinger, J. Am. Chem. Soc. **134**, 11904 (2012)
104. C. Lawler, M.D. Fayer, J. Phys. Chem. B **119**, 6024 (2015)
105. A. Fallah-Araghi, K. Meguellati, J.-C. Baret, A.E. Harrak, T. Mangeat et al., Phys. Rev. Lett. **112**, 028301 (2014)
106. T.J. Pinnavaia, Science **220**, 365 (1983)
107. M.M. Mortland, J.J. Fripiat, J. Chaussidon, J. Uytterhoeven, J. Phys. Chem. **67**, 248 (1963)
108. J.D. Russell, Trans. Faraday Soc. **61**, 2284 (1965)
109. J. Wei, M. Zhou, A. Long, Y. Xue, H. Liao, C. Wei, Z. Xu, Nano-Micro Lett. **10**, 75 (2018)
110. Z.W. Seh, J. Kibsgaard, C.F. Dickens, I. Chorkendorff, J.K. Nørskov, T.F. Jaramillo, Science **355**, eaad4998 (2017)
111. R. Zhang, P.E. Pearce, Y. Duan, N. Dubouis, T. Marchandier, A. Grimaud, Chem. Mater. **31**, 8248 (2019)
112. S. Li, S. Sirisomboonchai, X. An, X. Ma, P. Li et al., Nanoscale **12**, 6810 (2020)
113. M. Duc, F. Gaboriaud, F. Thomas, J. Coll. Interface Sci. **289**, 139 (2005)
114. J. Hunger, S.H. Parekh, Science **357**, 755 (2017)
115. C. Macias-Romero, I. Nahalka, H.I. Okur, S. Roke, Science **357**, 784 (2017)
116. A. Ali, R. Golnak, R. Seidel, B. Winter, J. Xiao, A.C.S. Appl, Nano Mater. **3**, 264 (2020)
117. Y. Hashikawa, S. Hasegawa, Y. Murata, Chem. Commun. **54**, 13686 (2018)
118. V. Mouarrawis, R. Plessius, J.I. van der Vlugt, J.N.H. Reek, Front. Chem. **6**, 623 (2018)
119. S.A. Miners, G.A. Rance, A.N. Khlobystov, Chem. Soc. Rev. **45**, 4727 (2016)
120. X. Pan, X. Bao, Acc. Chem. Res. **44**, 553 (2011)
121. J. Cheng, M. Sprik, J. Chem. Theory Comput. **6**, 880 (2010)
122. S. Tazi, B. Rotenberg, M. Salanne, M. Sprik, M. Sulpizi, Geochim. Cosmochim. Acta **94**, 1 (2012)
123. M. Sulpizi, M.P. Gaigeot, M. Sprik, Chem. Theory Comput. **8**, 1037 (2012)
124. M.P. Gaigeot, M. Sprik, M. Sulpizi, J. Phys.: Cond. Matter **24**, 124106 (2012)
125. X. Liu, J. Cheng, M. Sprik, X. Lu, R. Wang, Geochim. Cosmochim. Acta **120**, 487 (2013)
126. X. Liu, J. Cheng, M. Sprik, X. Lu, R. Wang, Geochim. Cosmochim. Acta **168**, 293 (2015)
127. M.L. Machesky, M. Předota, D.J. Wesolowski, L. Vlcek, P.T. Cummings et al., Langmuir **24**, 12331 (2008)
128. M. Sumita, C. Hu, Y. Tateyama, J. Phys. Chem. C **114**, 18529 (2010)
129. H. Cheng, A. Selloni, Langmuir **26**, 11518 (2010)
130. V.M. Sánchez, E. de la Llave, D.A. Scherlis, Langmuir **27**, 2411 (2011)
131. V.M. Sánchez, M. Sued, D.A. Scherlis, J. Chem. Phys. **131**, 174108 (2009)
132. K. Leung, L.J. Criscenti, J. Phys.: Condens. Matter **24**, 124105 (2012)
133. F. Nattino, M. Truscott, N. Marzari, O. Andreussi, J. Chem. Phys. **150**, 041722 (2019)
134. K. Schwarz, R. Sundararaman, Surf. Sci. Rep. **75**, 100492 (2020)
135. J.R. Rustad, A.R. Felmy, E.J. Bylaska, Geochim. Cosmochim. Acta **67**, 1001 (2003)
136. J.R. Rustad, A.R. Felmy, Geochim. Cosmochim. Acta **69**, 1405 (2005)
137. H. Manzano, S. Moeini, F. Marinelli, A.C.T. van Duin, F.-J. Ulm, R.J.-M. Pellenq, J. Am. Chem. Soc. **134**, 2208 (2012)
138. M.J.A. Qomi, M. Bauchy, F.-J. Ulm, R.J.-M. Pellenq, J. Chem. Phys. **140**, 054515 (2014)
139. D. Hou, T. Zhao, H. Ma, Z. Li, J. Phys. Chem. C **119**, 1346 (2015)
140. D. Hou, D. Li, T. Zhao, Z. Li, Langmuir **32**, 4153 (2016)
141. S. Masoumi, S. Zare, H. Valipour, M.J. Abdolhosseini Qomi, J. Phys. Chem. C **123**, 4755 (2019)
142. X. Liu, X. Lu, R. Wang, E.J. Meijer, H. Zhou, Geochim. Cosmochim. Acta **75**, 4978 (2011)
143. C. Wittekindt, D. Marx, J. Chem. Phys. **137**, 054710 (2012)
144. D. Muñoz-Santiburcio, C. Wittekindt, D. Marx, Nat. Commun. **4**, 2349 (2013)
145. D. Muñoz-Santiburcio, D. Marx, Nat. Commun. **7**, 12625 (2016)
146. D. Muñoz-Santiburcio, D. Marx, Phys. Rev. Lett. **119**, 056002 (2017)
147. D. Muñoz-Santiburcio, D. Marx, Chem. Sci. **8**, 3444 (2017)
148. Y.A.P. Sirkin, A. Hassanali, D.A. Scherlis, J. Phys. Chem. Lett. **9**, 5029 (2018)
149. C. Dellago, M.M. Naor, G. Hummer, Phys. Rev. Lett. **90**, 105902 (2003)
150. D.J. Mann, M.D. Halls, Phys. Rev. Lett. **90**, 195503 (2003)
151. J. Chen, X.-Z. Li, Q. Zhang, A. Michaelides, E. Wang, Phys. Chem. Chem. Phys. **15**, 6344 (2013)
152. Z. Cao, Y. Peng, T. Yan, S. Li, A. Li, G.A. Voth, J. Am. Chem. Soc. **132**, 11395 (2010)
153. M. Rossi, M. Ceriotti, D.E. Manolopoulos, J. Phys. Chem. Lett. **7**, 3001 (2016)
154. N. Agmon, Chem. Phys. Lett. **244**, 456 (1995)
155. D. Marx, A. Chandra, M.E. Tuckerman, Chem. Rev. **110**, 2174 (2010)
156. P.E. Videla, P.J. Rossky, D. Laria, J. Chem. Phys. **139**, 174315 (2013)
157. L. Turi, J. Rodriguez, D. Laria, J. Phys. Chem. B **124**, 2198 (2020)
158. P.E. Videla, P.J. Rossky, D. Laria, J. Phys. Chem. Lett. **5**, 2375 (2014)
159. P.E. Videla, P.J. Rossky, D. Laria, J. Chem. Phys. **148**, 084303 (2018)
160. P. Gallo, M. Rovere, J. Phys.: Condens. Matter **22**, 280301 (2010)
161. P. Gallo, T. Loerting, F. Sciortino, J. Chem. Phys. **151**, 210401 (2019)
162. P. Poole, F. Sciortino, U. Essmann, H. Stanley, Nature **360**, 324 (1992)
163. O. Mishima, H. Stanley, Nature **392**, 164 (1998)
164. K.H. Kim, A. Sph, H. Pathak, F. Perakis, D. Mariedahl et al., Science **358**, 1589 (2017)
165. J.C. Palmer, P.H. Poole, F. Sciortino, P.G. Debenedetti, Chem. Rev. **118**, 9129 (2018)

166. K.H. Kim, K. Amann-Winkel, N. Giovambattista, A. Späh, F. Perakis et al., Science **370**, 978 (2020)
167. G. Franzese, H. Stanley, J. Phys. Condens. Matt. **19**, 205126 (2007)
168. K. Ito, C. Moynihan, C. Angell, Nature **398**, 492 (1999)
169. L. Liu, S.H. Chen, A. Faraone, C.W. Yen, C.Y. Mou, Phys. Rev. Lett. **95**, 117802 (2005)
170. L. Xu, P. Kumar, S.V. Buldyrev, S.H. Chen, P.H. Poole, F. Sciortino, H.E. Stanley, Proc. Nat. Acad. Sci. U.S.A. **102**, 16558 (2005)
171. P. Gallo, M. Rovere, J. Chem. Phys. **137**, 164503 (2012)
172. M. De Marzio, G. Camisasca, M. Rovere, P. Gallo, J. Chem. Phys. **144**, 074503 (2016)
173. M. De Marzio, G. Camisasca, M. Rovere, P. Gallo, J. Chem. Phys. **146**, 084502 (2017)
174. P. Gallo, M. Rovere, S.H. Chen, J. Phys. Chem. Lett. **1**, 729 (2010)
175. P. Gallo, D. Corradini, M. Rovere, J. Chem. Phys. **139**, 204503 (2013)
176. S.H. Chen, L. Liu, E. Fratini, P. Baglioni, A. Faraone, E. Mamontov, Proc. Nat. Acad. Sci. U.S.A. **103**, 9012 (2006)
177. G. Camisasca, M. De Marzio, D. Corradini, P. Gallo, J. Chem. Phys. **145**, 044503 (2016)
178. A. Iorio, G. Camisasca, P. Gallo, J. Mol. Liq. **282**, 617 (2019)
179. P. Gallo, M. Rovere, E. Spohr, Phys. Rev. Lett. **85**, 4317 (2000)
180. P. Gallo, M. Rovere, E. Spohr, J. Chem. Phys. **113**, 11324 (2000)
181. P. Gallo, Phys. Chem. Chem. Phys. **2**, 1607 (2000)
182. P. Gallo, M. Rapinesi, M. Rovere, J. Chem. Phys. **117**, 369 (2002)
183. P. Gallo, M. Rovere, J. Phys.: Condens. Matter **15**, 7625 (2003)
184. H.J.C. Berendsen, J.R. Grigera, T.P. Straatsma, J.Phys. Chem. **91**, 6269 (1987)
185. P. Gallo, M. Rovere, S.H. Chen, J. Phys.: Condens. Matter **22**, 284102 (2010)
186. P. Gallo, M. Rovere, S.H. Chen, J. Phys.: Condens. Matter **24**, 064109 (2012)
187. M. De Marzio, G. Camisasca, M.M. Conde, M. Rovere, P. Gallo, J. Chem. Phys. **146**, 084505 (2017)
188. W. Götze, *Complex Dynamics of Glass-Forming Liquids* (Oxford University Press, New York, 2009)
189. P. Gallo, F. Sciortino, P. Tartaglia, S.H. Chen, Phys. Rev. Lett. **76**, 2730 (1996)
190. F. Sciortino, P. Gallo, P. Tartaglia, S.H. Chen, Phys. Rev. E **54**, 6331 (1996)
191. A. Faraone, L. Liu, C.Y. Mou, C.W. Yen, S.H. Chen, J. Chem. Phys. **121**, 10843 (2004)
192. F. Mallamace, M. Broccio, C. Corsaro, A. Faraone, U. Wanderlingh et al., J. Chem. Phys. **124**, 161102 (2006)
193. S.H. Chen, F. Mallamace, C.Y. Mou, M. Broccio, C. Corsaro, A. Faraone, L. Liu, Proc. Nat. Acad. Sci. U.S.A. **103**, 12974 (2006)
194. S.W. Starr, F. Sciortino, H.E. Stanley, Phys. Rev. E **60**, 6557 (1999)
195. M.E. Johnson, T. Head-Gordon, J. Chem. Phys. **130**, 214510 (2009)
196. Y. Rosenfeld, Phys. Rev. A **15**, 2545 (1977)
197. M. Agarwal, M.P. Alam, C. Chakravarty, J. Phys. Chem. B **115**, 6935 (2011)
198. P. Gallo, M. Rovere, Phys. Rev. E **91**, 012107 (2015)
199. C. Calero, G. Franzese, J. Mol. Liq. **317**, 114027 (2020)
200. L.B. Krott, J.R. Bordin, J. Chem. Phys. **139**, 154502 (2013)
201. J.L. Abascal, C. Vega, J. Chem. Phys. **123**, 234505 (2005)
202. J.B. Klauda, R.M. Venable, J.A. Freites, J.W. O'Connor, D.J. Tobias et al., J. Phys. Chem. B **114**, 7830 (2010)
203. J. Engstler, N. Giovambattista, J. Phys. Chem. B **122**, 8908 (2018)
204. N. Giovambattista, P.J. Rossky, P.G. Debenedetti, Phys. Rev. E **73**, 041604 (2006)
205. J. Martí, C. Calero, G. Franzese, Entropy **19**, 135 (2017)
206. M.M. Conde, M.A. Gonzalez, J.L.F. Abascal, C. Vega, J. Chem. Phys. **139**, 154505 (2013)
207. B. Radha, A. Esfandiar, F.C. Wang, A.P. Rooney, K. Gopinadhan et al., Nature **538**, 222 (2016)
208. J. Gao, W.D. Luedtke, U. Landman, Phys. Rev. Lett. **79**, 705 (1997)
209. J. Gao, W. Luedtke, U. Landman, J. Phys. Chem. B **101**, 4013 (1997)
210. K. Xu, P. Cao, J.R. Heath, Science **329**, 1188 (2010)
211. A. Calò, N. Domingo, S. Santos, A. Verdaguer, J. Phys. Chem. C **119**, 8258 (2015)
212. S. Santos, A. Verdaguer, Materials **9**, 182 (2016)
213. E.A. Jagla, J. Chem. Phys. **111**, 8980 (1999)
214. A.B. de Oliveira, P.A. Netz, T. Colla, M.C. Barbosa, J. Chem. Phys. **125**, 124503 (2006)
215. F. Leoni, G. Franzese, J. Chem. Phys. **141**, 174501 (2014)
216. P. Vilaseca, G. Franzese, J. Non-Cryst, Solids **357**, 419 (2011)
217. L.B. Krott, J.R. Bordin, N.M. Barraz, M.C. Barbosa, J. Chem. Phys. **142**, 134502 (2015)
218. J.R. Bordin, L.B. Krott, M.C. Barbosa, J. Chem. Phys. **141**, 144502 (2014)
219. L. Yang, Y. Guo, Nanotechnology **31**, 235702 (2020)
220. C.A. Angell, E.D. Finch, P. Bach, J. Chem. Phys. **65**, 3063 (1976)
221. P. Netz, F. Starr, M.C. Barbosa, H. Stanley, Phys. A **314**, 470 (2002)
222. P. Netz, F. Starr, M. Barbosa, H. Stanley, J. Molecular Liq. **101**, 159 (2002)
223. F. de los Santos, G. Franzese, Phys. Rev. E **85**, 010602 (2012)
224. J. Martí, M.C. Gordillo, J. Chem. Phys. **114**, 10486 (2001)
225. J. Martí, M.C. Gordillo, Phys. Rev. B **63**, 165430 (2001)
226. F. Calabró, K. Lee, D. Mattia, Appl. Mathem. Lett. **26**, 991 (2013)
227. D. Mattia, F. Calabró, Microfluid. Nanofluid. **13**, 125 (2012)
228. R.J. Mashl, S. Joseph, N.R. Aluru, E. Jakobsson, Nano Lett. **3**, 589 (2003)
229. A.B. Farimani, N.R. Aluru, J. Phys. Chem. B **115**, 12145 (2011)
230. J.R. Bordin, A.B. de Oliveira, A. Diehl, M.C. Barbosa, J. Chem. Phys. **137**, 084504 (2012)

231. M. Majumder, N. Chopra, R. Andrews, B.J. Hinds, Nature **438**, 44 (2005)
232. J.K. Holt, H.G. Park, Y. Wang, M. Stadermann, A.B. Artyukhin et al., Science **312**, 1034 (2006)
233. X. Qin, Q. Yuan, Y. Zhao, S. Xie, Z. Liu, Nanoletters **11**, 2173 (2011)
234. E. Secchi, S. Marbach, A. Nigues, D. Stein, A. Siria, L. Bocquet, Nature **537**, 210 (2016)
235. A. Striolo, Nano Lett. **6**, 633 (2006)
236. J.A. Thomas, A.J.H. McGaughey, Nano Lett. **8**, 2788 (2008)
237. J.A. Thomas, A.J.H. McGaughey, Phys. Rev. Lett. **102**, 184502 (2009)
238. J.R. Bordin, J.S. Andrade, A. Diehl, M.C. Barbosa, J. Chem. Phys. **140**, 194504 (2014)
239. L. Joly, J. Chem. Phys. **135**, 214705 (2011)
240. J.B. Sokoloff, Phys. Rev. E **100**, 023112 (2019)
241. J.R. Bordin, A. Diehl, M.C. Barbosa, J. Phys. Chem. B **117**, 7047 (2013)
242. J. Hassan, G. Diamantopoulos, L. Gkoura, M. Karagianni, S. Alhassan et al., J. Phys. Chem. C **122**, 10600 (2018)
243. A. Parmentier, M. Maccarini, A. De Francesco, L. Scaccia, G. Rogati et al., Phys. Chem. Chem. Phys. **21**, 21456 (2019)
244. K. Balasubramanian, M. Burghard, Small **1**, 180 (2005)
245. F.M. Machado, S.A. Carmalin, E.C. Lima, S.L.P. Dias, L.D.T. Prola et al., J. Phys. Chem. C **120**, 18296 (2016)
246. A. Bensghaier, S. Lau Truong, M. Seydou, A. Lamouri, E. Leroy et al., Langmuir **33**, 6677 (2017)
247. M.H. Köhler, J.R. Bordin, C.F. de Matos, M.C. Barbosa, Chem. Eng. Sci. **203**, 54 (2019)
248. G. Hummer, J.C. Rasaiah, J.P. Noworyta, Nature **414**, 188 (2001)
249. A. Striolo, Nanotechnology **18**, 475704 (2007)
250. D. Roy, N. Tiwari, M. Gupta, K. Mukhopadhyay, A.K. Saxena, J. Phys. Chem. C **119**, 716 (2015)
251. R. Duan, F. Xia, L. Jiang, ACS Nano **7**, 8344 (2013)
252. X. Hou, F. Yang, L. Li, Y. Song, L. Jiang, D. Zhu, J. Am. Chem. Soc. **132**, 11736 (2010)
253. L. Qu, L. Dai, E. Osawa, J. Am. Chem. Soc. **128**, 5523 (2006)
254. B.L. de Groot, H. Grubmüller, Curr. Opin. Struct. Biol. **15**, 176 (2005)
255. G. Zuo, R. Shen, S. Ma, W. Guo, ACS Nano **4**, 205 (2010)
256. F. Ramazani, F. Ebrahimi, J. Phys. Chem. C **120**, 12871 (2016)
257. Q. Chen, L. Meng, Q. Li, D. Wang, W. Guo, Z. Shuai, L. Jiang, Small **7**, 2225 (2011)
258. I. Moskowitz, M.A. Snyder, J. Mittal, J. Chem. Phys. **141**, 18C532 (2014)
259. J.R. Bordin, M.C. Barbosa, Phys. A **467**, 137 (2017)
260. Y. Xu, X. Tian, M. Lv, M. Deng, B. He et al., J. Phys. D Appl. Phys. **49**, 285302 (2016)
261. M. Foroutan, V.F. Naeini, M. Ebrahimi, Phys. Chem. Chem. Phys. **22**, 391 (2020)
262. M.H. Köhler, J.R. Bordin, L.B. da Silva, M.C. Barbosa, Phys. A **490**, 331 (2018)
263. M.H. Köhler, J.R. Bordin, L.B. da Silva, M.C. Barbosa, Phys. Chem. Chem. Phys. **19**, 12921 (2017)
264. M.H. Köhler, J.R. Bordin, J. Phys. Chem. C **122**, 6684 (2018)
265. B. Mendonça, P. Ternes, E. Salcedo, A.B. de Oliveira, M.C. Barbosa, J. Chem. Phys. **152**, 024708 (2020)
266. B. Mendonça, P. Ternes, E. Salcedo, A.B. de Oliveira, M.C. Barbosa, J. Chem. Phys. **153**, 244504 (2020)
267. K. Kwac, I. Kim, T.A. Pascal, W.A. Goddard, H.G. Park, Y. Jung, J. Phys. Chem. C **121**, 16021 (2017)
268. M.H. Köhler, C. Gavazzoni, J. Phys. Chem. C **123**, 13968 (2019)
269. Y.C. Zhongqiao Hu, J. Jiang, J. Chem. Phys. **134**, 134705 (2011)
270. C. Gavazzoni, N. Giovambattista, P.A. Netz, M.C. Barbosa, J. Chem. Phys. **146**, 234509 (2012)
271. P. Demontis, Gulín-González, G.B. Suffritti, J. Phys. Chem. C **116**, 11100 (2012)
272. F. Fornasiero, J.B. In, S. Kim, H.G. Park, Y. Yang, Langmuir **26**, 14848 (2010)
273. Z. Hu, Y. Chen, J. Jiang, J. Chem. Phys. **134**, 134705 (2011)
274. G. Guillen, E. Hoek, Chem. Eng. J. **149**, 221 (2009)
275. Z. Xu, C. Gao, Nat. Commun. **2**, 571 (2011)
276. Y. Wang, Z. He, K.M. Gupta, S.Q.R. Lu, Carbon **116**, 120 (2017)
277. S.P. Surwade, S.N. Smirnov, I.V. Vlassiouk, R.R. Unocic, G.M. Veith et al., Nat. Technol. **10**, 459 (2015)
278. K.A. Mahmoud, B. Mansoor, A. Mansour, M. Khraisheh, Desalination **356**, 208 (2015)
279. R.K. Joshi, P. Carbone, F.C. Wang, V.G. Kravets, Y. Su et al., Science **343**, 752 (2014)
280. M. Heiranian, A.B. Farimani, N.R. Aluru, Nat. Commun. **6**, 8616 (2015)
281. J. Abal, M.C. Barbosa, arXiv:2010.00688 (2020)
282. M.H. Köhler, J.R. Bordin, M.C. Barbosa, J. Chem. Phys. **148**, 222804 (2018)
283. M. Heiranian, A.B. Farimani, N.R. Aluru, Energy Environ. Sci. **4**, 1946 (2011)
284. J. Abal, J.R. Bordin, M.C. Barbosa, Phys. Chem. Chem. Phys. **22**, 11053 (2020)
285. H. Li, T.J. Ko, M. Lee, H.S. Chung, S.S. Han et al., Nanoletters **6**, 5194 (2019)
286. K.H. Jensen, A.X.C.N. Valente, H.A. Stone, Phys. Fluids **26**, 052004 (2014)
287. J. Abal, M.C. Barbosa, arXiv:2012.07795 (2021)
288. M. Zeng, M. Chen, D. Huang, S. Lei, X. Zhang, L. Wang, Z. Cheng, Mater. Horiz. **8**, 758 (2021)
289. R. Gusain, N. Kumar, S.S. Ray, Coord. Chem. Rev. **405**, 213111 (2020)
290. S. Mondal, B. Bagchi, J. Chem. Phys. **152**, 224707 (2020)
291. S. Faucher, M. Kuehne, V.B. Koman, N. Northrup, D. Kozawa et al., ACS Nano **15**, 2778 (2021)
292. J. Hassan, G. Diamantopoulos, L. Gkoura, M. Karagianni, S. Alhassan et al., J. Phys. Chem. C **122**, 10600 (2018)
293. K. Goh, Y. Chen, Nano Today **14**, 13 (2017)
294. E.W. Hansen, R. Schmidt, M. Stöcker, D. Akporiaye, Microporous Mater. **5**, 143 (1995)
295. R. Kimmich, S. Stapf, A.I. Maklakov, V.D. Skirda, E.V. Khozina, Magn. Res. Imaging **14**, 793 (1996)
296. L. Garro Linck, S.A. Maldonado Ochoa, H.R. Corti, G.A. Monti, F. Vaca Chávez, R.H. Acosta, Mesoporous Microporous Mater. **305**, 110351 (2020)

297. A. Kiwilsza, A. Pajzderska, M. A. Gonzalez, J. Mielcarek, J. Wasicki, J. Phys. Chem. C **119**, 16578 (2015)
298. H. Chemmi, D. Petit, P. Levitz, R. Denoyel, A. Galarneau, J.-P. Korb, J. Phys. Chem. Lett. **7**, 393 (2016)
299. D.C. Martinez-Casillas, M.P. Longinotti, M.M. Bruno, F. Vaca Chavéz, R.H. Acosta, H.R. Corti, J. Phys. Chem. C **122**, 3638 (2018)
300. D. Majolino, C. Corsaro, V. Crupi, V. Venuti, U. Wanderlingh, J. Phys. Chem. B **112**, 3927 (2008)
301. S. Takahara, M. Nakano, S. Kittaka, Y. Kuroda, T. Mori, H. Hamano, T. Yamaguchi, J. Phys. Chem. B **103**, 5814 (1999)
302. S. Takahara, N. Sumiyama, S. Kittaka, T. Yamaguchi, M.C. Bellissent-Funel, J. Phys. Chem. B **109**, 11231 (2005)
303. E. Mamontov, D.R. Cole, S. Dai, M.D. Pawel, C.D. Liang et al., Chem. Phys. **352**, 117 (2008)
304. H. Thompson, A.K. Soper, M.A. Ricci, F. Bruni, N.T. Skipper, J. Phys. Chem. B **111**, 5610 (2007)
305. D. Reìbiscoul, J. Cambedouzou, I. Matar Briman, M. Cabieì, H.-P. Brau, O. Diat, J. Phys. Chem. C **119**, 15982 (2015)
306. M. Baum, D. Rebiscoul, F. Juranyi, F. Rieutord, J. Phys. Chem. C **122**, 19857 (2018)
307. M. Baum, F. Rieutord, F. Juranyi, C. Rey, D. Reìbiscoul, Langmuir **35**, 10780 (2019)
308. S.A. Yamada, J.Y. Shin, W.H. Thompson, M.D. Fayer, J. Phys. Chem. C **123**, 5790 (2019)
309. N.D. Koone, J.D. Guo, T.W. Zerda, J. Non-Cryst, Solids **211**, 150 (1997)
310. J. Kunetz, L. Hench, J. Am. Ceram. Soc. **81**, 877 (1998)
311. R. Takahashi, S. Sato, T. Sodesawa, H. Nishida, Phys. Chem. Chem. Phys. **4**, 3800 (2002)
312. S.O. Diallo, Phys. Rev. E **92**, 012312 (2015)
313. K. Otake, K. Otsubo, T. Komatsu, S. Dekura, J.M. Taylor et al., Nat. Commun. **11**, 843 (2020)
314. G.L. Jackson, S.A. Kim, A. Jayaraman, S.O. Diallo, M.K. Mahanthappa, J. Phys. Chem. B **124**, 1495 (2020)
315. T.K. Tokunaga, S. Finsterle, Y. Kim, J. Wan, A. Lanzirotti, M. Newville, Environ. Sci. Technol. **51**, 4338 (2017)
316. T.H. van der Loop, N. Ottosson, T. Vad, W.F.C. Sager, H.J. Bakker, S. Woutersen, J. Chem. Phys. **146**, 131101 (2017)
317. J.J. Kasianowicz, J.W.F. Robertson, E.R. Chan, J.E. Reiner, V.M. Stanford, Ann. Rev. Anal. Chem. **1**, 737 (2008)
318. A. K. Friedman, L. A. Baker, In Nanoelectrochemistry, M. V. Mirkin, S. Amemiya Eds. Chap. 11. pp. 395-438 (2015)
319. H. Wang, J. Ettedgui, J. Forstater, J.W.F. Robertson, J.E. Reiner et al., ACS Sens. **3**, 252 (2018)
320. S. Sahu, M. Zwolak, Rev. Mod. Phys. **91**, 021004 (2019)
321. A. Siria, M.-L. Bocquet, L. Bocquet, Nat. Rev. Chem. **1**, 0091 (2017)
322. S.P. Surwade, S.N. Smirnov, I.V. Vlassiouk, R.R. Unocic, G.M. Veith, S. Dai, S.M. Mahurin, Nat. Nanotechnol. **10**, 459 (2015)
323. M. Salanne, B. Rotenberg, K. Naoi, K. Kaneko, P.-L. Taberna et al., Nat. Energy **1**, 1 (2016)
324. D. Stein, M. Kruithof, C. Dekker, Phys. Rev. Lett. **93**, 035901 (2004)
325. R. Fan, S. Huh, R. Yan, J. Arnold, P.D. Yang, Nat. Mater. **7**, 303 (2008)
326. C. Duan, A. Majumdar, Nat. Nanotechnol. **5**, 848 (2010)
327. J. Ma, K. Li, Z. Li, Y. Qiu, W. Si et al., J. Am. Chem. Soc. **141**, 4264 (2019)
328. A. Siria, P. Poncharal, A.L. Biance, R. Fulcrand, X. Blase, S.T. Purcell, L. Bocquet, Nature **494**, 458 (2013)
329. C. Ho, R. Qiao, J.B. Heng, A. Chatterjee, R.J. Timp, N.R. Aluru, G. Timp, Proc. Natl. Acad. Sci. U.S.A. **26**, 10445 (2005)
330. L. Bocquet, E. Charlaix, Chem. Soc. Rev. **39**, 1073 (2010)
331. A. Esfandiar, B. Radha, F. Wang, Q. Yang, S. Hu et al., Science **358**, 511 (2017)
332. E. Rigo, Z. Dong, J.H. Park, E. Kennedy, M. Hokmabadi et al., Nat. Commun. **10**, 2382 (2019)
333. R.H. Tunuguntla, F.I. Allen, K. Kim, A. Belliveau, A. Noy, Nat. Nanotechnol. **11**, 639 (2016)
334. B. Dong, L. Gwee, D. Salas de la Cruz, K.I. Winey, Y.A. Elabd, Nano Lett. **10**, 3785 (2010)
335. P. Pang, J. He, J.H. Park, P.S. Krstic, S. Lindsay, ACS Nano **5**, 7277 (2011)
336. Z.-X. Luo, Y.-Z. Xing, Y.-C. Ling, A. Kleinhammes, Y. Wu, Nat. Commun. **6**, 6358 (2015)
337. J.L. Anthony, E.J. Maginn, J.F. Brennecke, J. Phys. Chem. B **105**, 10942 (2001)
338. T. Takamuku, Y. Kyoshoin, T. Shimonura, S. Kittaka, T. Yamaguchi, J. Phys. Chem. B **113**, 10817 (2009)
339. T. Méndez-Morales, J. Carrete, O. Cabeza, L.J. Gallego, L.M. Varela, J. Phys. Chem. B **115**, 6995 (2011)
340. L. Cammarata, S.G. Kazarian, P.A. Salter, T. Welton, Phys. Chem. Chem. Phys. **3**, 5192 (2001)
341. C.G. Hanke, R.M. Lynden-Bell, J. Phys. Chem. B **107**, 10873 (2003)
342. B. Sun, Q. Jin, L. Tan, P. Wu, F. Yan, J. Phys. Chem. B **112**, 14251 (2008)
343. C. Spickermann, J. Thar, S.B.C. Lehmann, S. Zahn, J. Hunger et al., J. Chem. Phys. **129**, 104505 (2008)
344. M. Moreno, F. Catiglione, A. Mele, C. Pasqui, G. Raos, J. Phys. Chem. B **112**, 7826 (2008)
345. H. Wang, J. Wang, S. Zhang, X. Xuan, J. Phys. Chem. B **112**, 16682 (2008)
346. G. Schröder, G. Neumayr, O. Steinhauser, J. Chem. Phys. **130**, 194503 (2009)
347. W. Jian, Y. Wang, G.A. Voth, J. Phys. Chem. B **111**, 4812 (2007)
348. S. Feng, G.A. Voth, Fluid Phase Equilib. **294**, 148 (2010)
349. B.L. Bhargava, M.L. Klein, J. Phys. Chem. B **113**, 9499 (2009)
350. J. Łuczak, H. Hupka, J. Thoming, C. Jungnickel, Colloids Surf. A **329**, 125 (2008)
351. T. Singh, A. Kumar, J. Phys. Chem. B **111**, 7843 (2007)
352. B. Dong, X. Zhao, L. Zheng, J. Zhang, N. Li, T. Ionue, Colloids Surf. A **317**, 666 (2008)
353. F.-Y. Du, X.-H. Xiao, G.-K. Li, J. Chromatogr. A **1140**, 56 (2007)
354. J.G. Huddleston, H.D. Willauer, R.P. Swatloski, A.E. Visser, R.D. Rogers, Chem. Commun. **44**, 1765 (1998)

355. X. Zhao, Y. Gu, J. Li, H. Ding, Y. Shan, Catal. Commun. **9**, 2179 (2008)
356. A. Yokozeki, M.B. Shiflett, Ind. Eng. Chem. Res. **49**, 9496 (2010)
357. J. Zhang, Q. Zhang, X. Li, S. Liu, Y. Ma, F. Shi, Phys. Chem. Chem. Phys. **12**, 1971–1981 (2010)
358. M.-A. Néouze, J. Le Bideau, P. Gaveau, S. Bellayer, A. Vioux, Chem. Mater. **18**, 3931 (2006)
359. A. Chaumont, R. Schurhammer, G. Wipff, J. Phys. Chem. B **109**, 18964 (2005)
360. G. Chevrot, R. Schurhammer, G. Wipff, Phys. Chem. Chem. Phys. **8**, 4166 (2006)
361. R.M. Lynden-Bell, M. Del Pópolo, Phys. Chem. Chem. Phys. **8**, 949 (2006)
362. J. Picálek, B. Minofar, J. Kolafa, P. Jungwirth, Phys. Chem. Chem. Phys. **10**, 5765 (2008)
363. S. Rivera-Rubero, S. Baldelli, J. Am. Chem. Soc. **126**, 11788 (2004)
364. S. Baldelli, J. Phys. Chem. B **107**, 6148 (2003)
365. S. Rivera-Rubero, S. Baldelli, J. Phys. Chem. B **110**, 15499 (2006)
366. E. Gómez, B. González, A. Domínguez, E. Tojo, J. Tojo, J. Chem. Eng. Data **51**, 696 (2006)
367. N.J. English, D.A. Mooney, S.W. O'Brien, J. Mol. Liq. **157**, 163 (2010)
368. Y. Gu, C. Ogawa, J. Mori, S. Kobayashi, Angew. Chem. Int. Ed. **45**, 7217 (2006)
369. Y. Gu, C. Ogawa, S. Kobayashi, Organ. Lett. **9**, 175 (2007)
370. F. Borghi, A. Podestá, Adv. Phys. **5**, 1736949 (2020)
371. J. Rodriguez, M.D. Elola, D. Laria, J. Phys. Chem. C **116**, 5394 (2012)
372. R. Valiullin, S. Naumov, P. Galvosas, J. Kärger, H.-J. Woo, F. Porcheron, Nature **443**, 965–968 (2006)
373. M. Diaz, A. Ortiz, I. Ortiz, J. Membr. Sci. **469**, 379 (2014)
374. C. Pinilla, M.G. Del Pópolo, R.M. Lynden-Bell, J. Kohanoff, J. Chem. Phys. B **109**, 17922 (2015)
375. C. Pinilla, M.G. Del Pópolo, J. Kohanoff, R.M. Lynden-Bell, J. Phys. Chem. B **111**, 4877 (2007)
376. M.P. Singh, R.K. Singh, S. Chandra, J. Phys. Chem. B **115**, 7505 (2011)
377. B. Coasne, L. Viau, A. Voux, J. Phys. Chem. Lett. **2**, 1150 (2011)
378. C. Iacob, J.R. Sangoro, P. Papadopoulos, T. Schuber, S. Naumov et al., Phys. Chem. Chem. Phys. **12**, 13798 (2010)
379. T. Pal, C. Beck, D. Lessnich, M. Vogel, J. Phys. Chem. C **122**, 624 (2018)
380. W. Shi, D.C. Sorescu, J. Phys. Chem. B **114**, 15029 (2010)
381. C. Iacob, J.R. Sangoro, W.K. Kipnusu, R. Valiullin, J. Karger, F. Kremer, Soft Matter **8**, 289 (2012)
382. S.M. Chathoth, E. Mamontov, S. Dai, X. Wang, P.F. Fulvio, D.J. Wesolowski, EPL **97**, 66004 (2012)
383. Q. Berrod, F. Ferdeghini, P. Judeinstein, N. Genevaz, R. Ramos et al., Nanoscale **8**, 7845 (2016)
384. A. Ghoufi, A. Szymczyk, P. Malfreyt, Sci. Rep. **6**, 28518 (2016)
385. M. Foroutan, S.M. Fatemi, F.A. Esmaeilian, Eur. Phys. J. E **40**, 19 (2017)
386. M.D. Elola, J. Rodriguez, J. Phys. Chem. C **123**, 3622 (2019)
387. P.E. Videla, J. Sala, J. Martí, E. Guárdia, D. Laria, J. Chem. Phys. **135**, 104503 (2011)
388. R. Singh, J. Monk, F.R.A. Hung, J. Phys. Chem. C **114**, 15478 (2010)
389. G. Ori, F. Villemot, L. Viau, A. Vioux, B. Coasne, Mol. Phys. **112**, 1350 (2014)
390. G. Ori, C. Massobrio, A. Pradel, M. Ribes, B. Coasne, Langmuir **31**, 6742 (2015)
391. E.H. Lahrar, A. Belhboub, P. Simon, C. Merlet, A.C.S. Appl, Mater. Interfaces **12**, 1789 (2020)
392. J.-P. Hansen, I.R. McDonald, *Theory of Simple Liquids*, 3rd edn. (Academic Press, Elsevier, 2006)
393. O. Borodin, G.D. Smith, J. Phys. Chem. B **110**, 11481 (2006)
394. C. Schrôder, M. Haberler, O. Steinhauser, J. Chem. Phys. **128**, 134501 (2008)
395. M. Chen, R. Pendrill, G. Widmalm, J.W. Brady, J. Wohlert, J. Chem. Theory Comput. **10**, 4465 (2014)
396. J. Picálek, J. Kolafa, J. Mol. Liq. **134**, 29 (2007)
397. H.K. Kashyap, H.V.R. Annapureddy, F.O. Raineri, C.J. Margulis, J. Phys. Chem. B **115**, 13212 (2011)
398. O. Borodin, W. Gorecki, G.D. Smith, M. Armand, J. Phys. Chem. B **114**, 6786 (2010)
399. J. Trullás, J.A. Padró, Phys. Rev. B **55**, 12210 (1997)
400. J. Trullás, O. Alcaraz, L.E. González, M. Silbert, J. Phys. Chem. B **107**, 282 (2003)
401. C. Tasseven, J. Trullas, O. Alcaraz, M. Silbert, A. Giró, J. Chem. Phys. **106**, 7286 (1997)
402. T. Yamaguchi, A. Nagao, T. Matsuoka, S. Koda, J. Chem. Phys. **119**, 11306 (2003)
403. J. Rodriguez, M.D. Elola, D. Laria, J. Phys. Chem. B **113**, 12744 (2009)
404. M.N. Garaga, L. Aguilera, N. Yaghini, A. Matic, M. Persson, A. Martinelli, Phys. Chem. Chem. Phys. **19**, 5727 (2017)
405. S.R. Accordino, JM Montes. de Oca, J.A. Rodríguez Fris, G.A. Appignanesi, J. Chem. Phys. **143**, 154704 (2015)
406. L.M. Alarcón, JM Montes. de Oca, S.A. Accordino, J.A. RodríguezFris, G.A. Appignanesi, Fluid Phase Equilib. **362**, 81 (2014)
407. J.M. Montes de Oca, C.A. Menéndez, S.R. Accordino, D.C. Malaspina, G.A. Appignanesi, Eur. Phys. J. E **40**, 78 (2017)
408. N. Giovambattista, P.J. Rossky, P.G. Debenedetti, Annu. Rev. Phys. Chem. **63**, 179 (2012)
409. K. Lum, D. Chandler, J.D. Weeks, J. Phys. Chem. B **103**, 4570 (1999)
410. D. Huan, C.J. Margulis, B.J. Berne, Proc. Natl. Acad. Sci. U.S.A. **100**, 11953 (2003)
411. L. Hua, R. Zangi, B.J. Berne, J. Chem. Phys. C **113**, 5244 (2009)
412. S.R. Accordino, D.C. Malaspina, J.A. Rodríguez Fris, L.M. Alarcón, G.A. Appignanesi, Phys. Rev. E **85**, 031503 (2012)
413. S.R. Accordino, D.C. Malaspina, J.A. Rodríguez Fris, G.A. Appignanesi, Phys. Rev. Lett. **106**, 029801 (2011)
414. L.M. Alarcón, M.A. Frías, M.A. Morini, M.B. Sierra, G.A. Appignanesi, E.A. Disalvo, Eur. Phys. J. E **39**, 94 (2016)
415. J.M. Montes de Oca, F. Sciortino, G.A. Appignanesi, J. Chem. Phys. **152**, 244503 (2020)

416. A. Bizzarri, S. Cannistraro, J. Phys. Chem. B **106**, 6617 (2002)
417. D. Vitkup, D. Ringe, G.A. Petsko, M. Karplus, Nat. Struct. Biol. **7**, 34 (2000)
418. N. Choudhury, B. Montgomery Pettitt, J. Phys. Chem. B **109**, 6422 (2005)
419. H.E. Stanley, P. Kumar, L. Xu, Z. Yan, M.G. Mazza et al., Phys. A **386**, 729 (2007)
420. E.P. Schulz, L.M. Alarcón, G.A. Appignanesi, Eur. Phys. J. E **34**, 114 (2011)
421. D.C. Malaspina, E.P. Schulz, L.M. Alarcón, M.A. Frechero, G.A. Appignanesi, Eur. Phys. J. E **32**, 35 (2010)
422. L.M. Alarcón, D.C. Malaspina, E.P. Schulz, M.A. Frechero, G.A. Appignanesi, Chem. Phys. **388**, 47 (2011)
423. J.A. Rodríguez Fris, L.M. Alarcón, G.A. Appignanesi, Phys. Rev. E **76**, 011502 (2007)
424. J.A. Rodriguez Fris, G.A. Appignanesi, E. La Nave, F. Sciortino, Phys. Rev. E **75**, 041501 (2007)
425. J.M. Montes de Oca, S.R. Accordino, G.A. Appignanesi, P.H. Handle, F. Sciortino, J. Chem. Phys. **150**, 144505 (2019)
426. C. Calero, H.E. Stanley, G. Franzese, Materials **9**, 319 (2016)
427. A. Fernández, *Transformative Concepts for Drug Design: Target Wrapping*, vol. 1 (Springer, Heidelberg, 2010), pp. 1–224
428. A. Fernández, R. Scott, Phys. Rev. Lett. **91**, 018102 (2003)
429. S.R. Accordino, J.A. Rodríguez-Fris, G.A. Appignanesi, A. Fernández, Eur. Phys. J. E **35**, 59 (2012)
430. S.R. Accordino, M.A. Morini, M.B. Sierra, J.A. Rodríguez Fris, G.A. Appignanesi, A. Fernández, Proteins Struct. Funct. Bioinform. **80**, 1755 (2012)
431. M.B. Sierra, S.R. Accordino, J.A. Rodriguez-Fris, M.A. Morini, G.A. Appignanesi, A. Fernández Stigliano, Eur. Phys. J. E **36**, 62 (2013)
432. S.R. Accordino, J.A. Rodríguez Fris, G.A. Appignanesi, PLoS ONE **8**, e55123 (2013)
433. C.A. Menéndez, S.R. Accordino, D.C. Gerbino, G.A. Appignanesi, Eur. Phys. J. E **38**, 107 (2015)
434. C.A. Menéndez, S.R. Accordino, D.C. Gerbino, G.A. Appignanesi, PLoS ONE **11**, e0165767 (2016)
435. E. Schulz, M. Frechero, G.A. Appignanesi, A. Fernández, PLoS One **5**, e12844 (2010)
436. C. Wang, B.J. Berne, R.A. Friesner, Proc. Natl. Acad. Sci. U. S. A. **108**, 1326 (2011)
437. Z. Li, Y. Wang, A. Kozbial, G. Shenoy, F. Zhou et al., Nat. Mater. **12**, 925 (2013)
438. L. Li, D. Bedrov, G.D. Smith, J. Chem. Phys. **123**, 204504 (2005)
439. L. Li, D. Bedrov, G.D. Smith, J. Phys. Chem. B **110**, 10509 (2006)
440. M.V. Athawale, S.N. Jamadagni, S. Garde, J. Chem. Phys. **131**, 115102 (2009)
441. C.-J. Shih, S. Lin, M.S. Strano, D. Blankschtein, J. Am. Chem. Soc. **132**, 14638 (2010)
442. G. Hummer, J.C. Rasaiah, J.P. Noworyta, Nature **414**, 188 (2001)
443. S.N. Godawat, Jamadagni, S. Garde, Proc. Natl. Acad. Sci. U. S. A. **106**, 15119 (2009)
444. S. Jamadagni, R. Godawat, S. Garde, Annu. Rev. Chem. Biomol. Eng. **2**, 147 (2011)
445. P. Agre, Proc. Am. Thorac. Soc. **3**, 5 (2006)
446. B. Hille, *Ion Channels of Excitable Membranes*, 3rd edn. (Sinauer, Sunderland, MA, 2001)
447. M.P. Rout, J.D. Aitchison, A. Suprapto, K. Hjertaas, Y.M. Zhao, B.T. Chait, J. Cell Biol. **148**, 635 (2000)
448. L.G. Sheffield, H.B. Miskiewicz, L.B. Tannenbaum, S.S. Mirra, J. Neuropathol. Exp. Neurol. **65**, 45 (2006)
449. M. Heiranian, A.B. Farimani, N.R. Aluru, Nat. Commun. **6**, 8616 (2015)
450. S. Dervin, D.D. Dionysiou, S.C. Pillai, Nanoscale **8**, 15115 (2016)
451. R. Gimenez, M.G. Bellino, C.L.A. Berli, ACS Omega **3**, 16040 (2018)
452. I. Vlassiouk, T.R. Kozel, Z.S. Siwy, J. Am. Chem. Soc. **131**, 8211 (2009)
453. Z.S. Siwy, M. Davenport, Nat. Nanotechnol. **5**, 174 (2010)
454. A.B. Farimani, K. Min, N.R. Aluru, ACS Nano **8**, 7914 (2014)
455. C. Plesa, D. Verschueren, S. Pud, J. van der Torre, J.W. Ruitenberg et al., Nat. Nanotechnol. **11**, 1093 (2016)
456. W. Yang, L. Restrepo-Perez, M. Bengtson, S.J. Heerema, A. Birnie et al., Nano Lett. **18**, 6469 (2018)
457. R.R. Sanganna Gari, P. Seelheim, B. Liang, L.K. Tamm, ACS Sens. **4**, 1230 (2019)
458. Y.N. Jiang, N.N. Liu, W. Guo, F. Xia, L. Jiang, J. Am. Chem. Soc. **134**, 15395 (2012)
459. M. Ali, P. Ramirez, H.Q. Nguyen, S. Nasir, J. Cervera et al., ACS Nano **6**, 3631 (2012)
460. A. Smolyanitsky, E. Paulechka, K. Kroenlein, ACS Nano **12**, 6677 (2018)
461. A. Siria, P. Poncharal, A.-L. Biance, R. Fulcrand, X. Blase et al., Nature **494**, 455 (2013)
462. M. Macha, S. Marion, V.V.R. Nandigana, A. Radenovic, Nat. Rev. Mater. **4**, 588 (2019)
463. T. Ma, E. Balanzat, J.-M. Janot, S. Balme, A.C.S. Appl, Mater. Interfaces **11**, 12578 (2019)
464. G. Laucirica, A.G. Albesa, M.E. Toimil-Molares, C. Trautmann, W.A. Marmisolle, O. Azzaroni, Nano Energy **71**, 104612 (2020)
465. A.J. Storm, J.H. Chen, X.S. Ling, H.W. Zandbergen, C. Dekker, Nat. Mater. **2**, 537 (2003)
466. S. Hernandez-Ainsa, U.F. Keyser, Nanoscale **6**, 14121 (2014)
467. S. Howorka, Nat. Nanotechnol. **12**, 619 (2012)
468. Y.-A. Ren, H. Gao, X. Ouyang X, Chin. J. Chem. **36**, 875 (2018)
469. B. Yameen, M. Ali, R. Neumann, W. Ensinger, W. Knoll, O. Azzaroni, Nano Lett. **9**, 2788 (2009)
470. A. Calvo, B. Yameen, F.J. Williams, O. Azzaroni, G.J.A.A. Soler-Illia, Chem. Commun. **18**, 2553 (2009)
471. J.A. Armstrong, E.E.L. Bernal, A. Yaroshchuk, M.L. Bruening, Langmuir **29**, 10287 (2013)
472. L. Silies, A. Andrieu-Brunsen, Langmuir **34**, 807 (2018)
473. A.E. Abelow, I. Zharov, Soft Matter **5**, 457 (2009)
474. Y. Liebes-Peer, H. Rapaport, N. Ashkenasy, ACS Nano **8**, 6822 (2014)
475. X. Zhang, L. Zhang, J. Li, Anal. Chim. Acta **1057**, 36 (2019)
476. M. Ali, R. Neumann, W. Ensinger, ACS Nano **4**, 7267 (2010)

477. P. Gao, Q. Ma, D. Ding, D. Wang, X. Lou, T. Zhai, F. Xia, Nat. Commun. **9**, 4557 (2018)
478. X. Li, T. Zhai, P. Gao, H. Cheng, R. Hou, X. Lou, F. Xia, Nat. Commun. **9**, 40 (2018)
479. E.C. Yusko, J.M. Johnson, S. Majd, P. Prangkio, R.C. Rollings et al., Nat. Nanotechnol. **6**, 253 (2011)
480. L. Galla, A.J. Meyer, A. Spiering, A. Sischka, M. Mayer et al., Nano Lett. **14**, 4176 (2014)
481. G. Perez-Mitta, M.E. Toimil-Molares, C. Trautmann, W.A. Marmisolle, O. Azzaroni, Adv. Mater. **31**, 1901483 (2019)
482. X. Hou, W. Guo, L. Jiang, Chem. Soc. Rev. **40**, 2385 (2011)
483. M. Tagliazucchi, I. Szleifer, Mater. Today **18**, 131 (2015)
484. Z. Zhang, L. Wen, L. Jiang, Chem. Soc. Rev. **47**, 322 (2018)
485. J. Guo, J. Lee, C.I. Contescu, N.C. Gallego, S.T. Pantelides et al., Nat. Commun. **5**, 5389 (2014)
486. E.T. Acar, S.F. Buchsbaum, C. Combs, F. Fornasiero, Z.S. Siwy, Sci. Adv. **5**, eaav2568 (2019)
487. H.C. Zhang, X. Hou, L. Zeng, F. Yang, L. Li et al., J. Am. Chem. Soc. **135**, 16102 (2013)
488. Y. Sun, F. Zhang, J. Quan, F. Zhu, W. Hong et al., Nat. Commun. **9**, 2617 (2018)
489. J. Mo, A. Simha, M.G. Raizen, Phys. Rev. E **92**, 062106 (2015)
490. K. Huang, I. Szlufarska, Nat. Commun. **6**, 8558 (2015)
491. B. Ramos-Alvarado, S. Kumar, G.P. Peterson, Phys. Rev. E **93**, 033117 (2016)
492. X. Bian, C. Kim, G.E. Karniadakis, Soft Matter **12**, 6331 (2016)
493. S. De, N.R. Aluru, ACS Nano **12**, 368 (2018)
494. K. Falk, F. Sedlmeier, L. Joly, R.R. Netz, L. Bocquet, Nano Lett. **10**, 4067 (2010)
495. E. Secchi, S. Marbach, A. Nigues, D. Stein, A. Siria, L. Bocquet, Nature **537**, 210 (2016)
496. H. Daiguji, Chem. Soc. Rev. **39**, 901 (2010)
497. M. Tagliazucchi, I. Szleifer, Soft Matter **8**, 3292 (2012)
498. E. Gonzalez Solveyra, I. Szleifer, WIREs Nanomed. Nanobiotechnol. **8**, 334 (2016)
499. M. Tagliazucchi, O. Azzaroni, I. Szleifer, J. Am. Chem. Soc. **132**, 12404 (2010)
500. O. Peleg, M. Tagliazucchi, M. Kroeger, Y. Rabin, I. Szleifer, ACS Nano **5**, 4737 (2011)
501. L. Cheng, D. Cao, ACS Nano **5**, 1102 (2011)
502. D.I. Dimitrov, A. Milchev, K. Binder, J. Chem. Phys. **125**, 034905 (2006)
503. G. Chen, S. Das, J. Phys. Chem. B **119**, 12714 (2015)
504. C.-W. Li, H. Merlitz, C.-X. Wu, J.-U. Sommer, Macromolecules **51**, 6238 (2018)
505. M. Tagliazucchi, Y. Rabin, I. Szleifer, J. Am. Chem. Soc. **133**, 17753 (2011)
506. D. Osmanović, A. Fassati, I.J. Ford, B.W. Hoogenboom, Soft Matter **9**, 10442 (2013)
507. M. Tagliazucchi, Y. Rabin, I. Szleifer, ACS Nano **7**, 9085 (2013)
508. K. Huang, I. Szleifer, J. Am. Chem. Soc. **139**, 6422 (2017)
509. L.G. Lopez, R.J. Nap, Phys. Chem. Chem. Phys. **20**, 16657 (2018)
510. M. Tagliazucchi, K. Huang, I. Szleifer, J. Phys.: Condens. Matter **30**, 274006 (2018)
511. K. Huang, M. Tagliazucchi, S.H. Park, Y. Rabin, I. Szleifer, Biophys. J . **118**, 219 (2020)
512. H.S. Sachar, V.S. Sivasankar, S.A. Etha, G. Chen, S. Das, Electrophoresis **41**, 554 (2020)
513. R. Moussavi-Baygi, Y. Jamali, R. Karimi, M.R.K. Mofrad, PLoS Comput. Biol. **7**, e1002049 (2011)
514. J.S. Mincer, S.M. Simon, Proc. Natl. Acad. Sci. U. S. A. **108**, E351 (2011)
515. A. Ghavami, L.M. Veenhoff, E. van der Giessen, P.R. Onck, Biophys. J. **107**, 1393 (2014)
516. I. Szleifer, M.A. Carignano, Adv. Chem. Phys. **94**, 165 (1996)
517. M. Tagliazucchi, M. Olvera de la Cruz, I. Szleifer, Proc. Natl. Acad. Sci. U. S. A. **107**, 5300 (2010)
518. D. Wang, R.J. Nap, I. Lagzi, B. Kowalczyk, S. Han, B.A. Grzybowski, I. Szleifer, J. Am. Chem. Soc. **133**, 2192 (2011)
519. M. Tagliazucchi, O. Peleg, M. Kroger, Y. Rabin, I. Szleifer, Proc. Natl. Acad. Sci. U.S.A. **110**, 3363 (2013)
520. P.J. Flory, *Statistical Mechanics of Chain Molecule* (Hanser Publishers, New York, 1989)
521. R. Israels, F.A.M. Leermakers, G.J. Fleer, E.B. Zhulina, Macromolecules **27**, 3249 (1994)
522. E.B. Zhulina, T.M. Birshtein, O.V. Borisov, Macromolecules **28**, 1491 (1995)
523. R. Israels, F.A.M. Leermakers, G.J. Fleer, Macromolecules **27**, 3087 (1994)
524. E.B. Zhulina, M. Rubinstein, Soft Matter **8**, 9376 (2012)
525. S.A. Barr, A.Z. Panagiotopoulos, Chem. Phys. **137**, 144704 (2012)
526. R. Nap, P. Gong, I. Szleifer, J. Polym. Sci. B Polym. Phys. **44**, 2638 (2006)
527. M. Tagliazucchi, I. Szleifer, J. Am. Chem. Soc. **137**, 12539 (2015)
528. J. Yin, R. Yang, S. Yan, S. Luan, Sci. Sin. Chim. **50**, 447 (2020)
529. J.F. Lutz, M. Ouchi, D.R. Liu, M. Sawamoto, Science **341**, 1238149 (2013)
530. A.N. Ananth, A. Mishra, S. Frey, A. Dwarkasing, R. Versloot et al., Elife **7**, 31510 (2018)
531. S.S. Patel, B.J. Belmont, J.M. Sante, M.F. Rexach, Cell **129**, 83 (2007)
532. A. Hoelz, E.W. Debler, G. Blobel, Annu. Rev. Biochem. **80**, 613 (2011)
533. S.J. Kim, J. Fernandez-Martinez, I. Nudelman, Y. Shi, W. Zhang, B. Raveh et al., Nature **555**, 475 (2018)
534. R. Peters, BioEssays **3**, 466 (2009)
535. B.B. Hulsmann, A.A. Labokha, D. Gorlich, Cell **150**, 738 (2012)
536. D. Ando, R. Zandi, Y.W. Kim, M. Colvin, M. Rexach, A. Gopinathan, Biophys. J . **106**, 1997 (2014)
537. A. Ghavami, E. van der Giessen, P.R. Onck, Pore complex. PLoS ONE **11**, e0148876 (2016)
538. A. Vovk, C. Gu, M.G. Opferman, L.E. Kapinos, R.Y. Lim et al., Life **5**, e10785 (2016)
539. R. Zahn, D. Osmanović, S. Ehret, C. Araya Callis, S. Frey et al., Elife **5**, 14119 (2016)
540. R. Gamini, W. Han, J.E. Stone, K. Schulten, PLoS Comput. Biol. **10**, e1003488 (2014)
541. S. Milles, D. Mercadante, I.V. Aramburu, M.R. Jensen et al., Cell **163**, 734 (2015)

542. B. Raveh, J.M. Karp, S. Sparks, K. Dutta, M.P. Rout et al., Proc. Natl. Acad. Sci. U. S. A. **113**, E2489 (2016)
543. J. Ma, A. Goryaynov, A. Sarma, W. Yang, Proc. Natl. Acad. Sci. U. S. A. **109**, 7326 (2012)
544. C. Ader, S. Frey, W. Maas, H.B. Schmidt, D. Goerlich, M. Baldus, Proc. Natl. Acad. Sci. USA. **107**, 6281 (2010)
545. S. Rajoo, P. Vallotton, E. Onischenko, K. Weis, Proc. Natl. Acad. Sci. **115**, E3969 (2018)